A Rydberg Interferometer

From coherent formation of ultralong-range Rydberg molecules to state tomography of Rydberg atoms

Björn Butscher

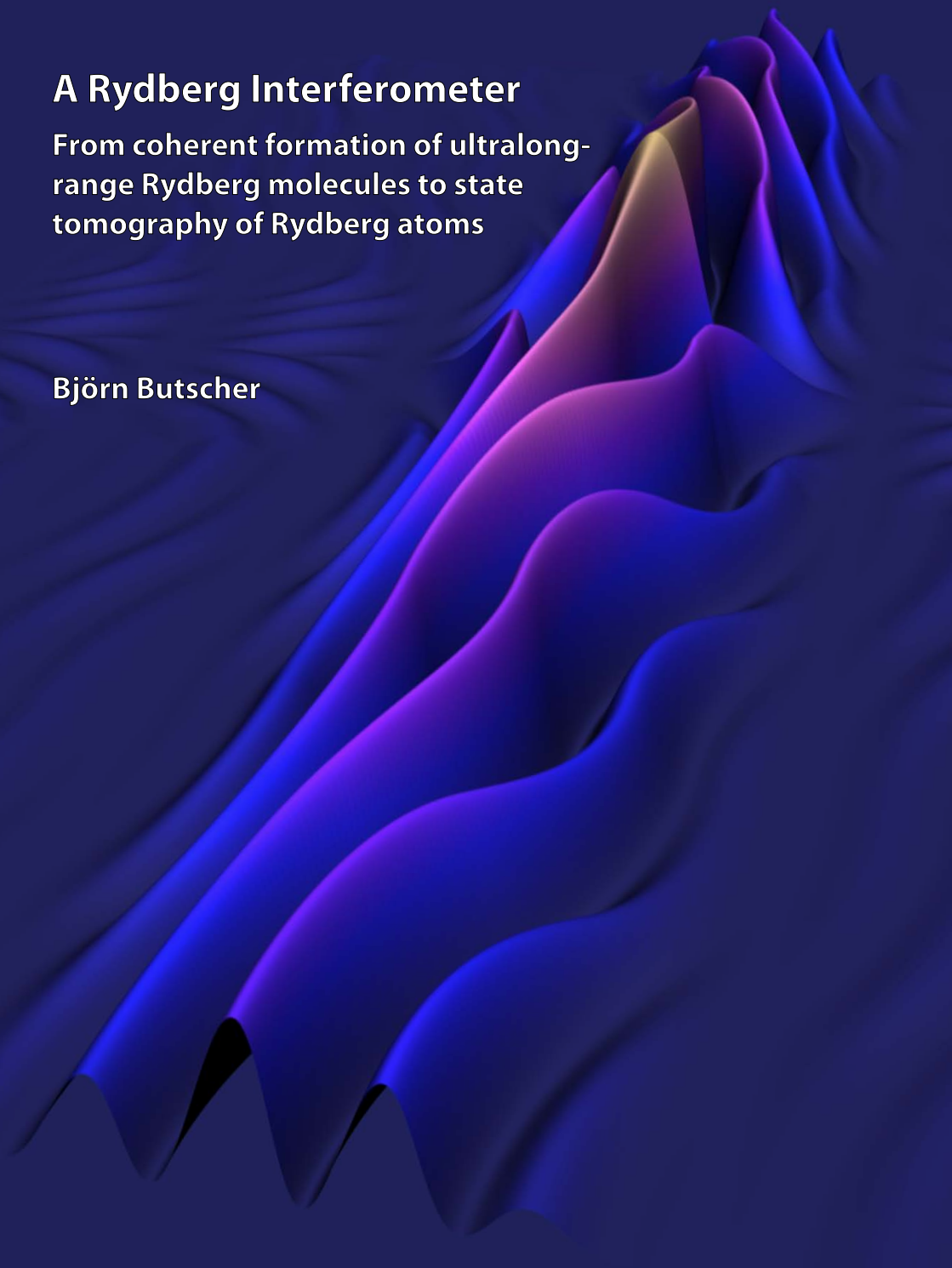

A Rydberg Interferometer:

From coherent formation of ultralong-range Rydberg Molecules to state tomography of Rydberg atoms

Von der Fakultät Mathematik und Physik der
Universität Stuttgart zur Erlangung der Würde eines
Doktors der Naturwissenschaften (Dr. rer. nat.)
genehmigte Abhandlung

vorgelegt von

Björn Butscher
aus Ludwigsburg

Betreuer und Hauptberichter:	Prof. Dr. Tilman Pfau
Mitberichter:	Prof. Dr. Harald Gießen
Prüfungsvorsitzender:	Prof. Dr. Hans Peter Büchler
Tag der mündlichen Prüfung:	26.05.2011

Physikalisches Institut der Universität Stuttgart

2011

Diese Arbeit wurde angefertigt am

5. Physikalischen Institut
Universität Stuttgart
Pfaffenwaldring 57
D-70569 Stuttgart

Achtung! Jetzt gibt es nur zwei Möglichkeiten: Entweder es funktioniert oder es funktioniert nicht.

(Lukas in „Jim Knopf und Lukas, der Lokomotivführer“)

Vorwort

Diese Arbeit untersucht die Erzeugung und die Eigenschaften einer besonderen Art von Atomen: den Rydberg-Atomen. Es handelt sich hierbei nicht um Atome, die einem besonderen chemische Element angehören, sondern die in eine besondere Art von Zuständen angeregt wurden. Diese Rydberg-Zustände sind dadurch gekennzeichnet, daß sich das Valenzelektron in einem Zustand mit großer Hauptquantenzahl n befindet. Die Quantenzahl n bestimmt viele wichtige Eigenschaften der Atome wie die Bindungsenergie, den Atomradius, das elektrische Dipolmoment und die Lebensdauer des Zustands. Bei hohen Quantenzahlen n sind die Bindungsenergien von Rydberg-Atomen sehr klein, die Atomradien sehr groß und die Lebensdauern relativ lang.

Von besonderer Bedeutung ist jedoch die außerordentliche Stärke der van-der-Waals und der Dipol-Dipol Wechselwirkung zwischen Rydberg-Atomen untereinander. Bei Rydberg-Zuständen mit Hauptquantenzahlen $n \approx 100$ kann die Reichweite der Wechselwirkung mehrere 10 µm betragen. Der Abstand zwischen den Grundzustandsatomen in einem ultrakalten Quantengas ist mit etwa 100 nm allerdings wesentlich kleiner als die Reichweite der Wechselwirkung. Hierdurch tritt die Situation ein, daß die Rydberg-Atome durch die Wechselwirkung mit vielen Nachbarn so stark gestört werden, daß sie nicht mehr angeregt werden können. In diesem Fall kann aus mehreren tausend Grundzustandsatomen lediglich ein einziges in den Rydberg-Zustand angeregt werden, da alle weiteren Anregungen durch das Rydberg-Atom blockiert werden. Auf der Ausnutzung dieses Effekts basieren Vorschläge zum Einsatz von Rydberg-Atomen beim Aufbau von Systemen zur Quanteninformationsverarbeitung[1,2], weshalb ein fundamentales Interesse an der Erforschung der Eigenschaften von Rydberg-Atomen besteht.

Neben der Wechselwirkung der Rydberg-Atome untereinander, die zur Rydberg-Blockade führt, ist kürzlich eine andere - eigentlich längst verstandene - Wechselwirkung von Rydberg-Atomen in das Interesse gerückt. Bereits im antiken Griechenland fand nämlich ein elektrisch geladener Stein - der Bernstein - Anwendung als Kleiderbürste, da er die elektrisch neutralen Staubteilchen an sich binden konnte. Verantwortlich hierfür ist die Polarisierbar-

keit von neutralen Teilchen. Durch ein äußeres elektrisches Feld werden in der Materie die beweglichen Elektronen gegen die positiven Atomrümpfe verschoben und es entsteht ein Dipolmoment, durch das die Materie vom elektrischen Feld z. B. einer Punktladung angezogen wird. Auf diesem Effekt basiert auch ein im Jahr 2000 von Chris Greene und seinen Kollegen theoretisch vorhergesagter Bindungsmechanismus[3], mit dem ein Rydberg-Atom ein Atom binden kann, das sich im Grundzustand befindet. Seit die Existenz dieser neuartigen weitausgedehnten Rydberg-Moleküle kürzlich bewiesen wurde[4], erfährt auch dieses Gebiet der Rydberg-Atome einen beträchtlichen Aufschwung.

Bei den meisten Molekülen erfordert es einen hohen experimentellen Aufwand[5], den Grundzustand ihrer Schwingung zu erreichen. Bedingt durch die großen Bindungsabstände der Rydberg-Moleküle können jedoch zwei Atome im Grundzustand direkt zu einem Molekül im Schwingungsgrundzustand $v = 0$ photo-assoziiert werden. Ein Ziel dieser Arbeit bestand darin, die Kontrolle über das Molekül weiter zu verbessern und eine kohärente Erzeugung von weitausgedehnten Rydberg-Molekülen zu erreichen. Hierzu wurde das bestehende Lasersystem zur Anregung der Rydberg-Zustände verbessert, so daß das Gesamtsystem nun eine Linienbreite von unter 60 kHz aufweist.

Mit dem derartig verbesserten Aufbau konnte eine kohärente Anregung des molekularen Grundzustands demonstriert werden. Zum einen wurde dies mit einer aus der Kernspin-Resonanz Technik bekannten Echo-Sequenz gezeigt. Hierbei wird ausgenutzt, daß sich die zeitliche Entwickung eines kohärent kontrollierten Systems unter bestimmten Umständen umkehren lässt. Mit dem Auftreten des Rydberg-Echos im Experiment konnte die kohärente Anregung auf einer Zeitskala von mehreren Mikrosekunden belegt werden.

Durch eine Erweiterung des Aufbaus konnte die Kohärenz der Anregung in einem weiteren Experiment bestätigt werden. Hierzu werden Paare von Grundzustandsatomen mit einem kurzen Laserpuls zunächst in einen Überlagerungszustand aus freiem Paar und gebundenem Molekül gebracht. Nach einer definierten Wartezeit wird diese Superposition mit einem zweiten Laserpuls abgefragt. Für eine völlig kohärente Anregung oszilliert die Anzahl der detektierten Moleküle, wenn die Frequenz des Anregungslasers über die Resonanzfrequenz verstimmt wird. Aus der Sichtbarkeit dieser Oszillation in diesem sogenannten Ramsey Experiment kann auf die Kohärenz der Anregung geschlossen werden.

In Abbildung V.1 ist das Ergebnis dieser Messung gezeigt. Neben den gemessenen Daten ist auch die berechnete Vorhersage eines theoretischen Modells gezeigt. Durch Anpassung der Vorhersage an die experimentellen Daten mit

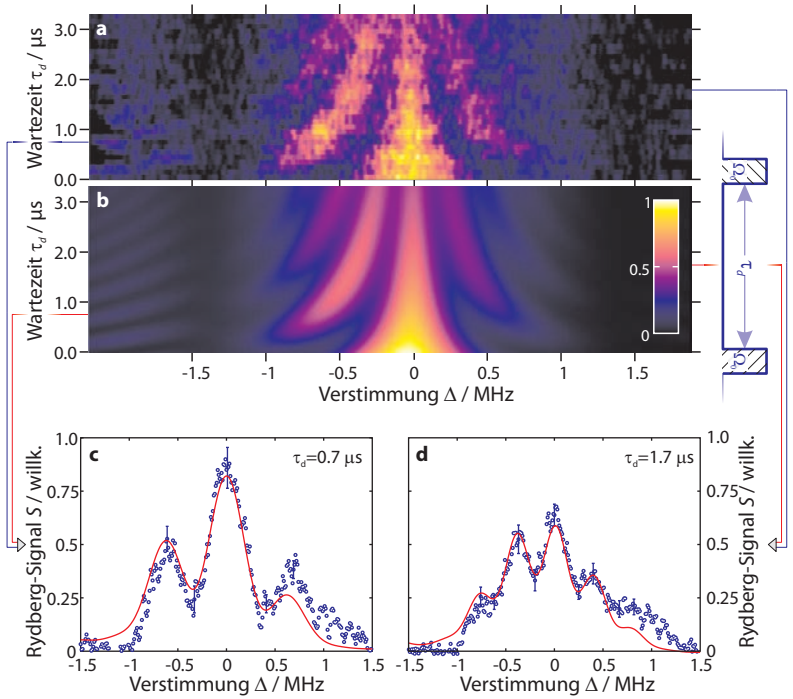

Abbildung V.1 | Ramsey Experimente an Rydberg-Molekülen.
a Experimentelles Rydberg-Signal für verschiedene Wartezeiten. **b** Berechnetes Rydberg-Signal mit optimierten Modell-Parametern. **c, d** Schnitte für feste Wartezeit. Die Oszillation des Rydberg-Signals ist deutlich zu erkennen und beweist die kohärente Anregung.

Hilfe der Parameter des Modells konnte die Kohärenzzeit mit 1.3 µs und die Lebensdauer der Moleküle mit 7.1 µs bestimmt werden.

Da die beobachtete Lebensdauer der Rydberg-Moleküle erheblich kürzer ist als die Lebensdauer des einzelnen Rydberg-Atoms von ca. 65 µs wurde der Grund für diese verkürtze Lebensdauer untersucht. Die wahrscheinlichste Ursache für die Verkürzung der Lebensdauer sind Stöße der Moleküle mit Atomen im Grundzustand. Die Rate der Stöße zwischen einem Rydberg-Molekül und Grundzustandsatomen wird durch die Dichte der Atome bestimmt. Deshalb wurde die Lebensdauer für verschiedene Dichten gemessen. Die Abhängigkeit der Lebensdauer von der Dichte wurde mit einem einfachen Modell verglichen, das die Dissoziation des Moleküls bei einem Stoß an-

nimmt. Ein solches Modell ist plausibel, da der Rydberg-Zustand empfindlich auf äußere Störungen reagiert. Aus der guten Übereinstimmung von Theorie und Experiment lässt sich die Verkürzung der Lebensdauer der Rydberg-Moleküle auf das Stoßen mit den Atomen zurückführen.

Darüberhinaus wurde bei der Untersuchung eines angeregten Schwingungszustands der Moleküle eine weitere systematische Verkürzung der Lebensdauer gegenüber dem Schwingungsgrundzustand festgestellt. Aus dieser Beobachtung konnte gezeigt werden, daß dieser Molekülzustand durch einen völlig anderen Bindungsmechanismus stabilisiert wird, der auf der Quantenrefelexion des Schwingungszustands im Molekülpotential basiert [6,7].

Basierend auf der erfolgreichen Verbesserung des Lasersystems und der erzielten Kohärenzzeiten wurde das Ramsey Experiment auch für die Anregung von Rydberg-Atomen eingesetzt. Die Besonderheit bestand hierbei darin, daß das Rydberg-Atom in der Wartezeit zwischen dem Laserpuls zur Erzeugung des Überlagerungszustands und dem Abfragepuls manipuliert wurde. Dieser besondere experimentelle Aufbau stellt ein Interferometer dar, das eine besonders präzise Untersuchung der Antwort von Rydberg-Atomen auf äußere Manipulationen ermöglicht. Zur erstmaligen Demonstration eines solchen Interferometers für Rydberg-Atome wurde mit einem elektischen Feld ein bekanntes Muster erzeugt und die Funktion des Interferometers bestätigt.

Mit dem nun verfügbaren Interferometer wurde dann die Energiestruktur von Rydberg-Atomen in gekreuzten elektrischen und magnetischen Feldern untersucht. Durch die Aufhebung sämtlicher Entartungen und die Kopplung der magnetischen Unterzustände ergeben sich komplexe Phänomene in der zeitlichen Entwicklung der Zustände. Basierend auf begleitenden Rechnungen konnte die Dynamik der Atome wie in Abbildung V.2 gezeigt aus den Messungen rekonstruiert werden. Das Interferometer wurde somit als Zustandstomograph für Rydberg-Atome eingesetzt.

Das Interferometer für Rydberg-Zustände, das im Rahmen dieser Arbeit entwickelt wurde, besitzt vielfältige Einsatzmöglichkeiten. Zum einen können damit dynamische Phänomene der Rydberg-Moleküle untersucht werden. Insbesondere ist hier die Frage nach der Beobachtbarkeit der Quantenreflexion von Interesse. Daneben eignet sich das Interferometer auch zur Untersuchung der Wechselwirkung von Rydberg-Atomen. Die Untersuchung der Stärke und der Durchstimmbarkeit von Förster Resonanzen stellt hierbei den nächsten Schritt dar.

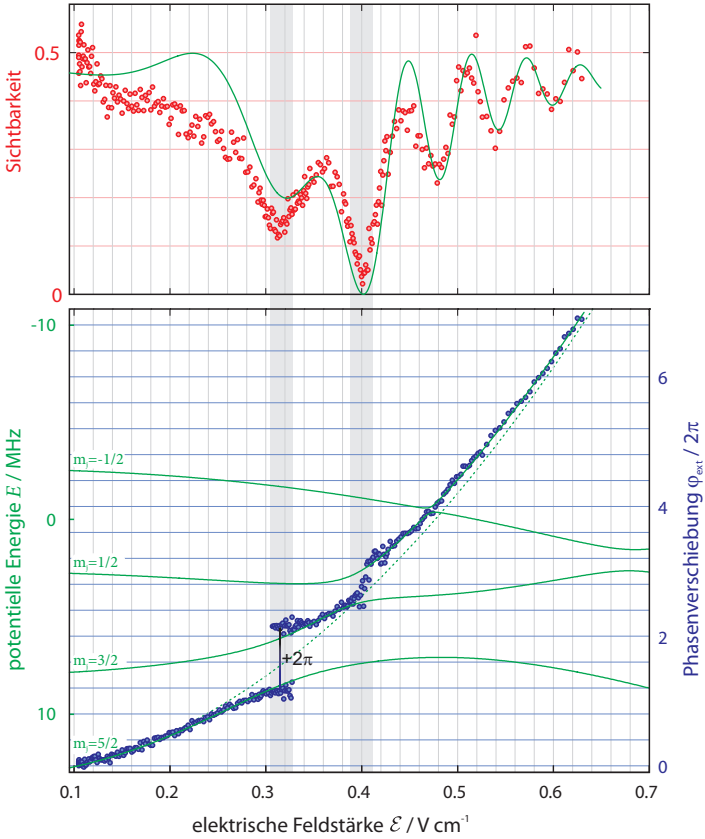

Abbildung V.2 | Ramsey Experimente an Rydberg-Atomen.
Aus den Messungen extrahierte Sichtbarkeit $\mathcal{V}$ (rote Punkte) und Phasenverschiebung φ_{ext} (blaue Punkte). Die grünen Linien sind das Ergebnis der Rechnungen. Für die Sichtbarkeit besteht eine gute qualitative Übereinstimmung. Aus dem Vergleich des gemessenen und des berechneten Verlaufs der Phasenverschiebung ergibt sich ein 2π-Phasensprung bei $\mathcal{E} \approx 0.33\,\text{V}\,\text{cm}^{-1}$, der durch die weiteren Messungen bestätigt wird.

Im Rahmen der vorliegenden Dissertation wurden die folgenden Publikationen veröffentlicht:

- A. K. Mohapatra, M. G. Bason, B. Butscher, K. J. Weatherill, and C. S. Adams. A giant electro-optic effect using polarizable dark states. *Nature Physics*, 4:890–894, November 2008.

- V. Bendkowsky, B. Butscher, J. Nipper, J. P. Shaffer, R. Löw, and T. Pfau. Observation of ultralong-range Rydberg molecules. *Nature*, 458:1005–1008, April 2009.

- U. Raitzsch, R. Heidemann, H. Weimer, B. Butscher, P. Kollmann, R. Löw, H. P. Büchler, and T. Pfau. Investigation of dephasing rates in an interacting Rydberg gas. *New Journal of Physics*, 11(5):055014, May 2009.

- B. Butscher, V. Bendkowsky, and T. Pfau. Moleküle aus Rydberg-Atomen. *Physik in unserer Zeit*, 40:173–174, July 2009.

- R. Löw, H. Weimer, U. Krohn, R. Heidemann, V. Bendkowsky, B. Butscher, H. P. Büchler, and T. Pfau. Universal scaling in a strongly interacting Rydberg gas. *Physical Review A*, 80(3):033422, September 2009.

- V. Bendkowsky, B. Butscher, J. Nipper, J. B. Balewski, J. P. Shaffer, R. Löw, T. Pfau, W. Li, J. Stanojevic, T. Pohl, and J. M. Rost. Rydberg Trimers and Excited Dimers Bound by Internal Quantum Reflection. *Physical Review Letters*, 105(16):163201, October 2010.

- B. Butscher, J. Nipper, J. B. Balewski, L. Kukota, V. Bendkowsky, R. Löw, and T. Pfau. Atom-molecule coherence for ultralong-range Rydberg dimers. *Nature Physics*, 6:970–974, December 2010.

- B. Butscher, V. Bendkowsky, J. Nipper, J. B. Balewski, L. Kukota, R. Löw, T. Pfau, W. Li, T. Pohl, and J. M. Rost. Lifetimes of ultralong-range Rydberg molecules in vibrational ground and excited state. *ArXiv e-prints, accepted for publication in J. Phys. B*, February 2011.

Contents

Introduction

The astronomic observation of the planetary movement in our solar system by Tycho Brahe was one of the first systematic investigations of physical laws using the visible spectrum of light. Based on these findings Nicolaus Copernicus developed the revolutionary theory of Heliocentrism. Even today, light observed from planetary systems billions of light years away helps to gain insight into their constellations[8].

Later, the spectroscopic investigation of light transmitted through atomic vapors were among the first experiments that aimed to gain insight into the structure of matter. The observation of characteristic lines in the solar spectrum by Joseph von Fraunhofer[9] was one of the pioneering experiments, leading to the postulation of Nils Bohr's model of the atom[10]. Steady improvement of the spectroscopic techniques helped to refine theory and concepts of the atomic system, and today fundamental properties of atoms like the hyperfine splitting of hydrogen are measured with a precision of 3.5×10^{-8} using optical transitions[11].

Although spectroscopy proved to be a worthwhile tool to explore the properties of atoms, since the 1930ies a different approach made its way for the manipulation of the internal states of atoms: radio frequency radiation. One of the reasons for the superiority of radio frequency compared to light was the high precision and the availability of coherent sources. Consequently, the controlled manipulation of the internal state of atoms was first demonstrated by Isidor Isaac Rabi in 1938 using radio frequency[12]. In 1949, Norman Ramsey reached a milestone when he separated the radiation into two pulses: the first pulse to prepare the atom in a coherent superposition state and the second pulse to probe it - the Ramsey interferometer was born[13]. Based on this simple principle, the interferometric investigation with radio frequency and later with microwave radiation found its way to become a standard application in scientific research and technical application like nuclear magnetic resonance spectroscopy as well as highly accurate clocks that are commonly used e.g. for satellite navigation and reach accuracies of 1×10^{-14} [14].

Inspired from the coherent sources of microwave radiation, Arthur Schawlow, Charles Townes, Theodore Maiman and many others fathered the idea of a

source for coherent light - the laser[15]. While the first laser sources were not easy to maintain and limited in power and accessible spectral range, the field progressed fast and today laser light is available for the complete range of the visible spectrum.

Nowadays, the sophistication in means of stability and accuracy of the generated laser light is able to challenge the well established high precision setup based on radio frequency and microwave radiation. Consequently, the next generation of ultra-stable atomic clocks keeps abreast to this development and will be based on optical transitions[16].

Another field of research that is of interest since the early days of atomic physics are highly excited atoms, the so-called Rydberg atoms. While the spectra of the Rydberg states of hydrogen helped to develop the idea of quantized energy levels of atoms, Rydberg atoms have been appreciated in the 1970ies to study coherence processes in thermal atomic samples[17]. Since the transition energies between the Rydberg levels are on the microwave scale, Rydberg atoms were ideal systems to be investigated using highly accurate microwave sources.

In the last years, another property of Rydberg atoms has attracted interest: their exaggerated interaction. Rydberg atoms are very large compared to ground-state atoms. This huge distance from the core makes the Rydberg electron very sensitive to external distortions like electric fields and thus Rydberg atoms have huge polarizabilities.

While the van der Waals C_6 coefficient is on the order of 5000 a.u. for the ground state of rubidium[18,19,20], the dispersion coefficient for the 35s-state is $C_6 = 1.7 \times 10^{19}$ a.u.[21]. In 2000, Dieter Jaksch et al. proposed a Rydberg quantum gate based on this enormous interaction strength[22,23]. In this approach, quantum information is stored in the long-lived magnetic structure of the ground state of an ultracold gas and the excitation to the Rydberg states provides the interaction between the quantum bits. Based on this proposal, in the last years more sophisticated schemes adopted to realistic experimental parameters have been developed[1,2]. However, all these schemes rely on the coherent coupling between the ground state and the Rydberg state via its optical transition.

Moreover, the physics of Rydberg atoms comes up with another specialty based on the interaction of the Rydberg electron with a ground-state atom. In 2000, Chris Greene et al. proposed that the attractive scattering of Rydberg electron and a ground-state atom gives rise to a novel molecular binding with bond length on the order of several thousand Bohr radii[3]. Only recently,

these exotic molecules were photoassociated from a dense sample of ultracold rubidium atoms[4]. Inspired by this discovery, more sophisticated theoretical models are developed and even another new binding mechanism based on quantum reflection has been unveiled[6]. However, there are still open questions in the field of ultralong-range Rydberg molecules, like the reason for the short lifetime of the molecules and the quest for their coherent creation.

It hence can be seen that the field of Rydberg atoms is a multifaceted and very fast progressing research area. The experimental methods have been refined over the last years and the results allowed to gain a deeper understanding of the physics of Rydberg atoms. With the routinely preparation of ultracold samples of rubidium atoms or even Bose-Einstein condensates (BEC)[24,25] combined with a laser setup for the Rydberg atoms, the experimental setup employed in this thesis has been used to demonstrate the Rydberg excitation of BECs[26] and to investigate the dephasing of dense samples of Rydberg atoms[27] as well as for the first observation ultralong-range Rydberg molecules[28]. At the current point of this evolution, a next major step needs to be tackled: the coherent coupling between the ground state and the Rydberg state.

This thesis will combine the recent advances in the development of ultrastable laser setups with the mature concepts of creating and probing coherence with microwave radiation in a Ramsey type experiment with optical coupling fields. Therefore, the existing Rydberg lasers have been replaced by a narrow-band setup and the control of the experimental sequence is upgraded to allow for a time resolution on the order of nano seconds. The merit of these improvements is a setup that can bring the trapped atoms into a superposition between ground state and Rydberg state. When the ultralong-range Rydberg molecules are addressed, the coherent photo-association and -dissociation of the molecules is observed. And for unbound atoms, this Rydberg interferometer will be used to explore the dynamic evolution of the Rydberg state under a tunable perturbation.

Part I

Theoretical Foundations

1 Rydberg atoms

This thesis investigates a very special kind of atoms - Rydberg atoms. A Rydberg atom is an atom whose outer electron is in a highly excited state where it is bound considerably weaker to the atomic core compared to the ground state. Rydberg atoms thus are not a chemically distinct species of atoms and they can be formed from almost any chemical atomic species by exciting any valence electron into a high orbit. Since the most important properties of these highly excited states are akin to all species and only weakly dominated by their particular chemical properties, they form an own special class of atoms.

In this chapter, an introduction to Rydberg atoms and some of their fundamental properties are given. As the experimental realization is based on rubidium, most properties are given for Rydberg states of rubidium.

Detailed numerical calculation for Rydberg states of rubidium are discussed in chapter 2.

1.1 Hydrogen and Hydrogen-like Atoms

It was already in the late 19th century when Fraunhofer, Ångstrøm, Vogel and Huggins systematically investigated the spectrum of the lightest and simplest atom - the hydrogen atom[9,29,30]. These experiments were the first investigations on Rydberg atoms. The first empirically found formula for the line series was given 1885 by Balmer[31]. A more precise mathematical formulation

$$\bar{\nu}_{nl} = \bar{\nu}_{\infty,l} - \frac{R_\infty}{n^2}, \tag{1.1}$$

- which is still valid today - was found by Johannes Rydberg[32]. In this formulation, $\bar{\nu}_{nl}$ is the wavenumber of the observed transition, n is the principal quantum number of the excited Rydberg state, $\bar{\nu}_{\infty,l}$ is the series limit and $R_\infty = 109\,737.315\,685\,27(73)\ \mathrm{cm}^{-1}$ is the Rydberg constant for hydrogen.

property		scaling	^{87}Rb ($35s$)
binding energy	$E_{\tilde{n}}$	$\tilde{n}^{-2}$	$-108.05\,/\mathrm{cm}$
level separation	$E_{\tilde{n}} - E_{\tilde{n}-1}$	$\tilde{n}^{-3}$	$7.11\,/\mathrm{cm}$
orbital radius	$r_{\tilde{n}} = \frac{4\pi\varepsilon_0\hbar^2\tilde{n}^2}{Ze^2m_e}$	$\tilde{n}^2$	$998\,a_0$
trans. dipole moment	$\mu = \langle nl\vert\, er\,\vert n'l'\rangle$	$\tilde{n}^2$	up to $676\,ea_0$
polarizability	$\alpha \propto \frac{\mu^2}{E_n - E_m}$	$\tilde{n}^7$	$4.2\,\mathrm{MHz/(V/cm)^2}$
van der Waals coeff.	$C_6 \propto \frac{(\mu_1\mu_2)^2}{E_n - E_m}$	$\tilde{n}^{11}$	$1.26 \times 10^{-61}\,\mathrm{J\,m^6}$

Table 1.1 | Scaling of fundamental properties of Rydberg states with the principal quantum number $\tilde{n} = n - \delta_{nlj}$ and calculated values for the $35s$-state of ^{87}Rb

However, it was not until the development of the Bohr model of the atom[10] that the fundamental meaning of the principal quantum number n was revealed. The Bohr model allowed to link the principal quantum number n to tangible quantities like the spatial extend of the atom. The radius of an imagined circular orbit around the core of the electron in a state with principal quantum number n depends quadratically on n and is given by

$$r_\mathrm{e} = \frac{4\pi\varepsilon_0\hbar^2}{e^2 m_\mathrm{e}} n^2 = a_0 n^2, \tag{1.2}$$

where $a_0 = 5.29 \times 10^{-11}\,\mathrm{m}$ is the Bohr radius and m_e is the electron mass. For the electron's energy levels E the model obtains

$$E = -\frac{e^4 m_\mathrm{e}}{8\varepsilon^2 h^2}\frac{1}{n^2} = -hc\frac{R_\mathrm{Ryd}}{n^2}. \tag{1.3}$$

With the help of (1.3) one can assign the the observed spectral lines of the Balmer series (1.1) to the transition of the electron of a hydrogen atom between the first excited state ($n = 2$) and Rydberg states with principal quantum number n.

In this thesis, the Rydberg states of rubidium are investigated. Rubidium has 35 electrons, but it has only one valence electron and all other electrons are in closed electron shells, like for all alkali atoms. As the core charge is mostly screened by the closed shell, the valence electron samples the coulomb potential of the effectively singly charged Rb^+ ion as long as it is does not enter the inner shells. This places rubidium among the hydrogen-like atoms and allows

state	$n^2s_{1/2}$	$n^2p_{1/2}$	$n^2p_{3/2}$	$n^2d_{3/2}$	$n^2d_{5/2}$	n^2f_j
δ_0	3.1311804	2.6548849	2.6416737	1.3480917	1.3464657	0.016312
δ_2	0.1784	0.2900	0.2950	−0.6029	−0.5960	−0.064007
δ_4	−1.8	−7.904	−0.97495	−1.50517	−1.50517	−0.36005
δ_6	-	116.4373	14.6001	−2.4206	−2.4206	3.239
δ_8	-	−405.907	−44.7265	19.736	19.736	-
ref.	[33]	[33,34]	[33,34]	[33,34]	[33,34]	[34]

Table 1.2 | Quantum defect parameters for ^{85}Rb.

to derive many of the properties of the Rydberg states of rubidium analogous to hydrogen.

Since the Rydberg electron can polarize the closed electron shells or can enter into the ionic core, it is an oversimplification to treat the ionic core as singly charged. The most convenient way to account for the energy shifts due to the interaction between Rydberg electron and closed shells is to employ quantum defect theory[35]. There, the principal quantum number n for hydrogen-like atoms is replaced by an effective quantum number $\tilde{n} = (n - \delta_{nlj})$ which accounts for the distortion of the Rydberg electron's wave function through the quantum defect δ_{nlj}. The quantum defect δ_{nlj} then represents the shift of the energy levels between hydrogen atoms and hydrogen-like atoms.

Consequently, the binding energies for rubidium can be calculated via

$$E_{nlj} = -hc\frac{R_{\mathrm{Rb}}}{\tilde{n}^2}, \tag{1.4}$$

where $R_{\mathrm{Rb}} = \frac{R_\infty}{1+m_e/M} = 109\,736.605\,\mathrm{cm}^{-1}$ is the Rydberg constant for rubidium[36] with the the mass M of rubidium. As for the binding energy, the scaling of the characteristic properties with the principal quantum number n for rubidium Rydberg atoms is the same as for hydrogen. Scaling properties and calculated values for the 35s-state of ^{87}Rb for selected properties are given in Table 1.1.

The quantum defect is a theoretical model that can be derived from sophisticated calculations. Conveniently, however, it is extracted form spectroscopic data, most suitably covering a large range of principal quantum numbers. Moreover, the quantum defect not only depends on n, but also on the angular momentum l, since states with lower angular momentum have due to their elliptic orbits more probability density close to the ionic core and thus

these states are less hydrogen-like than those of high angular momentum. The quantum defect also accounts for the fine structure splitting, making it depend on j as well. The most convenient expansion for the quantum defect δ_{nlj} is the Rydberg Ritz-formula

$$\delta_{nlj} = \delta_0 + \frac{\delta_2}{(n-\delta_0)^2} + \frac{\delta_4}{(n-\delta_0)^4} + \frac{\delta_6}{(n-\delta_0)^6} + \frac{\delta_8}{(n-\delta_0)^8} + \dots \quad (1.5)$$

The coefficients δ_0,δ_2,δ_4,δ_6 and δ_8 for rubidium obtained from spectroscopic data of a large range of Rydberg states are listed in Table 1.2. It can be seen that the coefficients differ significantly from zero only for for s, p, d and f states, the so-called low-l states. States with ($l > f$) have no quantum defect and thus are degenerate. The Rydberg states of rubidium thus can be divided into the class of non-degenerate low-l states and the hydrogen-like high-l states.

1.2 Stark effect

The so-called Stark effect is the shift of atomic energy levels due to the interaction with an external electric field. The magnitude of the shift depends on the strength of the electric field. Due to its large orbital radius, the interaction of the Rydberg electron of a Rydberg atom and an external electric field is exaggerated. The potential for a Rydberg atom in an electric field $\boldsymbol{\mathcal{E}}$ is given by

$$V = -\mathfrak{d}\boldsymbol{\mathcal{E}}, \quad (1.6)$$

where $\mathfrak{d}$ is the electric dipole moment of the Rydberg atom. In this section, the fundamental properties of Rydberg atoms in homogeneous electric fields will be discussed and for this purpose it is sufficient to restrict to the case of an electric field pointing along the quantization axis, i.e. $\boldsymbol{\mathcal{E}} = \mathcal{E}\mathbf{e_z}$. A thorough treatment of Rydberg atoms in external fields is subject to chapter 2.

When the shift due to (1.6) is small compared to the spacing of the unperturbed levels, the dipole moment $\mathfrak{d}$ can be expanded in powers of $\mathcal{E}$:

$$\mathfrak{d} = \mathfrak{d}_0 + \frac{1}{2}\alpha\mathcal{E} + \mathcal{O}(\mathcal{E}^2). \quad (1.7)$$

Here, $\mathfrak{d}_0 = \langle nl|\, e\mathbf{z}\,|nl\rangle$ is the expectation value of the dipole operator $e\mathbf{z}$ of the unperturbed Rydberg state $|nl\rangle$ and the scalar polarizability α is given by

$$\alpha = 2 \sum_{\substack{l'n' \\ n \neq n'}} \frac{|\langle nl| e\mathbf{z} |n'l'\rangle|^2}{E_{nl} - E_{n'l'}}. \tag{1.8}$$

Since the dipole operator $e\mathbf{z}$ is antisymmetric under inversion, only the expectation values of states with different parity are non-zero and thus the low-l states have no dipole moment $\mathfrak{d}$ in the absence of an external field, and thus only exhibit quadratic or higher order Stark shift (see Figure 1.1 **b,c**).

The high-l states, however, are degenerate and one can define basis states with contributions from states with different parity. The diagonal matrix elements of such states are non-zero and thus the high-l states can have a linear Stark shift (Figure 1.1 **a**), just like hydrogen atoms.

For heavy atoms like rubidium, the spin-orbit coupling cannot be neglected and the fine-structure must be included when calculating the Stark shift. The hyperfine-splitting in the range $28 \leq n \leq 33$ for ^{85}Rb and ^{87}Rb has been measured by Li et al[33]. They give the empirical scaling formula the hyperfine splitting

$$\nu_{\mathrm{HFS}} = \nu^{\circ}_{\mathrm{HFS}} \tilde{n}^{-3}, \tag{1.9}$$

where $\nu^{\circ}_{\mathrm{HFS}} = 14.6(14)$ GHz for ^{85}Rb. From their data for ^{87}Rb, one calculates $\nu^{\circ}_{\mathrm{HFS}} = 33.5(9)$ GHz. This is on the order of 1 MHz for states around $n = 35$. For states with higher angular momentum, the hyperfine splitting can be neglected since these states have vanishing probability density at the origin, and thus only weak interaction with the core spin. An exemplary Stark map can be found in Figure 1.1. Details on the calculation of this Stark map will be given in chapter 2.

1.3 Field ionization

As it has become clear in the previous section, the energy levels of Rydberg atom can be considerably shifted by weak electric fields. As soon as the field is strong enough to shift the levels on the order of the level spacing, it cannot be treated in perturbation theory any longer. If, however, the field is increased further, it can disturb the Rydberg electron's wave function so much that the energy shift exhibits the binding energy of the Rydberg electron which in rubidium is only on the order of 100 cm^{-1}.

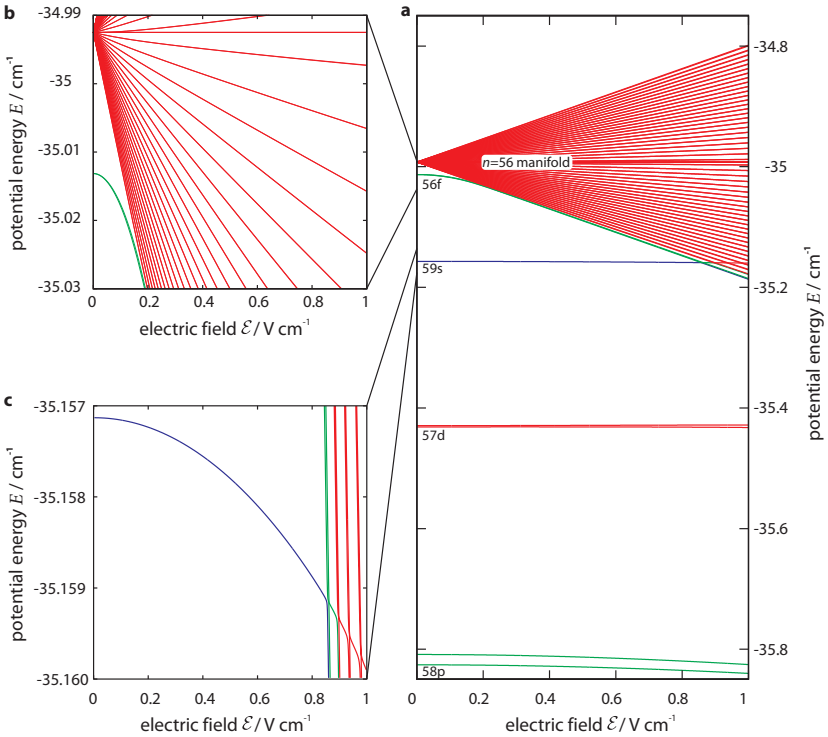

Figure 1.1 | Stark map. Energy E of the $|m_j = 1/2|$ rubidium Rydberg states in the region of the $n = 56$ manifold as function of the electric field $\mathcal{E}$. **a,** One can distinguish the degenerate high-l manifold (red) with its linear Stark shift from low-l states with a quadratic Stark shift. **b,** Due to its small quantum defect, the $56f$-state is nearly degenerate with the $n = 56$-manifold. **c,** The s-states exhibit a nearly perfect quadratic Stark effect.

Since the energy to strip the Rydberg electron off the atomic core can be provided by moderate electric fields, field ionization is a widely used technique to detect Rydberg atoms. Applying a constant electric field $\mathcal{E}$ along the z-direction to a Rydberg atom tilts the Coulomb potential and leads to an anisotropic potential, which is depicted in Figure 1.2. The resulting potential reads

$$V_{\mathcal{E}}(x,y,z) = -\frac{e^2}{4\pi\varepsilon_0}\frac{1}{\sqrt{x^2+y^2+z^2}} - e\mathcal{E}z \tag{1.10}$$

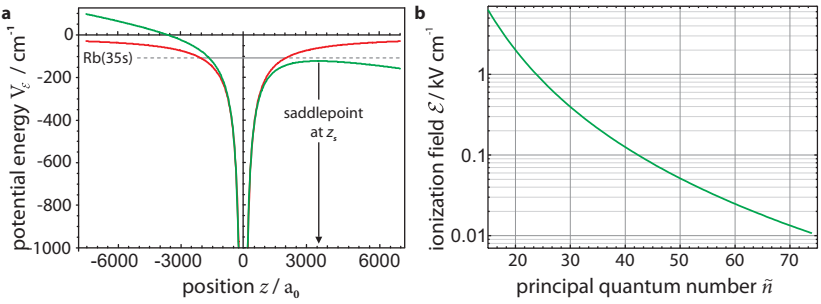

Figure 1.2 | Field ionization. **a,** Atomic Coulomb potential (red) and atomic potential in the presence of an electric field $\mathcal{E} = 400\,\mathrm{V/cm}$ (green). The atomic potential is lowered for $z > 0$ and the electron in the $35s$-state is no more bound. **b,** Scaling of the classical limit for field ionization with $\tilde{n}$.

with a local maximum at the saddlepoint

$$x_s = 0,\ y_s = 0,\ z_s = \sqrt{\frac{e}{4\pi\varepsilon_0 |\mathcal{E}|}}\,. \tag{1.11}$$

Classically, electrons with binding energies E_{nl} higher that the height of the barrier (1.10) are no longer bound. The barrier height equals the binding energy when

$$V_{\mathcal{E}}(0,0,z_s) = -\sqrt{\frac{e^3 |\mathcal{E}|}{\pi\varepsilon_0}} \stackrel{!}{=} -\frac{R_{\mathrm{Rb}}}{\tilde{n}^2} \tag{1.12}$$

and the critical value of the electric field to ionize a Rydberg atom then reads

$$|E| = \frac{\pi\varepsilon_0 R_{\mathrm{Rb}}^2}{e^3\,\tilde{n}^4} = 3.2\times 10^8\,\mathrm{V\,cm^{-1}}\cdot\tilde{n}^{-4}\,. \tag{1.13}$$

This calculation neglects the tunneling of the Rydberg electron through the potential as well as the Stark shift of the Rydberg levels. Nevertheless it serves as a good approximation for the ionization fields and is verified by experimental observations. Note however, that these calculations assume that the ionizing field is turned on slowly that the Rydberg state evolves adiabatically. If the field is ramped up fast, the state can not follow adiabatically and takes a diabatic path though the avoided level crossings with the manifold, resulting in a changed ionization field[36,37].

1.4 Lifetime of Rydberg atoms

In a two-level system, the radiative lifetime τ_{rad} of the excited state $|n'l'\rangle$ is determined by the Einstein A-coefficient

$$\frac{1}{\tau_{\mathrm{rad}}(n,l)} = A^{nl}_{n'l'} = \frac{(\omega^{nl}_{n'l'})^3}{3\pi\varepsilon_0\hbar c^3} |\langle n'l'| e\mathbf{r} |nl\rangle|^2 \tag{1.14}$$

where $\omega^{nl}_{n'l'} = (E_{n'l'} - E_{nl})/\hbar$ is the transition frequency and $\langle n'l'| e\mathbf{r} |nl\rangle = \mathfrak{d}^{nl}_{n'l'}$ is the dipole matrix element of the transition.

Treating Rydberg atoms as two-level systems, however, is an oversimplification since atoms in the level $|nl\rangle$ can not only decay to one level $|n'l'\rangle$ but to a variety of lower lying levels. To account for all of these decay channels, the decay rates for each possible channel $|nl\rangle \rightarrow |n'l'\rangle$ - the Einstein A-coefficients - have to be summed up. The radiative lifetime then read

$$\tau_{\mathrm{rad}}(n,l) = \left[\sum_{E_{n'l'} < E_{nl}} A^{nl}_{n'l'} \right]^{-1}, \tag{1.15}$$

where the summation is only over final states $|n'l'\rangle$ with lower energy than the initial state $|nl\rangle$. From (1.14) it can be seen that the Einstein coefficient $A^{nl}_{n'l'}$ accounts for both, the transition dipole matrix element $\mathfrak{d}^{nl}_{n'l'}$ and the transition frequency $\omega^{nl}_{n'l'}$. Since the level spacing in the region around $n = 40$ is on the order of 100 GHz and the transition energy to the $5p$-states is on the order of 600 THz, the energy term dominates the Einstein coefficient over the dipole matrix element. Rydberg atoms in ns or nd levels thus will most dominantly decay into the $5p_{1/2}$ and $5p_{3/2}$ levels.

The transition frequencies $\omega^{nl}_{n'l'}$ can be determined from quantum defect theory and the transition dipole matrix elements $\mathfrak{d}^{nl}_{n'l'}$ from a numerical calculation of the wave functions of Rydberg states, and thus the radiative lifetime of Rydberg atom can be calculated. An overview of the calculated radiative lifetimes for rubidium is given in Figure 1.3. Since the theoretical prediction depend on the parameters used in the theoretical models employed in the calculations, experimental measurements of the radiative lifetimes serve as valuable benchmarks. Radiative lifetimes of rubidium have already been measured in the 1970ies for ns and nd[42], np[43] and nf states[44]. Recently, the effects of collisions and superradiance in hot gases has been overcome by using cold samples. In these experiments, the radiative lifetimes of Rb(np)

state	Gounand[38]		Beterov[39]		Oliveira[40]		Branden[41]	
	τ'	γ	τ'	γ	τ'	γ	τ'	γ
$s_{1/2}$	1.43	2.94	1.368	3.0008	1.45(3)	3.02(2)	1.4(1)	2.99(3)
$p_{1/2}$	2.76	3.02	2.4360	2.9989	2.80(3)	3.01(3)	3.5(4)	2.90(3)
$p_{3/2}$			2.22135	3.00256				
$d_{3/2}$	2.09	2.85	1.0761	2.9898	2.10(2)	2.89(2)	1.8(3)	2.84(4)
$d_{5/2}$			1.0687	2.9897				

Table 1.3 | Lifetime parameters Theoretical and experimental parameter τ (in ns) and γ for the n dependence of the radiative lifetime of ^{85}Rb as defined in (1.16).

states and their dependency on the principal quantum number n in cold samples in the range of $31 \leq n \leq 45$[40], those of Rb(ns) and Rb(nd) states even for $26 \leq n \leq 45$[45,46] could be determined with enhanced accuracy. The most recent measurement of the radiative lifetime has been reported by Branden et al.[41] and is shown in Figure 1.3 together with the lifetimes calculated by Beterov et al. To compare the different results of theories and experiments, it is usual to describe the radiative lifetime using the analytic expression

$$\tau_{rad}(nl) = \tau'(n - \delta_{nlj})^{\gamma}\,, \tag{1.16}$$

where the parameter $\tau'$and γ are fitted to experimentally obtained lifetimes. Table 1.3 summarizes these parameters for the experiments done by Oliveira et al.[40] and Branden et al.[41] along with with theoretical predictions given by Gounand[38] and Beterov et al.[39].

From Figure 1.3 it can be seen that the experimentally obtained lifetimes are not explained by the calculated radiative lifetimes. The reason is that apart from the radiative lifetime, there is a second decay process that can considerably shorten the lifetime of Rydberg atom in experimental investigations. Although the decay via low-energy transitions to neighboring states is suppressed in spontaneous emission, these transitions can be induced by blackbody radiation as soon as the temperature of the environment T becomes comparable to or larger than the spacing of the Rydberg level $k_B T \approx E_{nl} - E_{n'l'}$[36].

In this regime, the modes of blackbody radiation that are resonant with atomic transitions have high photon occupation numbers $N \gg 1$ and the stimulated transfer of population of the initial Rydberg state $|nl\rangle$ to neighboring states

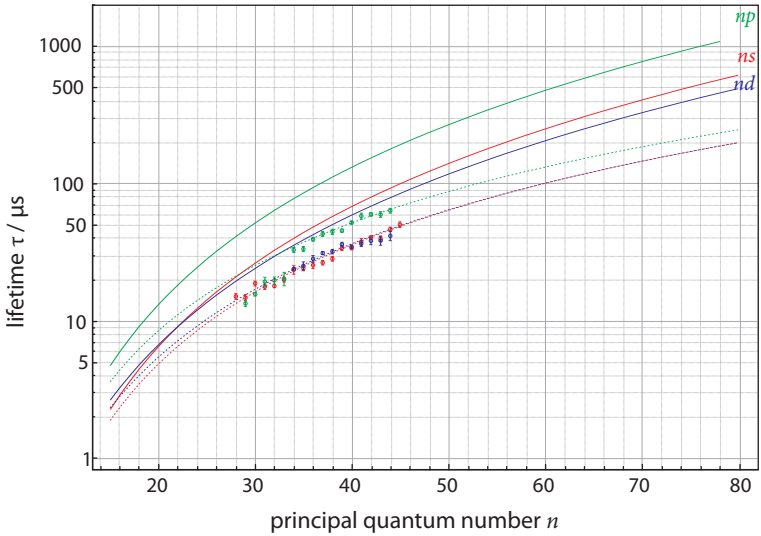

Figure 1.3 | Lifetimes of Rydberg states. The straight curves show the radiative lifetimes τ_{rad} for $l = s_{1/2}, p_{3/2}, d_{5/2}$ Rydberg states and the dashed curves the calculated effective lifetimes τ_{eff} including blackbody induced decay at temperature $T = 300\ K$ as calculated by Beterov et al.[39] The circled data points are the measured lifetimes from Branden et al.[41]

$|n'l'\rangle$ by emission or absorption of photons from the thermal radiation field thus can no longer be neglected. The probability of transitions originated from state $|nl\rangle$ are now dominated by their transition dipole matrix elements, which are largest for transitions to the neighboring states $|(n \pm 1)(l \pm 1)\rangle$ because their wave functions have large spacial overlap[36].

The most widely used model to calculate the effective lifetime of Rydberg states incorporating both, radiative decay and blackbody induced transitions, was developed by Gallagher and Cooke[47]. Based on the fact that the Einstein coefficient $W^{nl}_{n'l'}$ for the stimulated emission process $|nl\rangle \rightarrow |n'l'\rangle$ is

$$W^{nl}_{n'l'} = \bar{N}(\omega^{nl}_{n'l'}, T) \times A^{nl}_{n'l'}, \tag{1.17}$$

the product of Einstein A-coefficient for spontaneous emission of the same transition and the number of photons in the blackbody radiation field at the

transition frequency $\omega^{nl}_{n'l'}$, they give the simple expression

$$W^{nl}_{n'l'} = \frac{A^{nl}_{n'l'}}{\exp\left(\hbar\omega^{nl}_{n'l'}/k_B T\right) - 1}, \tag{1.18}$$

employing the Planck distribution at temperature T to obtain the number of photons per mode, $\bar{N}(\omega^{nl}_{n'l'}, T)$. For the transitions $ns \to (n-1)p$ or $nd \to (n+1)p$, which are at microwave frequencies for Rydberg atom, the transition dipole moment $\mathfrak{d}^{n'l'}_{nl}$ is typically large and on the order of some 1000 ea_0. Inspecting (1.17) reveals that a sufficiently large number of photons N can further increase the total transition probability. This can partly compensate for the penalty due to the low transition frequency for transitions to adjacent levels in the spontaneous decay (1.14), making the blackbody induced decay comparable to the spontaneous decay. At room temperature, the transition to the closest p state is enhanced by the number of photons in the thermal field by $N = 70$ for Rb$(35s)$ states and by $N = 200$ for Rb$(45d)$.

In analogy to the case of spontaneous decay (1.15), the blackbody limited lifetime τ_{bb} is defined as the inverse of the sum over all possible blackbody-induced transitions

$$\begin{aligned} \tau_{\mathrm{bb}}(nl) &= \left[\sum_{n'l'} W^{nl}_{n'l'}\right]^{-1} \\ &= \left[\sum_{n'l'} \frac{A^{nl}_{n'l'}}{\exp\left(\hbar\omega^{nl}_{n'l'}/k_B T\right) - 1}\right]^{-1}. \end{aligned} \tag{1.19}$$

Consequently, the effective lifetime is given by the sum of the depopulation rates due to spontaneous and stimulated emission as

$$\tau_{\mathrm{eff}}(nl) = \left[\frac{1}{\tau_{\mathrm{rad}}(nl)} + \frac{1}{\tau_{\mathrm{bb}}(nl)}\right]^{-1}. \tag{1.20}$$

The calculation of the blackbody induced lifetimes can also be reduced to the calculation of the transition matrix elements of neighboring Rydberg states $\langle n'l'|\, e\mathbf{r}\,|nl\rangle$ since the photon number in selected thermal modes is determined only by temperature. Beterov et al. determined and compared the blackbody induced decay rates of rubidium[39] with experimental data[40,45,46]. Their results for the effective lifetime τ_{eff} for s, p and d states as well as the radiative lifetimes τ_{rad} of Branden et al.[41] are shown in Figure 1.3.

1.5 Interaction of Rydberg atoms

In ultra cold quantum gases, the thermal energy is so low that Rydberg atoms can be treated as fixed in space during their lifetime. On the other hand, Rydberg atoms have huge atomic orbits $r_n \propto a_0 n^2$ and the multipolar forces between Rydberg atoms which are induced by the huge dipole moments and polarizabilities of Rydberg atoms are several orders of magnitude stronger than for ground-state atoms. Depending on the angular momentum l of the Rydberg state and on the relative orientation of the Rydberg atoms with respect to external fields, these interactions can alter in strength and sign. This versatility makes Rydberg atoms a valuable ingredient in ultra cold atomic physics since one can select the state that fits best to the desired properties from a large selection.

In analogy to the classical treatment of interacting dipoles[48], the potential energy for two quantum mechanical dipoles ${}^A\mathfrak{d}^{nl}_{n'l'} = \langle n'_A l'_A | \, e\mathbf{r} \, | n_A l_A \rangle$ and ${}^B\mathfrak{d}^{nl}_{n'l'} = \langle n'_B l'_B | \, e\mathbf{r} \, | n_B l_B \rangle$ is given by

$$\begin{aligned} V_{\mathrm{dd}} &= \sum_{|n'_A l'_A\rangle, |n'_B, l'_B\rangle} \frac{\langle n'_A l'_A | \, e\mathbf{r}_A \, | n_A l_A \rangle \, \langle n'_B, l'_B | \, e\mathbf{r}_B \, | n_B, l_B \rangle}{|\mathbf{r}|^3} \\ &= \sum_{|n'_A l'_A\rangle, |n'_B, l'_B\rangle} \frac{{}^A\mathfrak{d}^{nl}_{n'l'} \times {}^B\mathfrak{d}^{nl}_{n'l'}}{|\mathbf{r}|^3}, \end{aligned} \tag{1.21}$$

omitting the angular dependence.

To obtain the characteristic properties of the interaction, one can restrict the treatment to the three Rydberg levels $|d\rangle$, $|p\rangle$ and $|f\rangle$ with energy levels E_d, E_p, E_f, respectively. Assuming that the two pair-states $|dd\rangle$ and $|fp\rangle$ are nearly degenerate, i.e. the energy defect $\Delta = (E_d - E_p) - (E_f - E_d)$ is much smaller than any other energy separation, it is sufficient to consider the two pair-states $|dd\rangle$ and $|fp\rangle$. The Hamiltonian of the system then is given by

$$\mathcal{H} = \begin{pmatrix} 0 & \frac{{}^A\mathfrak{d}^{nl}_{n'l'} \times {}^B\mathfrak{d}^{nl}_{n'l'}}{|\mathbf{r}|^3} \\ \frac{{}^A\mathfrak{d}^{nl}_{n'l'} \times {}^B\mathfrak{d}^{nl}_{n'l'}}{|\mathbf{r}|^3} & \Delta \end{pmatrix}, \tag{1.22}$$

and the eigenenergies are

$$E_\pm = \frac{\Delta}{2} \pm \sqrt{\left(\frac{\Delta}{2}\right)^2 + \left(\frac{{}^A\mathfrak{d}^{nl}_{n'l'} \times {}^B\mathfrak{d}^{nl}_{n'l'}}{|\mathbf{r}|^3}\right)^2}. \tag{1.23}$$

pair state of interest		coupled pair state	accessible n-range
$ns_{1/2} + ns_{1/2}$	$\leftrightarrow$	$np_{1/2} + (n-1)p_{1/2}$	no Förster resonances
$np_{1/2} + np_{1/2}$	$\leftrightarrow$	$ns_{1/2} + (n+1)s_{1/2}$	no Förster resonances
$np_{3/2} + np_{3/2}$	$\leftrightarrow$	$ns_{1/2} + (n+1)s_{1/2}$	all n
$nd_{5/2} + nd_{5/2}$	$\leftrightarrow$	$(n+1)p_{3/2} + (n-1)f_{7/2}$	all n
$nd_{5/2} + nd_{5/2}$	$\leftrightarrow$	$(n+2)p_{3/2} + (n-2)f_{7/2}$	resonance at $n \approx 43$
$nd_{3/2} + nd_{3/2}$	$\leftrightarrow$	$(n+1)p_{3/2} + (n-1)f_{5/2}$	all n
$nd_{3/2} + nd_{3/2}$	$\leftrightarrow$	$(n+2)p_{3/2} + (n-2)f_{5/2}$	resonance at $n \approx 39$
$nd_{3/2} + nd_{3/2}$	$\leftrightarrow$	$(n+2)p_{1/2} + (n-2)f_{7/2}$	resonance at $n \approx 58$

Table 1.4 | Förster zeros in rubidium Overview of Förster resonances for $|ss\rangle$-, $|pp\rangle$- and $|dd\rangle$-pair states of rubidium[51]

For sufficiently large internuclear separation $\mathbf{r}$, the energy defect Δ is much larger than $\frac{{}^A\mathfrak{d}^{nl}_{n'l'} \times {}^B\mathfrak{d}^{nl}_{n'l'}}{|\mathbf{r}|^3}$ and one can expand (1.23) in a Taylor series which yields for the energy shift of the state $|dd\rangle$

$$\Delta E_{\mathrm{vdW}} = E_- = -\frac{1}{\Delta}\left(\frac{{}^A\mathfrak{d}^{nl}_{n'l'} \times {}^B\mathfrak{d}^{nl}_{n'l'}}{|\mathbf{r}|^3}\right)^2 = -\frac{C_6}{|\mathbf{r}|^6}. \tag{1.24}$$

This is the van der Waals-Interaction with the C_6-coefficient defined as

$$C_6 = \frac{\left({}^A\mathfrak{d}^{nl}_{n'l'} \times {}^B\mathfrak{d}^{nl}_{n'l'}\right)^2}{\Delta}, \tag{1.25}$$

which is attractive for positive energy defects Δ and scales like $\tilde{n}^{11}$, as can be seen from $\mathfrak{d} \propto \tilde{n}^2$ and $\Delta \propto \tilde{n}^{-3}$. The C_6 coefficients for rubidium can be calculated using ref. 49.

In the absence of external fields, the energy defect is given by the atomic level structure E_{nlj} of the atomic species. Energy degeneracies of the pair states would be accidental and for rubidium there are no such degeneracies. However, the atomic energy levels E_{nlj} are shifted in external fields and it is possible to create degenerate pair states with moderate electric fields on the order of some $\mathrm{V\,cm^{-1}}$. If the energy defect Δ is shifted to zero, the two pair states $|dd\rangle$ and $|fp\rangle$ are resonantly coupled - a Förster resonance occurs[50]. An overview of pair states that can be brought into resonance is given in Table 1.4.

For vanishing energy defect $\Delta = 0$, a transition from van der Waals interac-

tion to dipole-dipole interaction occurs since the energy of the states in (1.22) are shifted by

$$\Delta E_{\text{Föster}} = \pm \frac{{}^{A}\mathfrak{d}^{nl}_{n'l'} \times {}^{B}\mathfrak{d}^{nl}_{n'l'}}{|\mathbf{r}|^3} = \pm \frac{C_3}{|\mathbf{r}|^3}. \tag{1.26}$$

Förster resonances are of experimental interest not only because they change the interaction type from $1/r^6$-van der Waals to $1/r^3$-dipole-dipole interaction but more importantly this transition can be tuned with a single control parameter, namely the electric field. This is analogous to Feshbach resonances[52], where the pair-states are shifted into resonance by a magnetic field. For the exact calculation of the interaction between two Rydberg atoms, (1.22) has to be constructed for all coupled states and must be diagonalized.

A consequence of the strong van der Waals and dipole-dipole interaction is a clipping of the Rydberg population. If two atoms are closer than the so called blockade radius r_B, the interaction energy exceeds the linewidth of the driving laser $\hbar\Omega$

$$\hbar\Omega \leq -\frac{C_6}{r_B^6} \qquad \text{resp.} \qquad \hbar\Omega \leq -\frac{C_3}{r_B^3}. \tag{1.27}$$

In this case, the excitation laser is no longer resonant to the doubly occupied Rydberg state and thus the excitation of the second atom is suppressed.

For most Rydberg states and typically accessible Rabi frequencies Ω_o on the order of few 100 kHz, the blockade radius r_B is on the order of some µm and thus much larger than the mean particle spacing $\mathcal{N}^{-1/3}$ in an ultra cold atomic sample, which is of the order of few 100 nm. Consequently, one single Rydberg excitation is shared between a large number N of ground-state atoms in a so called blockade sphere of volume $4/3\pi r_B^3$. This manifests itself in a collective excitation of the Rydberg state[53,54,55] and an enhanced Rabi frequency

$$\Omega_{\text{enh}} = \sqrt{N}\Omega_o\,, \tag{1.28}$$

where, Ω_o is the single-atom Rabi frequency. For magneto-optically trapped atoms with a low density of ground-state atoms $\mathcal{N}$, the enhancement is low, but for a Bose-Einstein condensate, an enhancement by a factor $\sqrt{N} \approx 30$ is possible[26,56].

1.6 Ultralong-range Rydberg molecules

A different kind of interaction of Rydberg atoms leads to another new state of matter. In the year 2000, Chris Greene et al. proposed a binding mechanism between an atom in its ground state and another atom in a Rydberg state that is mediated through the attraction between the electric field of the Rydberg electron and the polarizable ground-state atom[3]. That a polarizable particle is attracted by an electric field due to the displacement between electrons and the atomic core is a well known effect in classical physics. The quantum nature of atomic physics, however, demands for a quantum mechanical treatment of the problem. This implies that the interaction is treated as a scattering process between the low energy Rydberg electron and the ground-state atom.

The quantum mechanical treatment of scattering problems goes back to Enrico Fermi who introduced the concept of the scattering length and the pseudopotential in 1934[57] (see Figure 1.4 **b**). In this formalism, the scattering is described in first order by a single number accounting for the phase shift between ingoing and outgoing wave function outside the region of interaction - the s-wave scattering length A_s. The sign of the scattering length depends on whether the wave function is shifted inwards (negative scattering length) or outwards (positive scattering length), resulting in attraction or repulsion of the two particles. If $\mathbf{r}$ is the position of the Rydberg electron and $\mathbf{R}$ is the position of the ground-state atom, both with respect to the ionic core of the Rydberg atom, then the pseudopotential can be written to first order as[a]

$$V_{\text{pseudo}}(\mathbf{r},\mathbf{R}) = 4\pi A_s \delta(\mathbf{r}-\mathbf{R}). \tag{1.29}$$

To calculate the molecular potential of the ultralong-range Rydberg molecules, one needs to average the pseudopotential (1.29) over the spatial probability distribution of the Rydberg electron, which is given by its wave function $\psi_{n,l}$. One then obtains the molecular potential for a ground-state atom and a Rydberg atom in its ns state at internuclear separation r as

$$U(r) = 2\pi\, A_s(k[r])\, |\psi_{n,0}|^2, \tag{1.30}$$

where the scattering length has been replaced by an energy dependent scattering length $A_s(k[r])$ since the scattering phase depends on the kinetic energy of the electron. The shape of the energy dependence of the scattering

[a] in this section, atomic units will be used instead of SI units

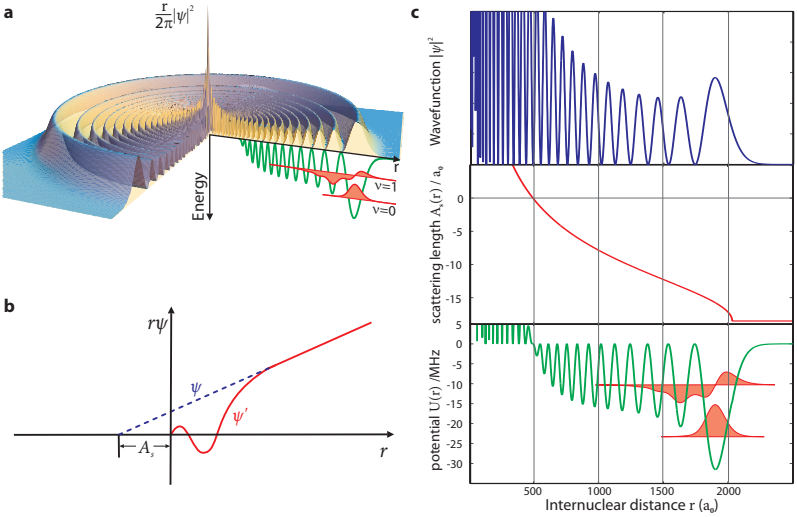

Figure 1.4 | Ultralong-range Rydberg molecules. a, Surface plot of the spherically symmetric density distribution of the Rydberg electron in the r-φ-plane. **b,** For long distances from the scattering center, ingoing (blue) and outgoing (red) wave only differ by a phase. This is equivalent to the outgoing wave being shifted by the scattering length A_s (adapted from ref. 57) **c,** The molecular potential for ultralong-range Rydberg molecules is calculated by multiplying the Rydberg electron's probability density (upper panel) and the energy dependent scattering length $A_s(k[r])$. The resulting potential for $35s$ (lower panel) supports two bound states.

length can be obtained from an effective range theory[58]. For the scattering of an electron off an alkali atom with polarizability α, which is described by a potential $V \propto \alpha/r^4$, modified effective range theory (MERT) yields[59]

$$A_s(k[r]) = A_{s,0} + \frac{\pi}{3}\alpha k(r) + \mathcal{O}(k^2), \tag{1.31}$$

with the zero-energy scattering length $A_{s,0}$. The kinetic energy of the Rydberg electron $k(r)$ can be calculated from the classical expression

$$k(r) = \sqrt{2E_{\text{kin}}} = \sqrt{2(E_{nl} + 1/r)}. \tag{1.32}$$

If one assumes that the Rydberg electron and the ground-state atom are in a triplet state, i.e. their spins are parallel, then the negative triplet scattering

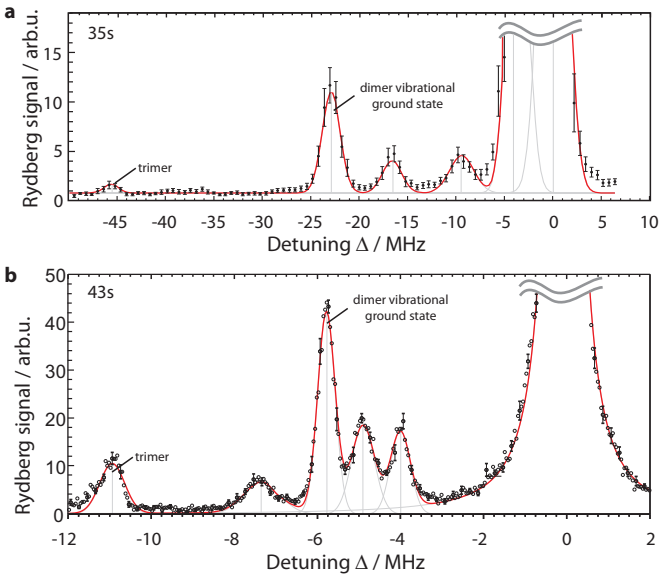

Figure 1.5 | Observation of ultralong-range Rydberg molecules for rubidium. Photo-association spectra of ultralong-range Rydberg molecules. **a,** Spectrum for $n = 35s$. The vibrational ground state and several vibrationally excited states can be observed. At twice the binding energy of the dimer state there is a trimer state where the Rydberg atoms binds two ground-state atoms. **b,** Spectrum for the $n = 43s$ state of the ultralong-rang Rydberg molecules. With a bond length of ca. 3000 a_0, these are the largest molecules of this kind observed until now.

length for rubidium gives rise to an attractive potential. For the $35s$-state of rubidium and a zero-energy scattering length of $A^T_{s,0} = -18.0 a_0$ one then obtains the potential depicted in Figure 1.4 **b**, which is ca. 30 MHz deep and supports two bound states: the vibrational ground state ($v = 0$) with binding energy $E_B = -22.5$ MHz and the first excited state ($v = 1$) at -10.1 MHz. The singlet scattering length in contrast is sightly positive, $A^S_{s,0} = 2.03\, a_0$ [60] and $A^S_{s,0} = 0.627\, a_0$ [61], and thus the molecular potential for singlet states is repulsive.

Recently, the experimental prove of the existence of this exotic binding mechanism was given by photo-associating the molecules in the setup also used for the experiments presented in this thesis [4,28]. Although the vibrational ground state can be modeled well with restricting to s-wave scattering, the observed spectra reveal several more excited molecular states that cannot be assigned

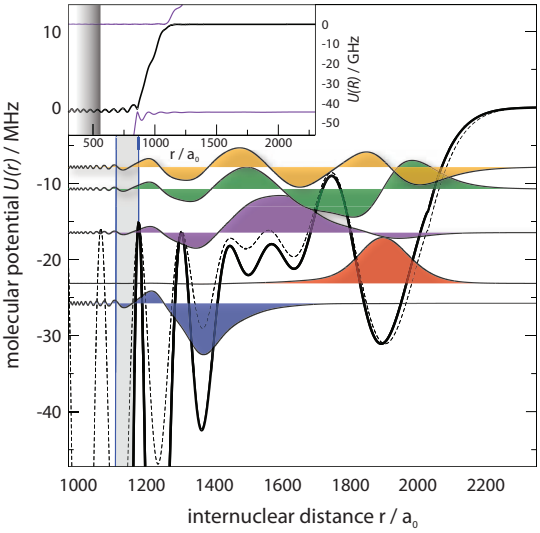

Figure 1.6 | Molecular potential curve for $^3\Sigma(35s - 5s)$ Rydberg molecules. Result of a Green's function calculation for ultralong-range Rydberg molecules (solid line) and an calculation based on MERT incorporating an effective scattering length $A_s = -19.48\, a_0$ (dashed line). Note that the best localized state (red) is not the state with lowest energy. The inset illustrates the steep potential drop of ca. 40 GHz around $r \approx 1200 a_0$

by this model (cf. Figure 1.5).

In a more sophisticated approach one can go beyond perturbation theory and consider the full Hamiltonian for the electron-atom interaction[6]. The resulting potential as well as the wave functions of the bound states is depicted in Figure 1.6. Using multimode Green's function calculations for the molecular potential reveals that there is a deep potential drop around $r \approx 1200 a_0$ (see inset of Figure 1.6) caused by a resonance in the electron-atom scattering[62]. This very special shape of the potential gives rise to bound states which can be identified as the lines unassigned by s-wave theory. Note that some of the states have binding energies smaller than the potential barriers, which means that classically these states would not be bound. It turns out that these states are stabilized in the outer region of the molecular potential by quantum reflection at the steep potential drop around $r = 1200\ a_0$[6].

From Figure 1.6 one can see, that only the vibrational ground state has vanishing probability density near the potential drop and is the only molecular

binding energy E_B / MHz	−7.8	−10.7	−16.5	−23.1	−25.9
Wigner delay time τ_{del} / μs	8.5	26.6	40.5	$\gg \tau_{\mathrm{atom}}$	14.7
decay rate $\gamma_{\mathrm{del}} = \tau_{\mathrm{del}}^{-1}$ / $10^4 \mathrm{s}^{-1}$	11.8	3.76	2.47	$\ll \gamma_{\mathrm{atom}}$	6.80

Table 1.5 | Lifetimes of bound states Lifetimes and decay rates of bound states with binding energy E_B due to transmission into the inner region of the molecular potential.

state that is bound by the outermost potential well near $r \approx 1900\, a_0$. All other bound state are stabilized by quantum reflection at the deep abyss near $r \approx 1200\, a_0$, which prevents these states from reaching smaller internuclear distances. However, the reflection is not perfect and there is a considerable probability for the state to penetrate into small internuclear separations which ultimately leads to a decay of the molecule. On the other hand, this decay allows to treat the inner region as an open boundary and the quantum reflection can be treated as an inward scattering[6].

From the asymptotic phase shift θ between ingoing and scattered wave, one can calculate the Wigner delay time

$$\tau_d = \frac{\mathrm{d}\theta}{\mathrm{d}E}, \tag{1.33}$$

which is a measure for the time that the ground-state atom needs to pass through the barrier. The values calculated by W. Li, T. Pohl and J. M. Rost for the 35s-states are summarized in Table 1.5[7]. As expected, the lifetime of the vibrational ground state at $E_B = -23.1\,\mathrm{MHz}$ is not affected by the inward scattering, since it is not bound due to quantum refection. The lifetime of the other bound states, however, is considerably shorter than the radiative and the blackbody induced lifetime of the atomic 35s-state. In chapter 7, these theoretical findings will be compared to experimental results.

2 Treating Rydberg Atoms with `rydLib`

Most of the exaggerated properties of Rydberg atoms result from their large spatial extent and the small energy spacings between the involved states, in contrast to the well separated energy levels in ground-state atoms. The most crucial ingredient for calculating the properties of Rydberg atoms is their wavefunction, since all other quantities can be described in term of expectation values and overlap integrals. This chapter will describe the `C` library `rydLib`, that has been developed in the frame of this thesis to calculate and handle wavefunctions and dipole matrix elements of rubidium. It constitutes the numerical basis for the explanation of the experimental findings presented later in this thesis.

2.1 Wavefunctions of hydrogen atoms

The hydrogen atom is a model system in atomic physics, because it is the only atom for which an analytic solution exists. The Schrödinger equation of the problem with the radial potential $V(r)$ of the electron and the energy eigenvalue E in atomic units (a.u.) reads

$$\mathcal{H}_0\psi(r,\theta,\varphi) = \left[-\frac{1}{2}\nabla^2 + V(r)\right]\psi(r,\theta,\varphi) = E\psi(r,\theta,\varphi). \tag{2.1}$$

In spherical coordinates, the Hamiltonian is given by

$$\mathcal{H}_0 = -\left[\frac{\partial^2}{\partial r^2} + \frac{2}{r}\frac{\partial}{\partial r} + \frac{1}{r^2}\left(\frac{\partial^2}{\partial\theta^2} + \cot\theta\frac{\partial}{\partial\theta} + \frac{1}{\sin^2\theta}\frac{\partial^2}{\partial\varphi^2}\right)\right] + V(r), \tag{2.2}$$

where the term in round brackets is the representation of the angular momentum operator $\hat{L}^2$ and is independent of r. Since the angular dependence is contained within $\hat{L}^2$ and the potential $V(r)$ of the electron is a central potential only depending on r, the Schrödinger equation (2.1) is separable. The eigenstates of the angular momentum operator are the spherical harmonics

$$Y_l^{m_l}(\theta,\varphi) = \sqrt{\frac{(l-m_l)!}{(l+m_l)!}\frac{2l+1}{4\pi}}P_l^{m_l}(\cos\theta)e^{im_l\varphi} \tag{2.3}$$

where $P_l^{m_l}(\cos\theta)$ are the associated Legendre polynomials. The eigenvalue of $\hat{L}^2$ is $l(l+1)$ and the eigenvalue of $\hat{L}_z$, the projection of the angular momentum along the quantization axis z, is m_l.

Using the separation ansatz $\psi(r,\theta,\varphi) = Y_l^{m_l}R(r)$ in (2.1) yields the Schrödinger equation for the radial wave function $R(r)$

$$\left[-\left(\frac{\mathrm{d}^2}{\mathrm{d}r^2}+\frac{2}{r}\frac{\mathrm{d}}{\mathrm{d}r}\right)\frac{l(l+1)}{r^2}+2V(r)\right]R(r) = 2ER(r), \tag{2.4}$$

which can formally be written as a system of ordinary first order differential equations

$$\begin{aligned}\frac{\mathrm{d}}{\mathrm{d}r}R(r) &= R'(r)\\ \frac{\mathrm{d}}{\mathrm{d}r}R'(r) &= \frac{2}{r}R'(r)+2\left(\frac{l(l+1)}{2r^2}+V(r)-E\right)R(r).\end{aligned} \tag{2.5}$$

The simplest atom in the periodic table of elements is the hydrogen atom with the core consisting only of one proton. For hydrogen, the central potential is simply the Coulomb potential of the proton, $V(r) = -1/r$. For bound states with $E < 0$, the solutions are given by

$$R_{n,l}(r) = \frac{2}{n^2}\sqrt{\frac{(n-l-1)!}{(l+n)!}}\left(\frac{2r}{n}\right)^l L_{n-l-1}^{2l+1}\left(\frac{2r}{n}\right)e^{-r/n}, \tag{2.6}$$

where the $L_{n-l-1}^{2l+1}(r)$ are the so-called generalized Laguerre polynomials of degree $n-l-1$ and n is the principal quantum number. The eigenenergies of these states are $E = -R_{\mathrm{Ryd}}/n^2$, where $R_{\mathrm{Ryd}} = 1/2$ in atomic units.

Describing the hydrogen atom with the Schrödinger equation (2.1) is exact in a non-relativistic treatment but however it is only an approximation since it does not account for the coupling of the electron spin s with its orbital angular momentum l. To account for this coupling, one needs to solve the Dirac equation for the hydrogen atoms, which adds the fine structure to the level

scheme of hydrogen. The shift of the levels with same quantum numbers for spin s and orbital quantum number l, but different total angular momentum, j, arising from this coupling is known as the Lamb Shift.

2.2 Wavefunctions of alkali atoms

For hydrogen-like atoms like rubidium, the angular dependence is fully analytic as for the hydrogen atom. The radial wave function $R(r)$, however, is not analytic since, as mentioned in section 1.1, the core charge in hydrogen-like atoms is partly screened by the inner electrons and the potential $V(r)$ for the valence electron is not fully Coulombic. While far away from the core at long range the potential is that of a single positive charge at the origin, at short range the valence electron penetrates the closed inner electron shells and is exposed to the unscreened charge of the core, Z. Additionally, the electron can polarize the core, leading to a long ranged attractive $1/r^4$ potential[63]. Since these effects are stronger as the Rydberg electron gets closer to the core, the resulting energy shift strongly depend on the angular momentum quantum number l, describing the ellipticity of the electron's orbit.

This behavior is utilized in quantum defect theory, where the principal quantum number n is corrected by the quantum defect δ_{nlj}, which mostly depends on the angular momentum quantum number, l, (see Table 1.2), but also partly on the total angular momentum, j. The corrected eigenenergies E can be calculated via

$$E = -\frac{R_{\mathrm{es}}}{(n-\delta_{nlj})^2}, \tag{2.7}$$

where R_{es} is the element specific Rydberg constant. On the other hand, (2.7) can be used to calculate the δ_{nlj} from spectroscopic data. Tabulated values for δ_{nlj} obtained in several experiments are compiled in Table 1.2.

The wave functions of hydrogen-like atoms, however, can not be calculated easily from the hydrogen wave functions, except for the high-l states, which have vanishing quantum defect and thus can be assumed hydrogenic. One approach to calculate wave functions of hydrogen-like atoms is to construct them with the help of the quantum defect from a series of the general solutions of (2.5) for $V(r) = -1/r$, the regular and irregular Coulomb wave functions[64].

	$l = 0$	$l = 1$	$l = 2$	$l \geq 3$
a_1	3.69628474	4.44088978	3.78717363	2.39848933
a_2	1.64915255	1.92828831	1.57027864	1.76810544
a_3	−9.86069196	−16.79597770	−1.65588970	−12.07106780
a_4	0.19579987	−0.81633314	0.52942835	0.77256589
r_c	1.66242117	1.50195124	4.86851938	4.79831327

Table 2.1 | Core model parameters. Parameters for calculating the core potential $V_m(r)$ for the l-states of rubidium[65].

In this thesis, another approach will be employed, where the core is described by an effective potential[65]. The effective potential is constructed using three terms: polarization potential V_p, single-electron central field V_c, and spin-orbit interaction potential V_{so}.

The polarization potential V_p represents the effect of the induced core electron dipole moments on the Rydberg electron. Neglecting quadrupole polarizability, the potential can be written as

$$V_p(r) = -\frac{\alpha_d}{2r^4}\left[1 - e^{(r/r_c)^6}\right], \tag{2.8}$$

where the static dipole polarizability is[18] $\alpha_d = 9.0760$ a.u. and the cutoff radius r_c removes unphysical short-range contribution near the origin.

The single-electron central field is the Coulomb potential caused by the core with charge Z and the closed electron shells and reads

$$V_c(r) = -\frac{Z_l(r)}{r}, \tag{2.9}$$

with the radial charge $Z_l(r)$ given by

$$Z_l(r) = 1 + (Z-1)e^{-a_1 r} - r(a_3 + a_4 r)e^{a_2 r}. \tag{2.10}$$

The parameters $a_1 \ldots a_4$ and r_c must be obtained from a fitting procedure to experimental values. The values used in this thesis are presented in Table 2.1. They are taken from ref. 18 and were obtained by fitting at least five energies per l value with an accuracy of 1 part in 10^5.

The third term in the effective potential is the spin-orbit interaction potential

which reads in the full relativistic form as[65]

$$V_{so} = \frac{\alpha^2}{2r} f(r)^2 \frac{\mathrm{d}V_m(r)}{\mathrm{d}r} \vec{l} \cdot \vec{s}, \tag{2.11}$$

with the fine-structure constant α and with

$$f(r) = \left\{1 + (\alpha^2/4)[E - V_m(r)]\right\}^{-1}, \tag{2.12}$$

where $V_m(r)$ is the model potential consisting of the core plus the polarization potentials:

$$V_m(r) = V_c(r) + V_p(r). \tag{2.13}$$

Outside the core, this can be reduced to[63]

$$V_{so} = \frac{\alpha^2}{2r^3} \vec{l} \cdot \vec{s}, \tag{2.14}$$

where

$$\vec{l} \cdot \vec{s} = \frac{1}{2}\left[j(j+1) - l(l+1) - s(s+1)\right]. \tag{2.15}$$

With the model potential $V(r)$ defined, the radial wave equations can be numerically integrated to obtain the radial wave function $R(r)$. Since the model potential does not reproduce the short range behavior near the origin correctly, care must be taken when choosing the boundary conditions and there is an inner radius, r_i, at which the calculated wave function should be truncated. On the other hand, there is no need to carry out the integration for $r \to \infty$, and the wave function can also be truncated at an outer radius r_o, where $R(r_o)$ has decayed sufficiently. Good values are $r_o = 2n(n+15)$ for the outer radius and $r_i = \sqrt[3]{\alpha_c}$ for the inner radius[63].

To minimize errors in the calculation of the radial wave function due to the core potential being only approximative, the integration should be carried out inwards, beginning at the outer starting point r_o. The truncated wave function must be normalized after calculation such that

$$\int_{r_i}^{r_o} r^2 R(r) \mathrm{d}r = 1. \tag{2.16}$$

The accuracy of the calculation can be verified when comparing $\langle r \rangle$ of the

calculated wave function with the result for the hydrogen atom

$$\langle r \rangle = \frac{1}{2}\left[3\tilde{n}^2 - l(l+1)\right]. \tag{2.17}$$

Which method is used to implement the integration depends on the purpose and the desired accuracy. Most commonly, Numerov's method is used with quadratic[66] or logarithmic[63] scaling. In this thesis, a Runge-Kutta method with adaptive step size[67] and quadratic printout points is used to solve (2.5).

Since the differential equation (2.5) is a two dimensional problem, it is not sufficient to have the the boundary condition $R_{n,l}(r_o) = 0$, but it is also necessary to start with a small, but non-vanishing slope of R_{nl}. As the outer radius is chosen sufficiently large, the exact value of $\frac{\mathrm{d}R_{nl}}{\mathrm{d}r}|_{r_o} = \epsilon$ will not affect the accuracy of the calculation, but to obtain the correct parity, the wave function must be inverted if $n - l$ is an even number.

2.3 Calculation of Dipole Matrix Elements of Rydberg Atoms

The electric dipole matrix element of an atom describes the electric coupling strength of the two atomic levels $|n,l,m_l\rangle$ and $|n',l',m'_{l'}\rangle$ and, as discussed in section 1.2 and section 1.4, the basic properties of Rydberg atoms can be derived from these matrix elements. The electric dipole operator is given by

$$\mathfrak{d} = e\mathbf{r}, \tag{2.18}$$

where e is the elementary charge and $\mathbf{r}$ the position operator. This can be expressed in its Cartesian components $\mathfrak{d}_{x,y,z}$. In the calculation of matrix elements of various operators however, it has turned out to be more convenient to classify the operators according to their behavior upon rotation of the coordinate system. It is therefore preferred to express an operator in such a way that all its components are transformed in the same way under rotation. This condition is met by the spherical harmonics Y_κ^q from (2.3), and it is convenient to define the irreducible tensors or spherical tensors of rank κ as the set of $(2\kappa - 1)$ quantities that transform under rotation of the coordinate system in the same way as the spherical harmonics $Y_\kappa^q; q = -\kappa, \ldots, \kappa$[68]. The

irreducible representation of the vector $\mathfrak{d}$ is the tensor of rank 1 given by

$$\mathfrak{d}_q = er\sqrt{\frac{4\pi}{3}}Y_1^q(\theta,\varphi). \tag{2.19}$$

This is related to the expansion of $\mathfrak{d}$ in Cartesian coordinates via

$$\begin{aligned}\mathfrak{d}_0 &= \mathfrak{d}_z \\ \mathfrak{d}_1 &= -\frac{1}{\sqrt{2}}(\mathfrak{d}_x + i\mathfrak{d}_y) \\ \mathfrak{d}_{-1} &= \frac{1}{\sqrt{2}}(\mathfrak{d}_x - i\mathfrak{d}_y).\end{aligned} \tag{2.20}$$

From the definition of the irreducible tensors it is naturally that they are separated in radial and angular part. Since one also can express the wave function of the state $|n,l,m_l\rangle$ in its radial part $R_{nl}(r)$ and the angular part $Y_l^{m_l}(\theta,\varphi)$, the calculation of the matrix elements can also be separated into the radial matrix element $\mathfrak{d}_{\mathrm{rad}}$ and the spherical matrix element $\mathfrak{d}_{\mathrm{sph}}$:

$$\begin{aligned}\langle n,l,m_l|\,\mathfrak{d}_q\,|n',l',m_{l'}'\rangle &= \langle R_{nl}|\,er\,|R_{n'l'}\rangle\sqrt{\frac{4\pi}{3}}\left\langle Y_l^{m_l}|Y_1^q|Y_{l'}^{m_{l'}'}\right\rangle \\ &= \mathfrak{d}_{\mathrm{rad}}\mathfrak{d}_{\mathrm{sph}}.\end{aligned} \tag{2.21}$$

2.3.1 Radial Electric Dipole Matrix Elements

The radial matrix elements can be directly calculated from the radial wave functions of the the two coupled atomic states by integrating

$$\mathfrak{d}_{\mathrm{rad}} = \int_0^\infty R_{n,l}^j(r)rR_{n',l'}^{j'}(r)r^2\mathrm{d}r. \tag{2.22}$$

When the radial wave functions are calculated through numerical integration of (2.5), the radial matrix element is obtained from (2.22) where the limits have to be restricted to r_i and r_o. Since Rydberg atoms have their probability density centered away from the core, the error resutling from this truncation are small. The superscript indices ^{j},$^{j'}$ in (2.22) shall remind that quantum defect δ and core potential $V(r)$ depend on the total angular momentum j due to the spin-orbit coupling. To benchmark the accuracy of the radial matrix elements calculated with `rydLib`, Table 2.2 compares results found

Matrix element	calculation	literature	deviation / %	Reference
$\langle 35d_{5/2}\|r\|33f_{7/2}\rangle$	882 ea_0	882 ea_0	< 0.1	[69]
$\langle 35d_{5/2}\|r\|37p_{3/2}\rangle$	877 ea_0	875 ea_0	0.2	[69]
$\langle 46d_{5/2}\|r\|44f_{7/2}\rangle$	1586 ea_0	1587 ea_0	< 0.1	[70]
$\langle 46d_{5/2}\|r\|45f_{7/2}\rangle$	2694 ea_0	2694 ea_0	< 0.1	[70]
$\langle 46d_{5/2}\|r\|47p_{3/2}\rangle$	2708 ea_0	2709 ea_0	< 0.1	[70]
$\langle 46d_{5/2}\|r\|48p_{3/2}\rangle$	1551 ea_0	1548 ea_0	0.2	[70]
$\langle 50d_{5/2}\|r\|48f_{7/2}\rangle$	1893 ea_0	1893 ea_0	< 0.1	[69]
$\langle 50d_{5/2}\|r\|52p_{3/2}\rangle$	1844 ea_0	1840 ea_0	0.2	[69]
$\langle 58d_{3/2}\|r\|56f_{5/2}\rangle$	2596 ea_0	2594 ea_0	< 0.1	[55]
$\langle 58d_{3/2}\|r\|60p_{1/2}\rangle$	2565 ea_0	2563 ea_0	< 0.1	[55]

Table 2.2 | Comparison of radial matrix elements. Comparison of the radial part of dipole matrix elements for rubidium found in the literature and those calculated using the C-library presented in this thesis.

in the literature with the values calculated in the frame of this thesis. The deviations are typically below 10^{-3}.

2.3.2 Spherical Electric Dipole Matrix Elements

The spherical matrix element can be directly calculated from (2.21) using Gaunt's formula[71]

$$\begin{aligned}\vartheta_{\text{sph}} &= \sqrt{\frac{4\pi}{3}}\left\langle Y_l^{m_l}\middle|Y_1^q\middle|Y_{l'}^{m'_{l'}}\right\rangle \qquad (2.23)\\ &= \sqrt{\frac{4\pi}{3}}(-1)^{m_l}\int_0^{2\pi}\int_0^{\pi} Y_l^{m_l}Y_1^qY_{l'}^{m'_{l'}}\sin\theta\,\mathrm{d}\theta\,\mathrm{d}\varphi\\ &= (-1)^{m_l}\sqrt{(2l+1)(2l'+1)}\begin{pmatrix} l & 1 & l' \\ 0 & 0 & 0\end{pmatrix}\begin{pmatrix} l & 1 & l' \\ -m_l & q & m'_{l'}\end{pmatrix},\end{aligned}$$

where the terms in round brackets denote the Wigner $3j$-symbol[68].

For rubidium, however, one has to take into account the spin-orbit coupling, and thus the good quantum numbers are $|n,l,s,j,m_j\rangle$. The decomposition of the states in fine structure representation in the uncoupled basis is done with the help of the Clebsch-Gordan coefficients $C^j_{m_1,m_2} = (j_1 j_2 m_1 m_2|j_1 j_2 jm)$[68]:

$\sqrt{\frac{4\pi}{3}}\langle l,m_l\vert\, Y_1^q \,\vert l',m'_{l'}\rangle$	$l \to l+1$	$l \to l-1$
$q=-1$ $m_l \to m_l+1$	$-\frac{1}{\sqrt{2}}\sqrt{\frac{(l+m_l+1)(l+m_l+2)}{(2l+3)(2l+1)}}$	$\frac{1}{\sqrt{2}}\sqrt{\frac{(l-m_l)(l-m_l-1)}{(2l+1)(2l-1)}}$
$q=0$ $m_l \to m_l$	$\sqrt{\frac{(l+m_l+1)^2}{(2l+3)(2l+1)}}$	$\frac{1}{\sqrt{2}}\sqrt{\frac{l^2-m_l^2}{(2l+1)(2l-1)}}$
$q=+1$ $m_l \to m_l-1$	$-\frac{1}{\sqrt{2}}\sqrt{\frac{(l-m_l+1)(l-m_l+2)}{(2l+3)(2l+1)}}$	$\frac{1}{\sqrt{2}}\sqrt{\frac{(l+m_l)(l+m_l-1)}{(2l+1)(2l-1)}}$

Table 2.3 | Integrals of spherical harmonics. List of all non-zero spherical matrix elements in the uncoupled basis $\sqrt{\frac{4\pi}{3}}\langle l,m_l\vert\, Y_1^q \,\vert l',m'_{l'}\rangle$.

$$\left|nlsjm_j\right\rangle = \sum_{m_l,m_s} C^j_{m_l,m_s}\left|nlm_lsm_s\right\rangle. \tag{2.24}$$

Noting that the spin of rubidium is $s = 1/2$ and that the spin wave functions are orthogonal, the calculation of the spherical matrix elements can be expressed as

$$\begin{aligned}\mathfrak{d}_{\text{sph}} &= \left\langle nlsjm_j\right|\mathfrak{d}_q\left|n'l's'j'm'_{j'}\right\rangle \\ &= \sum_{m_l,m'_{l'}} C^j_{m_l,m_j-m_l} C^{j'}_{m'_{l'},m'_{j'}-m'_{l'}}\,\delta_{m_j-m_l,m'_{j'}-m'_{l'}} \\ &\quad\times\sqrt{\frac{4\pi}{3}}\left\langle Y_l^{m_l}\middle|Y_1^q\middle|Y_{l'}^{m'_{l'}}\right\rangle.\end{aligned} \tag{2.25}$$

A list of spherical matrix elements in the uncoupled basis is given in Table 2.3. The spherical matrix element then can be obtained by calculation the sum in (2.25).

A more sophisticated approach takes advantage of the Wigner-Eckart theorem[72,73], which allows to decompose the matrix element in an m_j-dependent part and in a reduced matrix element $\langle j\|\mathfrak{d}_q\|j'\rangle$, which does not depend on

the orientation of the wave functions:

$$\left\langle nlsjm_j \middle| \mathfrak{d}_q \middle| n'l's'j'm'_{j'} \right\rangle = (-1)^{j-m_j} \begin{pmatrix} j & 1 & j' \\ -m_j & q & m'_{j'} \end{pmatrix} \left(j \| \mathfrak{d}_q \| j'\right). \quad (2.26)$$

The reduced matrix element in the $j - m_j$-basis can be expressed in the m_l-m_s-basis as

$$\begin{aligned} \left(j \| \mathfrak{d}_q \| j'\right) &= (-1)^{l+s+j'+1} \delta_{s,s'} \sqrt{(2j+1)(2j'+1)} \\ &\times \begin{Bmatrix} l & j & s \\ j' & l' & 1 \end{Bmatrix} \left(l \| \mathfrak{d}_q \| l'\right), \end{aligned} \quad (2.27)$$

where the term in curly brackets denotes the $6j$-symbol and the reduced matrix element in the m_l-m_s-basis is given by

$$\left\langle l \| \mathfrak{d}_q \| l' \right\rangle = (-1)^l \sqrt{(2l+1)(2l'+1)} \begin{pmatrix} l & 1 & l' \\ 0 & 0 & 0 \end{pmatrix}. \quad (2.28)$$

From the properties of the $3j$- and $6j$-symbols the following selection rules can be directly obtained:

$$|l - l'| = 1, \quad (2.29)$$

$$|j - j'| \leq 1, \text{ except } j = 0 \rightarrow j' = 0, \quad (2.30)$$

$$m_j - m'_{j'} = q. \quad (2.31)$$

2.3.3 Magnetic Dipole Matrix Elements

In analogy to the electric dipole moment, atoms can also have a magnetic dipole moment. The magnetic dipole operator is given by

$$\boldsymbol{\mu} = \mu_B \boldsymbol{\mathcal{J}}, \quad (2.32)$$

where μ_B is the Bohr magneton and $\boldsymbol{\mathcal{J}}$ is the total electronic angular momentum operator[68]. In the case of ls-coupling, one can express $\boldsymbol{\mathcal{J}}$ in terms of the orbital angular momentum $\mathbf{l}$ and the electron spin $\mathbf{s}$ as

$$\boldsymbol{\mathcal{J}} = g_l \mathbf{l} + g_s \mathbf{s} = g_l \mathbf{j} + (g_s - g_l)\mathbf{s}, \quad (2.33)$$

with the gyromagnetic ratios of orbital angular momentum, $g_l = 1$, and spin, $g_s \approx 2$, and the total angular momentum operator $\mathbf{j}$. Obviously, the magnetic dipole matrix elements do not depend on the radial wave function, but only on the orientation of the atomic state.

Assuming that the quantization axis points into z-direction , it is clear that the diagonal matrix elements are given by

$$\begin{aligned} \left\langle nlsjm_j \right| \boldsymbol{\mu} \left| nlsjm_j \right\rangle &= \mu_B \left\langle nlsjm_j \right| \mathcal{J} \left| nlsjm_j \right\rangle \\ &= g_j m_j \mu_B \mathbf{e_z}, \end{aligned} \tag{2.34}$$

where g_j is the Landé-factor

$$g_j = 1 + \frac{j(j+1) - l(l+1) + s(s+1)}{2j(j+1)}. \tag{2.35}$$

On the other hand, the total angular moment operator $\mathbf{j}$ is diagonal in the ls-basis and thus the off-diagonal elements are given by

$$\left\langle nlsjm_j \right| \boldsymbol{\mu} \left| n'l's'j'm'_{j'} \right\rangle = \mu_B \mathbf{e_z} \left\langle nlsjm_j \right| \boldsymbol{s_z} \left| nl's'j'm'_{j'} \right\rangle. \tag{2.36}$$

Applying the properties of irreducible tensor operator, it is not difficult to obtain that[68]

$$\begin{aligned} &\left\langle nlsjm_j \right| \boldsymbol{\mu} \left| n'l's'j'm'_{j'} \right\rangle \\ &= \mu_B \mathbf{e_z} (-1)^{j-m_j} \left(nlsj \| s_z \| n'l's'j' \right) \begin{pmatrix} j & 1 & j' \\ -m_j & 0 & m'_{j'} \end{pmatrix}, \end{aligned} \tag{2.37}$$

with the reduced matrix element of the electron spin operator $\mathbf{s}$ given by

$$\begin{aligned} &\left(nlsj \| s_z \| n'l's'j' \right) \\ &= (-1)^{l+1+s+j'} \sqrt{s(s+1)(2s+1)(2j+1)(2j'+1)} \begin{Bmatrix} s & j & l \\ j' & s & 1 \end{Bmatrix}. \end{aligned} \tag{2.38}$$

Again, from the properties of the irreducible tensor operatators and the reduced matrix elements $(nlsj\|\mathbf{l}\|n'l's'j')$ and $(nlsj\|\mathbf{s}\|n'l's'j')$, the selection

rules for magnetic dipole transitions are

$$|l - l'| = 0, \tag{2.39}$$
$$|j - j'| = 1, \tag{2.40}$$
$$|n - n'| = 0, \tag{2.41}$$
$$|m_j - m'_{j'}| = 0. \tag{2.42}$$

With the formulae (2.22), (2.26), (2.34) and (2.37), the electric and magnetic dipole matrix element for any two states can now be calculated.

2.4 Rydberg atoms in external fields

In the previous section, the strength of the magnetic and electric dipole coupling of two Rydberg states in external fields has been calculated. To obtain the energy corrections of the states in external fields, one has to consider the Hamiltonian

$$\mathcal{H} = \mathcal{H}_0 + \mathcal{H}_\mathcal{E} + \mathcal{H}_\mathcal{B}, \tag{2.43}$$

with the electric Hamiltonian $\mathcal{H}_\mathcal{E} = \mathfrak{d}\boldsymbol{\mathcal{E}}$ and the magnetic Hamiltonian $\mathcal{H}_\mathcal{B} = \boldsymbol{\mu}\boldsymbol{\mathcal{B}}$. $\boldsymbol{\mathcal{E}}$ and $\boldsymbol{\mathcal{B}}$ are the electric and magnetic field strengths. The corrected energies of the states in external fields are the eigenvalues E of $\mathcal{H}$.

Since this is a non-perturbative approach, all possible states $|nlsjm_j\rangle$ have to be considered in the calculation. However, due to the selection rules for dipole transitions, there are sub-spaces of states that are not coupled and can be treated independently. For the magnetic coupling, only states with the same n and l need to be considered. The strength of the electric dipole coupling $\mathfrak{d}_{\text{rad}}$ dramatically decreases as $|n - n'|$ becomes larger, and it is mostly sufficient to restrict the basis to $n_{\text{soi}} - 5 \leq n \leq n_{\text{soi}} + 5$ around the state of interest (soi). Moreover, calculation can be restricted to states of same m_j due to the selection rules (2.29).

To obtain the matrix representation of $\mathcal{H}$ in the j-m_j-basis, the matrix elements given in the previous section have to be calculated for the chosen basis states. Assuming only an electric field pointing along the z-axis, the matrix

reads

$$\begin{aligned}\mathcal{H} &= \begin{pmatrix} \langle nljm_j|\,\mathcal{H}_0 + \mathfrak{d}_0\mathcal{E}\,|nljm_j\rangle & \langle nljm_j|\,\mathcal{H}_0 + \mathfrak{d}_0\mathcal{E}\,|n'l'j'm_j\rangle & \dots \\ \langle n'l'j'm_j|\,\mathcal{H}_0 + \mathfrak{d}_0\mathcal{E}\,|nljm_j\rangle & \langle n'l'j'm_j|\,\mathcal{H}_0 + \mathfrak{d}_0\mathcal{E}\,|n'l'j'm_j\rangle & \dots \\ \vdots & \vdots & \ddots \end{pmatrix} \\ &= \begin{pmatrix} E_{nlj} & \langle nljm_j|\,\mathfrak{d}_0\mathcal{E}\,|n'l'j'm_j\rangle & \dots \\ \langle n'l'j'm_j|\,\mathfrak{d}_0\mathcal{E}\,|nljm_j\rangle & E_{n'l'j'} & \dots \\ \vdots & \vdots & \ddots \end{pmatrix}, \end{aligned} \tag{2.44}$$

and the corrected energies one obtains by diagonalization for different electric field strengths $\mathcal{E}$ can be plotted versus $\mathcal{E}$ in so called Stark maps for the $|m_j|$-manifold (e.g. Figure 1.1).

For the case of a magnetic field pointing along the z-axis, the Hamiltonian reads

$$\begin{aligned}\mathcal{H} &= \begin{pmatrix} \langle nljm_j|\,\mathcal{H}_0 + \mu_0\mathcal{B}\,|nljm_j\rangle & \langle nljm_j|\,\mathcal{H}_0 + \mu_0\mathcal{B}\,|n'l'j'm_j\rangle & \dots \\ \langle n'l'j'm_j|\,\mathcal{H}_0 + \mu_0\mathcal{B}\,|nljm_j\rangle & \langle n'l'j'm_j|\,\mathcal{H}_0 + \mu_0\mathcal{B}\,|n'l'j'm_j\rangle & \dots \\ \vdots & \vdots & \ddots \end{pmatrix} \\ &= \begin{pmatrix} E_{nlj} + g_j m_j \mu_B \mathcal{B} & \langle nljm_j|\,\mu_0\mathcal{B}\,|n'l'j'm_j\rangle & \dots \\ \langle n'l'j'm_j|\,\mu_0\mathcal{B}\,|nljm_j\rangle & E_{n'l'j'} + g_{j'} m_{j'} \mu_B \mathcal{B} & \dots \\ \vdots & \vdots & \ddots \end{pmatrix}, \end{aligned} \tag{2.45}$$

and for weak magnetic fields $\mathcal{B}$ on the order of few G, the off-diagonal terms are irrelevant and only the Zeeman shift $E_Z = g_j m_j \mu_B \mathcal{B}$ needs to be considered. When a weak magnetic field is applied additionally to an electric field, both pointing along z-direction, the only effect is the additional Zeeman shift of Stark-levels as long as the magnetic coupling is much smaller than the electric coupling.

However, the situation dramatically changes when electric and magnetic field are not parallel, but are under an angle α. In this case, the quantization axis can only be parallel to one of the external fields and the projection of the total angular momentum, m_j, is no good quantum numbers any more. In this case, it is convenient to treat the direction of the magnetic field as the z-axis. Then, the electric field is given by $(\cos\alpha \mathbf{e}_z + \sin\alpha \mathbf{e}_x)\mathcal{E}$. According to (2.20), the electric Hamiltonian then reads

$$\mathcal{H}_\mathcal{E} = \frac{1}{\sqrt{2}}[\mathfrak{d}_0 \cos\alpha + (\mathfrak{d}_{-1} - \mathfrak{d}_1)\sin\alpha]\mathcal{E}, \tag{2.46}$$

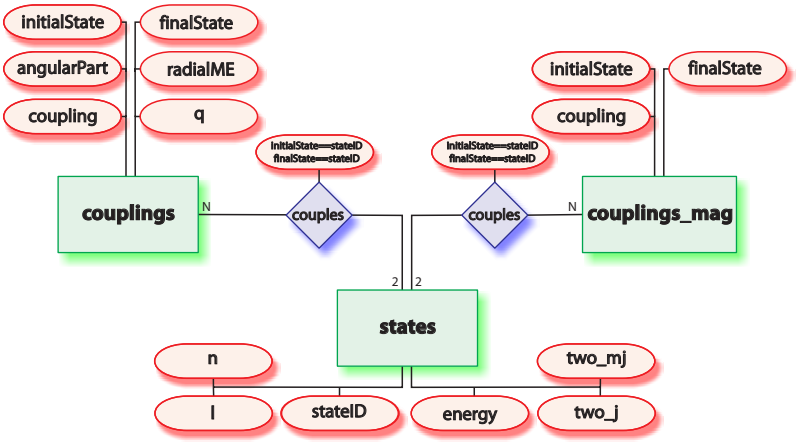

Figure 2.1 | Entity-Relationship Diagram for `rydLib`. Schematic view of the entity relationship model for the database used to store the dipole matrix elements in `rydLib` in Chen notation.

which couples states of different m_j. When calculating the Stark map in this case, one has to take into account that the $|m_j|$-manifolds are no longer decoupled and restricting the calculation to a single value of m_j will not yield the correct behavior. To obtain the correct energies for a state with total angular momentum j, at least the states with $-(j+1) \leq m_j \leq j+1$ must be taken into account.

2.5 implementation of `rydLib`

As mentioned earlier, an important and elaborate part in the calculation of properties of Rydberg atoms is the calculation of the dipole matrix elements (2.18). Among others, they are also needed for the calculation of radiative decay rates and interaction strengths.

The calculation of each matrix element employs numerical integration of the Schrödinger equation (2.4) for the radial wave functions $|\psi\rangle, |\psi'\rangle$ as well as numerical integration of the expectation value $\langle\psi| r |\psi'\rangle$. Additionally, the angular part (2.27) also needs to be evaluated. Although this procedure can be optimized by dismissing matrix elements forbidden by the selection rules at the first step already and by caching calculated wave functions, a considerable

```
CREATE TABLE states(  stateID integer primary key,
                      n integer,
                      l integer,
                      two_j integer,
                      two_mj integer,
                      energy numeric,
                      energyTHz numeric,
                      energycm numeric,
                      UNIQUE(n, l, two_j, two_mj));
CREATE INDEX idx_states ON (n, l, two_j, two_mj);
```

Listing 2.1 | create_database_states.sqlite

effort in each calculation of the properties of Rydberg atoms is spent on the calculation of dipole matrix elements. To overcome this bottleneck, `rydLib` adopts a database backend to store and retrieve the matrix elements that have been precomputed already. This allows a massive speedup compared to calculating each matrix element at runtime.

The logical layout of the database is shown in Figure 2.1 . It consists of three tables, but can be extended to enlarge its capabilities. The `states`-table is the central part of the database since it uniquely connects a `stateID` with a state $|n,l,j,m_j\rangle$. The SQL-code to create the table is shown in Listing 2.1.

The relevant tables for the calculation of the properties of Rydberg atoms, however, are the tables `couplings` and `couplings_mag`. These tables are used to store the electric and magnetic dipole matrix elements. Since a state is unambiguously identified by its `stateID`, storing the parameters $|n,l,j,m_j\rangle$ in the `couplings` tables can be omitted. This allows to reduce the redundancy in the stored data and thus leads to a speedup when searching and retrieving data from the database. The powerful engines of relational database make it possible to still retrieve entries from the `couplings`-table based on properties stored in the `states`-table by joining both tables. The SQL-code to create the tables is shown in Listing 2.2.

The first step when using `rydLib` is to fill the `states`-table. Typically, only states with $|m_j| < 11/2$ are needed when dealing with low-l Rydberg states. For the range of $5 \leq n \leq 90$, there are 89 762 states with $|m_j| < 11/2$. Note that including all m_j substates means a total number of 477 870 states for $5 \leq n \leq 90$. New states can be added at any later time. However, the radial matrix element does not depend on m_j and thus only few thousand radial matrix elements need to be calculated at all.

```
CREATE TABLE couplings(initialState integer,
                       finalState integer,
                       coupling numeric,
                       radialME numeric,
                       angularPart numeric,
                       q integer,
                       UNIQUE (initialState, finalState, q));
CREATE INDEX idx_couplings ON (initialState, finalState, q);

CREATE TABLE couplings_mag(initialState integer,
                           finalState integer,
                           coupling numeric,
                           UNIQUE (initialState, finalState));
CREATE INDEX idx_couplings_mag ON (initialState, finalState, q);
```

Listing 2.2 | create_database_couplings.sqlite

In the second step, the matrix elements are calculated and fed into the database. This can be done in advance for a large set of state pairs or at runtime for the necessary couplings. Since it is reasonable to store only nonzero couplings, pre-calculation is preferred. `rydLib` includes a `C`-program to calculate the dipole matrix elements. It calculates the wave functions of the two states by numerical integration of (2.5) with the ODE-solver provided by the GNU Scientific Library (GSL)[67]. The wave functions are calculated on a nodal grid with quadratic stepping, i.e. the kth point r_k is at $r_k = r_0 k^2$. As the wave functions have oscillatory character with wavelength scaling like $\sqrt{r}$, this yields equal numbers of nodes per wavelength. Since this allows to reduce the total number of nodes, the calculation of the overlap integral of the two wave functions is speeded up and thus also the calculation of the matrix elements.

3 Bloch Model

3.1 Equation of motion for two-level systems

The quantum mechanical treatment of a two level system is at the heart of quantum mechanics and many different but equivalent approaches are commonly used to model the interaction between a two level atom and the electromagnetic field. Generally, the interaction is described by the Hamiltonian[74]

$$\mathcal{H} = \mathcal{H}_A + \mathcal{H}_F + \mathcal{H}_{AF}, \tag{3.1}$$

where $\mathcal{H}_A$ is the atomic Hamiltonian, $\mathcal{H}_F$ is the Hamiltonian of the light field and $\mathcal{H}_{AF}$ describes the interaction.

For a two level atom of mass m with ground state $|g\rangle$ and excited state $|e\rangle$ and transition frequency ω_o, $\mathcal{H}_A$ can be expressed as

$$\mathcal{H}_A = \frac{p^2}{2m} + \hbar\omega_o |e\rangle\langle e|. \tag{3.2}$$

The interaction between atoms and light fields can be described adequately in the electric dipole approximation, which assumes that the size of the atom is much smaller than the wavelength of the radiation. In this approximation $\mathcal{H}_{AF}$ can be written as

$$\mathcal{H}_{AF} = -d\hat{\epsilon}(|e\rangle\langle g| + |g\rangle\langle e|)\hat{\mathbf{E}}(\mathbf{r},t), \tag{3.3}$$

where d is the atomic dipole moment along the quantization and ϵ is the unit vector pointing along its direction. The electric field operator at the atom's center of mass is denoted by $\hat{\mathbf{E}}$.

The Hamiltonian of the light field can be expressed through creation and annihiliaton operators of the modes κ, $\hat{a}_\kappa^\dagger$ and $\hat{a}_\kappa$, as

$$\mathcal{H}_F = \sum_\kappa \hbar\omega_\kappa \hat{a}_\kappa^\dagger \hat{a}_\kappa, \tag{3.4}$$

which is a fully quantum mechanical treatment. Throughout this thesis, it is sufficient to treat the electric field as a classical field:

$$\mathbf{E}(\mathbf{r},t) = \hat{\epsilon}(\mathbf{r})\mathcal{E}(\mathbf{r})\cos\left[\omega t + \Phi(\mathbf{r})\right], \tag{3.5}$$

where ω is the frequency and $\hat{\epsilon}(\mathbf{r})$ is the polarization. The amplitude is given by $\mathcal{E}(\mathbf{r})$. However, the classical treatment also neglects the dissipative dynamics and thus a phenomenologic decay needs to be included later. The interaction Hamiltonian then yields the form

$$\mathcal{H}_{AF} = \hbar\Omega_o(\mathbf{r})\left(\cos\left[\omega t + \Phi(\mathbf{r})\right]|e\rangle\langle g| + H.c.\right), \tag{3.6}$$

where $\Omega_o(\mathbf{r}) = -d\mathcal{E}(\mathbf{r})/\hbar$ is the Rabi frequency.

To obtain the evolution of the atoms, it is convenient to introduce the detuning $\Delta = \omega - \omega_o$ together with employing the rotating wave approximation[75] and to express the equations of motion in a frame rotating at the frequency ω of the light field. In the density matrix formalism, the equations of motion take the form

$$\begin{aligned}
\dot{\rho}_{ee} &= -\frac{i\Omega_o}{2}\left(\rho_{ge} - c.c.\right) \\
\dot{\rho}_{gg} &= +\frac{i\Omega_o}{2}\left(\rho_{ge} - c.c.\right) \\
\dot{\rho}_{eg} &= i\Delta\rho_{eg} + \frac{i\Omega_o}{2}(\rho_{ee} - \rho_{gg}),
\end{aligned} \tag{3.7}$$

where ρ_{ee} and ρ_{gg} are the populations of the levels $|e\rangle$ and $|g\rangle$ and $\rho_{eg} = \rho^*_{ge}$ is the electronic coherence.

Due to its mathematical equivalence to the Bloch equations[76], which is set of equation that is used in NMR and ESR to calculate the nuclear magnetization M, the equations of motion (3.7) can be formulated as the optical Bloch equations[77]

$$\begin{aligned}
\dot{u} &= -\Delta\, v \\
\dot{v} &= \Delta\, u + \Omega_o\, w \\
\dot{w} &= -\Omega_o\, v.
\end{aligned} \tag{3.8}$$

Here, $u = 1/2(\rho_{eg} + \rho_{ge})$ denotes the dipole moment, $v = i/2(\rho_{ge} - \rho_{eg})$ the dipole current and $w = 1/2(\rho_{ee} - \rho_{gg})$ the population inversion of the atomic

system. The population of the excited state $|e\rangle$ is given by $S = \frac{w+1}{2}$. The optical Bloch equations can also be formulated as a single vector precession equation

$$\frac{\mathrm{d}}{\mathrm{d}t}\vec{\rho} = \vec{\Omega}_0 \times \vec{\rho}, \tag{3.9}$$

where $\vec{\rho} = (u,v,w)$ is the Bloch vector and $\vec{\Omega}_0 = (-\Omega_0,0,\Delta)$ is the torque. This allows one to consider the temporal evolution of the Bloch vector as a rotation about the $\vec{\Omega}_0$ axis. Note that the motion of the Bloch vector can be separated into an energy-conserving precession about the $(0,0,\Delta)$-vector and a rotation about the $(\Omega_0,0,0)$-vector that transfers energy between the atomic system and the light field. The analytic solution of (3.9) is represented by a complicated rotation of the vector of initial values $\vec{\rho}_0$[78]. In the case of an atom that is initially in its ground state $\vec{\rho}_0 = (0,0,-1)$ and is driven at constant Rabi frequency Ω_0 and detuning Δ, the population of the excited state is

$$S(t) = \frac{\Omega_0^2}{\Omega^2}\sin(\frac{1}{2}\Omega t)^2, \tag{3.10}$$

with the effective or generalized Rabi frequency $\Omega = \sqrt{\Omega_0^2 + \Delta^2}$.

Due to the classical treatment of the electro-magnetic field when deducing the optical Bloch equations, they do not account for decay. To introduce a phenomenological decay, it is convenient to follow the approach proposed by Bloch[76] for nuclear spins and to introduce the longitudinal T_1-time and the transversal T_2-time. The terms longitudinal and transversal refer to the theory of magnetic resonance, where the two decay times are governed by the decay parallel with and orthogonal to the static magnetic field, respectively.

In atomic physics, the T_1-time models the energy non-conserving decay from the excited state to the ground state and describes the population decaying to the ground state via spontaneous emission. T_2 is the coherence lifetime that accounts for the loss of coherence and is energy conserving. The optical Bloch equations then take the form[78,79]

$$\begin{aligned}
\dot{u} &= -\Delta\, v - \frac{u}{T_2} \\
\dot{v} &= \Delta\, u + \Omega_0\, w - \frac{v}{T_2} \\
\dot{w} &= -\Omega_0\, v - \frac{w+1}{T_1}.
\end{aligned} \tag{3.11}$$

In most atom optics textbooks, the decay times T_1 and T_2 are combined to a single decay rate $\Gamma = 1/T_1$ and $T_2 = 2T_1$[74,80]. Generally, T_2 can never exceed $2T_1$ since loss of population also affects the coherence of the system.

3.2 Evolution of the optical Bloch equations

While the evolution of the undamped optical Bloch equations (3.8) can be solved analytically for arbitrary Rabi frequency Ω_0 and detuning Δ, the introduction of the T_1- and T_2-relaxation times makes it impossible to give an arbitrary analytic solution. However, there are two special cases of particular experimental interest for which an analytic solution is feasible.

The first of these cases is the steady-state solution which allows one to extract the spectral response of the system, i.e. its lineshape. if one sets $\dot{\tilde{\rho}} = 0$, one finds

$$\begin{aligned} u_{\mathrm{eq}}(\Delta) &= \frac{(\Delta T_2)(\Omega_0 T_2)}{1 + (\Delta T_2)^2 + T_1 T_2 \Omega_0^2} \\ v_{\mathrm{eq}}(\Delta) &= -\frac{(\Omega_0 T_2)}{1 + (\Delta T_2)^2 + T_1 T_2 \Omega_0^2} \\ w_{\mathrm{eq}}(\Delta) &= -\frac{1 + (\Delta T_2)^2}{1 + (\Delta T_2)^2 + T_1 T_2 \Omega_0^2}. \end{aligned} \tag{3.12}$$

To obtain the lineshape of the two-level system with the phenomenological decay times, one calculates

$$S_{\mathrm{eq}}(\Delta) = \frac{1}{2}\left(1 + w_{\mathrm{eq}}(\Delta)\right) = \frac{\left(T_1/2T_2\right)\Omega_0^2}{\Delta^2 + 1/T_2^2\left(1 + T_1 T_2 \Omega_0^2\right)}, \tag{3.13}$$

which is a Lorentzian lineshape with linewidth $\gamma = \left(2/T_2\right)\sqrt{1 + T_1 T_2 \Omega_0^2}$, also being its full width at half maximum (FWHM)[78].

The second case, where an analytic solution is feasible is that of exact resonance, $\Delta = 0$. The solution has been given first by Torrey[81] for a nuclear spin system. Since he only treats the case of one particular initial condition and a slightly different equation of motion, the general solution of (3.11) will be deduced in the following, where for the sake of readability the decay rates $\gamma_1 = 1/T_1$ and $\gamma_2 = 1/T_2$ will be used instead of the lifetimes.

Applying the Laplace transform

$$\mathcal{L}\left[\tilde{f}(p)\right] = \int_0^\infty f(\tau)e^{-p\tau}\mathrm{d}\tau \tag{3.14}$$

to the equation of motion (3.11) leads to a system of linear equations in the Laplace transforms $\{\tilde{u},\tilde{v},\tilde{w}\}$ of the Bloch vector $\{u,v,w\}$:

$$\begin{aligned} (p+\gamma_2)\tilde{u} + \Delta\tilde{v} &= u_0 \\ -\Delta\tilde{u} + (p+\gamma_2)\tilde{v} - \Omega_0\tilde{w} &= v_0 \\ \Omega_0\tilde{v} + (p+\gamma_1)\tilde{w} &= w_0 - \frac{\gamma_1}{p}, \end{aligned} \tag{3.15}$$

where $\{u_0, v_0, w_0\}$ are the initial values of $\{u,v,w\}$. Like any system of linear equations, also (3.15) can be solved using Cramer's rule.

The solution for the three components of the transformed Bloch vector, $(\tilde{u},\tilde{v},\tilde{w})$, are

$$\{\tilde{u},\tilde{v},\tilde{w}\}(p) = \frac{g_{u,v,w}}{pD_T(p)} \tag{3.16}$$

with the determinant of the coefficients

$$D_T(p) = (p+\gamma_2)^2(p+\gamma_1) + \Omega_0^2(p+\gamma_2) + \Delta^2(p+\gamma_1) \tag{3.17}$$

and the $g_{u,v,w}$ given by

$$\begin{aligned} g_u &= u_0 p\left[(p+\gamma_1)(p+\gamma_2) + \Omega_0^2\right] - \Delta v_0 p(p+\gamma_1) + \Delta\Omega_0^2 \\ g_v &= v_0 p(p+\gamma_1)(p+\gamma_2) + \Omega_0(p+\gamma 2)(w_0 p - \gamma_1) + \Delta u_0 p(p+\gamma_1) \\ g_w &= (p+\gamma_2)^2(w_0 p - \gamma_1) - \Delta\Omega_0 u_0 p - (p+\gamma_2)\Omega_0 v_0 p + \Delta^2(w_0 p - \gamma_1). \end{aligned} \tag{3.18}$$

From (3.17) it is clear that the equation $D_T(p) = 0$ will have at least one real negative root and one can factorize the determinant as

$$D_T(p) = (p+a)\left[(p+b)^2 + s^2\right]. \tag{3.19}$$

Applying the partial fraction expansion to (3.16) and the inverse of the Laplace

transform (3.15) then yields the solutions

$$\begin{aligned} u(t) &= A_u e^{-at} + \left[B_u \cos(st) + \frac{1}{s} C_u \sin(st) \right] e^{-bt} + D_u \\ v(t) &= A_v e^{-at} + \left[B_v \cos(st) + \frac{1}{s} C_v \sin(st) \right] e^{-bt} + D_v \\ w(t) &= A_w e^{-at} + \left[B_w \cos(st) + \frac{1}{s} C_w \sin(st) \right] e^{-bt} + D_w. \end{aligned} \tag{3.20}$$

The terms $A_{u,v,w}$ and $D_{u,v,w}$ can be found from

$$A_{u,v,w} = \lim_{p \to -a} (p+a) \cdot \{\tilde{u}, \tilde{v}, \tilde{w}\}; \qquad D_{u,v,w} = \lim_{p \to 0} p \cdot \{\tilde{u}, \tilde{v}, \tilde{w}\}, \tag{3.21}$$

and the $B_{u,v,w}$ and $C_{u,v,w}$ from the inital conditions at $t = 0$.

For vanishing detuning $\Delta = 0$, the roots of the determinant (3.17) are $a = \gamma_2$, $b = 1/2(\gamma_1 + \gamma_2)$ and $s^2 = \Omega_0^2 - 1/4(\gamma_2 - \gamma_1)^2$. One then obtains the coefficients

$$\begin{aligned} A_w &= 0; \quad B_w = \frac{\gamma_1 \gamma_2}{\Omega_0^2 + \gamma_1 \gamma_2} + w_0; \quad D_w = -\frac{\gamma_1 \gamma_2}{\Omega_0^2 + \gamma_1 \gamma_2} \\ C_w &= \frac{\gamma_1 + \gamma_2}{2} \frac{\gamma_1 \gamma_2}{\Omega_0^2 + \gamma_1 \gamma_2} - + \frac{\gamma_1 - \gamma_2}{2} w_0 - \Omega_0 v_0 - \gamma_1 \end{aligned} \tag{3.22}$$

$$\begin{aligned} A_v &= 0; \quad B_v = \frac{\Omega_0 \gamma_1}{\Omega_0^2 + \gamma_1 \gamma_2} + v_0; \quad D_v = -\frac{\Omega_0 \gamma_1}{\Omega_0^2 + \gamma_1 \gamma_2} \\ C_v &= \frac{\gamma_1 + \gamma_2}{2} \frac{\Omega_0 \gamma_1}{\Omega_0^2 + \gamma_1 \gamma_2} + \frac{\gamma_1 - \gamma_2}{2} v_0 + \Omega_0 w_0 \end{aligned} \tag{3.23}$$

and finally

$$A_u = -u_0 \quad B_u = 2u_0 \quad C_u = 0 \quad D_u = 0, \tag{3.24}$$

which implies that $u \equiv 0$, if $u_0 = 0$.

Part II

Experimental Setup

One crucial part for any experimental investigation is the setup where the experiments are conducted. The setup for the experiments presented in this thesis is very special in its configuration. The largest part is devoted to the preparation of an ultra cold sample of ^{87}Rb atoms starting at a 160 °C hot gas. Even the creation of Bose-Einstein condensates is possible in this setup. Apart from many other cold atoms experiments, the creation of ultra cold samples in this setup is not the goal but just the prerequisite for the actual part of the experiment.

The second important part of the setup is the laser system for the excitation of Rydberg states. It has been designed to allow for a total line width below 100 kHz to provide laser light that is narrower than the physical limits of the investigated Rydberg transitions. The combination of ultra cold samples and a narrow band excitation system dedicates this setup to the investigation of the topic in the field of Rydberg atom that are mostly discussed right now: ultralong-range Rydberg molecules, coherence and interaction.

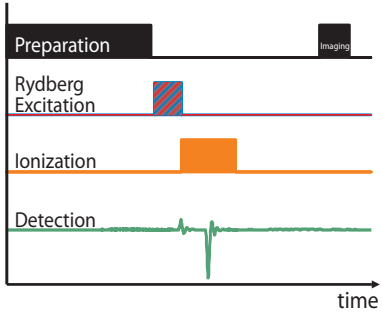

Figure 3.1 | Sequence. Schematic view of the experimental setup sequence.

This chapter will be divided into two parts, just as the experimental setup it describes. In the first part, chapter 4, the preparation of the ultra cold ground-state atoms will be described, along with the tools that the setup offers to manipulate the ground-state atoms and to finally detect them at the end of the sequence. The description will focus on the parts which are important for this thesis; a thorough discussion of the setup is given in the diploma thesis of U. Raitzsch[82] and the dissertation of R. Löw[83]. The second part, chapter 5, will focus on the laser system to create and manipulate Rydberg atoms and ultralong-range Rydberg molecules. Finally, this chapter will close with a description of the scheme for the detection of Rydberg atoms along with a discussion of the software to post-process the measured data.

4 Trapping and manipulating ultra cold atoms

The vacuum chamber is the central part of the experiment. Hot atoms are cooled down, the ultra cold atomic sample is created and excited to the Rydberg state and finally the Rydberg atoms are detected in the chamber.

The design of the chamber is adapted from the setup of BEC-chambers from the Ketterle group at the MIT[84]. Creating an atomic sample starts with an effusive oven filled with rubidium at 160 °C. The effusive beam is directed through a differential pumping stage into the Zeeman slower. A mechanical shutter intercepts the atomic beam before the Zeeman slower when loading is finished. The Zeeman slower is 0.85 m long and slows down the atoms by Doppler cooling with a counter propagating resonant laser beam[85]. The Zeeman shift created by an external offset magnetic field, that increases as the atoms approach the experimental chamber, compensates the decreasing Doppler shift as the atoms are decelerated. At the end of the Zeeman slower, an atomic flux of ca. 3×10^{12} atoms/s is reached.

When the atoms leave the Zeeman slower, they are cold enough to be trapped in a magneto-optical trap (MOT). The MOT is constituted by six counter propagating laser beams and a magnetic quadrupole field that is created by two coils in anti Helmholtz configuration. The cooling transition of Zeeman slower and MOT is the $5s_{1/2}\ (f = 2) \rightarrow 5p_{3/2}\ (f = 3)$ and repumping lasers on the $5s_{1/2}\ (f = 1) \rightarrow 5p_{3/2}\ (f = 2)$ transition pump atoms in the $f = 1$ ground state back into the cooling cycle. While the light for the cooling transitions is created from a Ti:Sa laser, the repumping light is created from a diode laser. After a loading time of 5 s, a sample of approximately 5×10^9 atoms at a temperature of few mK can be created. A subsequent molasses cooling with all magnetic fields turned off further decreases the temperature to about 20 µK.

Before loading the atoms into the magnetic trap, their spins need to be aligned again since they were depolarized during the molasses phase. This is again done with the trapping lasers at the $5s_{1/2}(f = 2) \rightarrow 5p_{3/2}(f = 3)$ transition and a small magnetic field turned on. Afterwards, the clover leaf type magnetic trap is ramped up and the atoms are compressed from a round cloud of ca. 3 mm in the MOT to a cigar shaped sample of ca 3×10^9 atoms with a

radial extent of 160 µm and a length of 2 mm. To decrease size and temperature of the atomic sample and to increase its density, the atoms are cooled further with forced evaporation cooling. Since the m_f magnetic sublevels are split in the magnetic field of the magnetic trap, radiation at radio frequencies (RF) can drive transitions between the substates. Thereby trapped atoms in the $m_f = 2$ resonant to the RF-field are gradually transfered into the untrapped $m_f = -2$ state. The magnetic field in the trap rises quadratically from the center and thus only hot atoms can reach the magnetic fields where the radio frequency is resonant. By reducing the frequency little by little from 45 MHz to ca. 1 MHz, only the hottest atoms are carefully removed and therefore the remaining are cooled by rethermalization. At the end, samples of ca. 3×10^6 atoms at temperatures of few µK are prepared for Rydberg excitation.

Following the Rydberg experiments, the magnetic trap is turned off and the atomic cloud is released. After a variable time of flight of typically 20 ms, an imaging laser is turned on and the transmitted light is recorded on a CCD camera. From the absorption profile, the number of ground-state atoms and the size of the cloud are evaluated. Temperature and density of ground-state atoms of the atomic samples can be calculated from these values.

In the magnetic trap, the atoms are trapped as long as their magnetic moment is parallel to the magnetic field. Thus there must always be a magnetic offset field B_0 to ensure that no Majorana spin flips occur[86]. Normally, the offset field in a magnetic trap is determined by the geometry of the copper coils and can not be changed. This setup, however, employs two additional power supplies to tune the current through the bias coils, thus tuning the magnetic offset field, B_0 [27]. Note that the magnetic offset field also affects size and shape of the trap.

To measure the strength of B_0, a microwave resonant to the hyperfine splitting between the $5s_{1/2}$ $(f = 2, m_f = 2)$ and the $5s_{1/2}$ $(f = 1, m_f = 1)$ states at $\nu_0 = 6.834\,683$ GHz can be used. The Landé-factors are $g_2 = 1/2$ and $g_1 = -1/2$, respectively, and thus the $f = 1, m_f = 1$-state is not magnetically trapped. Since these two levels shift differently in magnetic fields, the offset field B_0 can be found spectroscopically when monitoring the atom loss due to resonantly pumping atoms from the trapped $5s_{1/2}$ $(f = 2, m_f = 2)$-state into the untrapped $5s_{1/2}$ $(f = 1, m_f = 1)$-state at the resonant frequency ν. The magnetic offset field then is determined by

$$B_0 = \frac{2}{3}\frac{h}{\mu_B}(\nu - \nu_0). \tag{4.1}$$

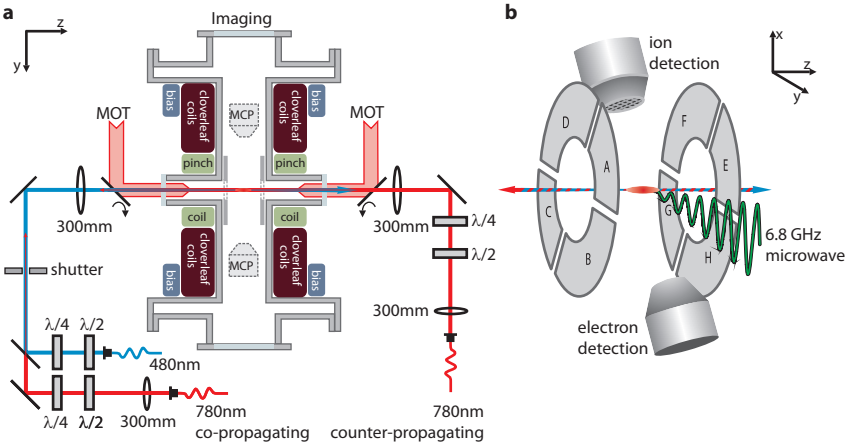

Figure 4.1 | Experimental setup for trapping and Rydberg excitation. a, View from above on the experimental chamber. The MOT-beams enter the chamber via a movable mirror that is flipped down when the atoms are magnetically trapped to clear the way for the Rydberg beams. The magnetically trapped sample is cigar shaped due to the different axial and radial trapping frequencies of the magnetic trap constituted of pinch coils, bias coils and cloverleaf coils. The laser beams for Rydberg excitation cross the chamber along the z-axis and, depending on the experimental scheme, the red beam can be co- or counter-propagating with respect to the blue beam. **b,** Stereoscopic view on the two four-fold segmented field plates and the two micro-channel plates for detection of ions and electrons.

Moreover, the microwave generator can also be used to deliberately remove atoms from the trap without heating the sample by pumping ground-state atoms from the $5s$ $(f = 2, m_f = 2)$ state into the magnetically untrapped $5s$ $(f = 1, m_f = 1)$-state. This is of particular interest when the density of the sample shall be varied without changing the other trapping parameters, e.g. to find how a given property scales with the density of ground-state atoms, $\mathcal{N}$. The microwave frequency must be varied slowly, to make sure that the transition is adiabatic. With the duration of the Landau-Zener sweep, the number of transfered atoms and thus $\mathcal{N}$ can be varied[87]. More details on the setup for cooling and trapping rubidium atoms can be found in the dissertations of Robert Löw[83] and Ulrich Raitzsch[27].

5 Laser setup for Rydberg excitation

Exciting Rydberg states of rubidium with principal quantum numbers $n > 20$ requires lasers at a wavelength below 300 nm as the ionization energy of the $5s_{1/2}$ ground state is $33\,691\,\mathrm{cm}^{-1}$. However, it is unfavorable to employ laser light around 300 nm since the only available laser sources are dye lasers that either provide low power in cw mode or have large line widths in pulsed mode. Additionally, ultra violet light is considerably absorbed in ambient air, demanding for the laser and the beams being operated under vacuum.

To overcome these problems, a two-photon transition via the $5p$-states of rubidium can be used. Even if the detuning from the intermediate state is chosen sufficiently large that the intermediate state will not be populated, the effective two-photon Rabi frequency still can be on the order of few 100 kHz. Choosing a two-photon excitation has several advantages:

- For both wavelengths required to excite Rydberg states, 780 nm and 480 nm, diode lasers are available. This allows for an easy maintaining and a narrow line width. The power available allow for an effective two-photon Rabi frequency that is higher than for a one-photon transition.
- ns- and nd-states can be addressed instead of only np-states. ns-states are of particular interests since their interaction is always repulsive, whereas nd-states offer a rich variety of states showing Förster resonances and interactions that depend on the angle between internuclear axis and quantization axis.
- Another advantage of two-photon transitions is the possibility for excitation with counter-propagating laser beams allowing to reduce the Doppler shift due to the thermal motion of the atoms. This also makes pump and probe experiments like electromagnetically induced transparency or four-wave mixing experiments possible.

In this thesis, the $35s$-state will be addressed when regarding the creation of ultralong-range Rydberg molecules, since this state has been thoroughly covered theoretically already[6]. Moreover, the d-states with $n = 45 - 47$ are also addressed in the scope of this thesis since the Förster resonance near the

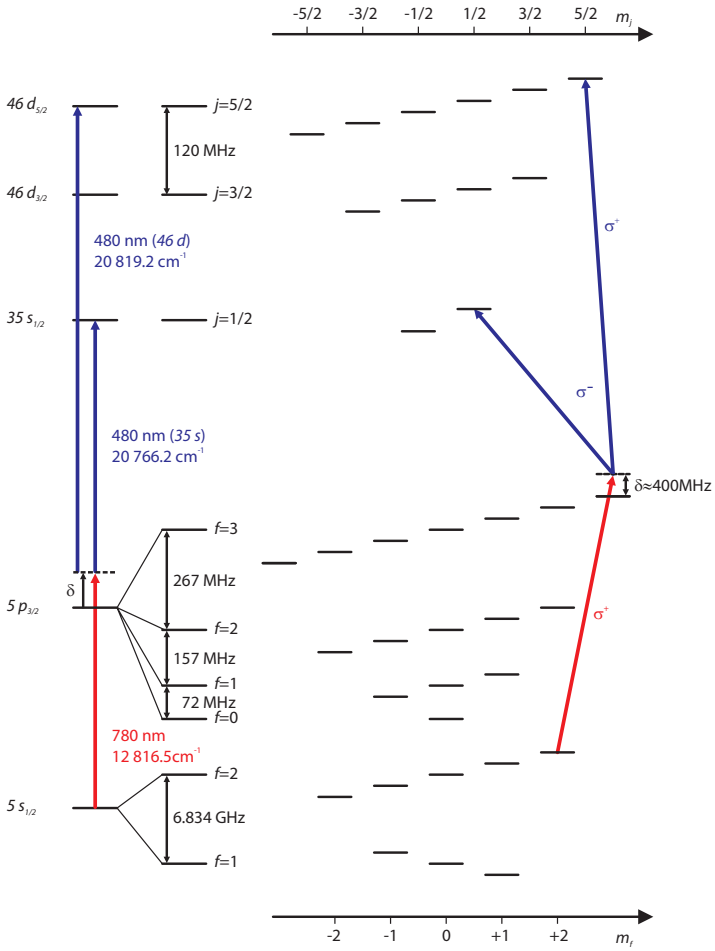

Figure 5.1 | Rydberg level scheme of ^{87}Rb. Schematic view of the energy levels of the Rb isotope ^{87}Rb with nuclear spin $i = 3/2$. The left panel shown the level splitting due to fine-structure and hyperfine-structure splitting as well as the wavelengths of the lasers to drive the two-photon excitation. For the Rydberg states, hyperfine splitting can be neglected.
The right panel shows the lifting of the degenerate magnetic sublevels in a magnetic field according to their magnetic quantum number: m_f for $5s$- and $5p$-states, m_j for Rydberg states. The excitation into the $35s(m_j = 1/2)$-state is via σ^+-σ^- polarization, and σ^+-σ^+ polarization into the $46d(j = 5/2, m_j = 5/2)$-state.

$46d_{5/2}$-state is extraordinarily strong. The essential part of the level scheme of rubidium including ns- and nd-states is depicted in Figure 5.1.

The excitation to the Rydberg states starts in the $5s_{1/2}$ $(f = 2, m_f = 2)$ ground state. The excitation path is chosen such that the Rabi frequencies of the transition to the intermediate $5p_{3/2}$ state and the final Rydberg state are maximal. Since only the angular parts of the transition dipole matrix elements depend on the magnetic substates, these have to be maximized. For transitions to the ns $m_j = 1/2$-states, this can be achieved by choosing σ^+ polarization for the red laser and σ^- polarization for the blue laser. For transitions to the nd $m_j = 5/2$-states, σ^+ polarization is chosen for both laser. To avoid population of the intermediate $5p_{3/2}$ state and heating due to absorption, the red laser is ca. 400 MHz blue detuned from that level. Note that the ground states has the same magnetic moment as the ns $m_j = 1/2$-states, an thus the transition frequency to these states does not depend on the magnetic field. The frequency at which the nd $m_j = 5/2$-states can be excited, however, shifts in magnetic fields.

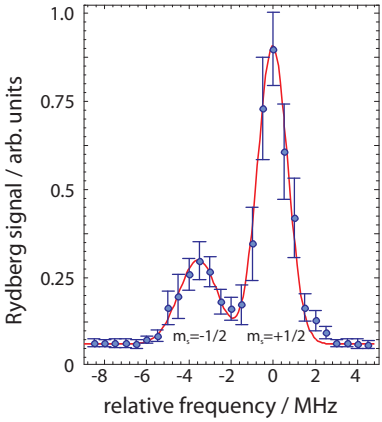

Figure 5.2 | Rydberg spectrum. Exemplary spectrum of the Rydberg excitation to the $37s$-state showing the magnetic substates.

Moreover, the magnetic field is not homogeneous due to the curvature of the magnetic trap. This slightly tilts the axis of the magnetic field depending on the distance from the center of the trap. Since the laser light propagates along the z-axis, the polarizations cannot be perfect over the entire sample. As consequences, the transitions that depend on the magnitude of the magnetic field are broadened and states with different m_j-values can be populated as well. This can be seen in the exemplary spectrum in Figure 5.2. A thorough treatment of this effect has been given earlier[88].

5.1 Two-photon laser system

All experiments in this thesis are based on the photo-excitation of Rydberg atoms or photo-association of Rydberg molecules. Thus the laser setup is at the heart of the experimental scheme. As it has been pointed out earlier, the Rydberg states are addressed via a two-photon excitation with the red laser at $\lambda_{\mathrm{red}} = 780\,\mathrm{nm}$ and the blue laser at $\lambda_{\mathrm{blue}} = 480\,\mathrm{nm}$. The blue laser light is derived from frequency doubling the light of an infrared laser running at $\lambda_{\mathrm{IR}} = 960\,\mathrm{nm}$. The laser setup is shown in Figure 5.3.

For both wavelengths, a master-slave setup is employed. The red and infrared master-lasers are external cavity diode lasers (ECDL)[a] with a typical line width of 100 kHz. The light beams of both lasers are split into several paths to monitor the frequency on a wavemeter[b] and the mode on a Fabry-Perot interferometer, to stabilize the laser frequency and to monitor the stabilization and finally a path to guide the light to the experiment.

The light of the red laser passes an acousto-optic modulator (AOM) with a central frequency of 80 MHz in double pass configuration to allow for a scanning of the laser frequency. The efficiency of the acousto-optical modulation depends on the RF-frequency. To obtain a flat intensity profile, the frequency shifted light therefore seeds a slave laser, delivering ca. 40 mW of red laser power. A second acousto-optic modulator is used to switch the beam of the slave laser on and off with a rise time of 10 ns before it is coupled into a polarization maintaining single mode fiber, delivering a well shaped Gaussian beam to the experiment.

To scan the frequency of the two-photon transition without changing the detuning from the intermediate $5p_{3/2}$-state, the light from the 960 nm-laser passes an acousto-optic modulator with a central frequency of 350 MHz in double pass configuration, allowing to scan the blue laser frequency in a range of ca. 600 MHz. The efficiency of the AOM is around 30% per pass, and thus only few mW are available afterwards. Since this is not enough for the frequency doubling, the infrared light is first seeded into a slave laser. Then it is coupled into a polarization maintaining fiber and injected into a tapered amplifier diode (TA), providing ca. 800 mW of infrared power. Finally, this light is frequency doubled in a $KNbO_3$ crystal placed in an external cavity[c], yielding ca. 300 mW at 480 nm. A second AOM switches the cw-laser with a rise time of 10 ns. Again, the light is coupled into a polarization maintaining

[a] Toptica DL pro
[b] Advantest TQ 8325
[c] Toptica SHG-TA 110

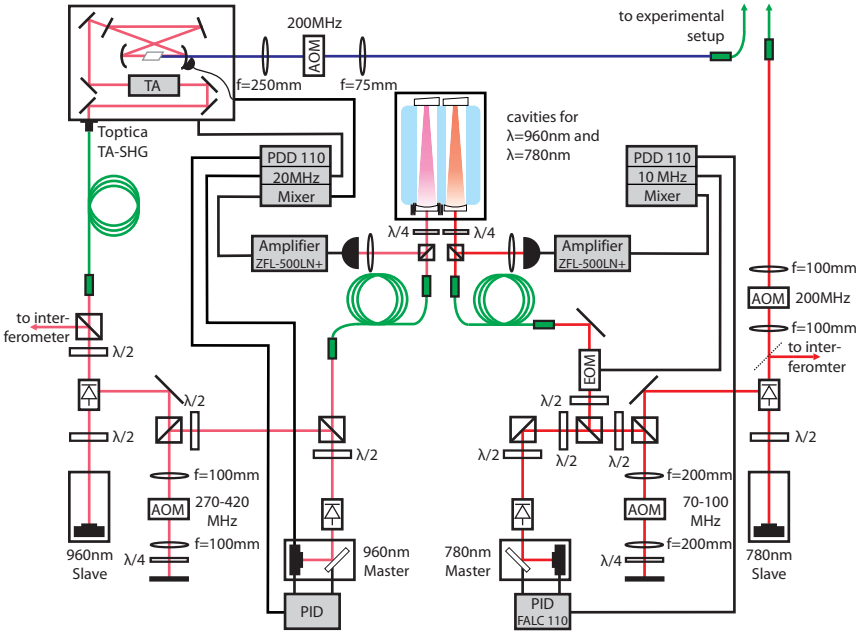

Figure 5.3 | Schematic view of the laser system.
The laser light for the Rydberg excitation is generated from diode lasers. For the 780 nm-light, a diode laser is locked to a passively stabilized cavity and frequency shifted via an acousto-optic modulator (AOM). A seeded slave laser provides a flat intensity profile when scanning the AOM.
The 480 nm light is generated from frequency doubling a diode laser at 960 nm. The master laser is locked to a cavity with a scanning piezo mirror and amplified by a slave laser diode and an tapered amplifier (TA). Light of both wavelengths is brought to the experiment via optical fibers.

single mode fiber to obtain a Gaussian profile and to improve the pointing stability at the experiment.

5.2 Frequency stabilization

The coherent control of an atomic or molecular system with lasers demands for a very good frequency stabilization since fluctuations in the frequency of lasers directly corresponds to phase fluctuations leading to a loss in coher-

ence. Apart from the laser frequency fluctuations, there are other incoherent processes. The most intrinsic loss is the limited lifetime of the atomic or molecular state, which is on the order of 30 – 100 µs for Rydberg states around $n = 40$. This translates to an intrinsic frequency uncertainty of about 10 – 30 kHz.

Another important source is the thermal motion of the atoms which results in a velocity dependent Doppler shift of the transition frequency. The Doppler effect leads to a broadening with a Gaussian lineshape. For a gas of particles with mass m at temperature T, and transition frequency at rest ν_0, the full width at half maximum (FWHM) of the Doppler broadening is[89]

$$\delta\nu = \frac{\nu_0}{c}\sqrt{\frac{8kT\ln 2}{m}}. \tag{5.1}$$

For a two-photon transition with co-propagating beams, ν_0 is the sum of the two laser frequencies. In a sample of rubidium atoms at a temperature of 3 µK this yields a Doppler width of $\delta\nu = 130$ kHz. This can be dramatically reduced by using counter propagating beams. In this case, ν_0 is the difference of the frequencies of the two lasers leading to $\delta\nu = 30$ kHz in the counter propagating case. Thus the frequency of the lasers needs to be stabilized on the order of 10 kHz.

The two master lasers have a typical frequency stability of 100 kHz and thus a further stabilization is necessary. This is realized by locking the laser frequencies to the modes of two cavities. The cavities are formed each by a plane mirror and a plano-convex mirror being glued to a 10 cm long block of ZERODUR®. The cavity for the red laser has a fixed length close to the frequency of the transition $5s_{1/2}(f = 2, m_f = 2) \rightarrow 5p_{3/2}(f = 3, m_f = 3)$. The plano-convex mirror of the cavity for the infrared laser is not glued directly to the glass-ceramic but to a piezo stack to allow to vary the length of the cavity and thus the resonance frequency. Using a special design of the piezo stack, temperature drifts are greatly reduced[90]. By applying a voltage between −150 V and 150 V from a ultra-low noise high voltage generator[d], the resonance frequency can be varied by more than one free spectral range (1.5 GHz). This allows to stabilize the frequency of the infrared laser to any desired frequency.

The most important reason for a change of the resonance frequency is a change of the length of the cavity and the change of refractive index of air in the cavity. To overcome the change of refractive index, the cavity is placed in a metal chamber that is evacuated to a pressure below 10×10^{-8} mbar using an ion

[d] Iseg T1DP 005 106 EPU

pump. Since ZERODUR® has an extremely low coefficient of thermal expansion of $\kappa = (0.05 \pm 0.10) \times 10^{-6}\,\mathrm{K}^{-1}$, the length of the cavity and thus the resonance frequencies are only weakly sensitive to temperature drifts. Furthermore, the shift of the cavity resonance frequency due to thermal expansion is very slow and thus the line width on the scale of one experimental sequence, which is on the order of few seconds, is not affected. However, it is also necessary to keep the cavity resonance frequency stable when the absolute frequency between the experiments is compared. Therefore, the vacuum vessel including the cavity is placed inside another metal box whose temperature is actively controlled on the level of some 10 mK. The remaining drift is on the order of 2 MHz/h and is owed to the increasing room temperature during the experiment is running.

To stabilize the master lasers to the cavities, the Pound-Drever-Hall (PDH) locking scheme[91] is employed. For this scheme, sidebands need to be modulated on the laser beams coupled into the cavity. The error signal generated from the different reflexion of sidebands and carrier can be fed back to the laser to keep the laser frequency on the cavity resonance. Slow frequency drifts are corrected by the angle of the grating in the laser heads via a piezo crystal, whereas fast frequency drifts are contained by a fast modulation of the diode current. The employed lasers have two BNC-connectors accepting slow and fast feedback signals.

In the case of the 780 nm-laser, sidebands at 10 MHz for the beam to the cavity are generated by an electro-optical modulator (EOM). A direct modulation of the laser current is not feasible since this would also lead to sidebands on the beam directed to the experiment. The sidebands on the 960 nm-laser at 20 MHz are generated by modulating the laser current at the same frequency. This is applicable here for two reasons: Firstly, the length of the cavity for the frequency doubling also employs a PDH-scheme and thus also needs sideband on the laser beam. Secondly, the doubling cavity acts as a bandpass filter for optical frequencies with a bandwidth of 6 MHz. The sidebands are thus filtered out and are not visible in the beam going to the experiment.

The electronic feedback loops for the frequency stabilization of both lasers are very similar and consist of a frequency generator to generate the modulation frequency and a photo-diode to monitor the light intensity that is reflected from the cavity. The signal from the photo-diode is fed into the Pound-Drever-Detector (PDD)[e], which delivers a dispersive signal with a zero-crossing at the cavity resonance. Finally, the PID-loop controls grating position and laser diode current according to the error signal. The con-

[e] Toptica PDD 110

troller to stabilize the 960 nm-laser is a homebuilt PID-loop and to control the 780 nm-laser, a commercial laser line width controller is employed[f]. Both feedback loops are found to perform equally.

When the total line width of the laser system is considered, one must not neglect the broadening effects of acousto-optic modulators. For the sake of easy control, the previous experimental setup contained frequency synthesizers that were controlled by analog voltage signals. The noise of the analog control voltage led to a line width of 50 kHz of the RF signal and directly transfers to the laser line width. With the help of digitally controlled synthesizers, the line broadening due to acousto-optic modulators is now on the order of 100 Hz[92].

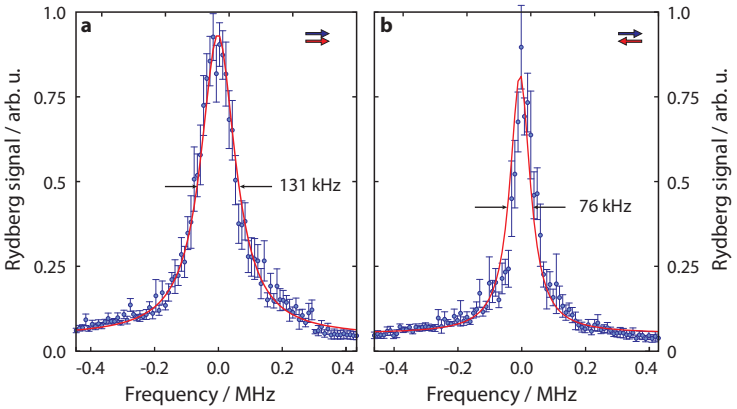

Figure 5.4 | Exemplary narrow excitation line. Comparison of the minimal achievable line width using the presented laser setup at a temperature of 3 µK. **a,** For co-propagating laser beams, the minimal line width is 131 kHz, well within the Doppler limit. **b,** For counter-propagating laser beams, the line width is 76 kHz and thus considerably lower than in the counter-propagating case.

The performance of the laser line width stabilization setup cannot be directly seen from the locking signal and thus a self-heterodyne setup has been been built[92]. The total line width for each laser found with this setup is below the detection limit of 20 kHz. Estimated conservatively, the line with of the two-photon setup thus is below 60 kHz, which is comparable to the Doppler broadening. A thorough treatment of cavity setup, locking scheme, AOM

[f] Toptica FALC

Figure 5.5 | Micro-channel plate and shielding cage. Photograph of the micro-channel plate detector (left) and the dismounted metal cage (right) that normally shields the high voltage at the MCP front side. The holder for the MCP is machined from Macor® glass ceramic.

frequency generation and self-heterodyne measurement can be found in the diploma thesis of Jonathan Balewski[92].

5.3 Detection of Rydberg atoms

Every Rydberg experiment is subdivided into a series of sequences consisting of excitation, detection and waiting. Each sequence starts with one or more laser light pulses of variable duration. The pulses are created by fast switching the radio frequency for the AOMs on and off. Directly after the excitation, the Rydberg atoms are field ionized. Therefore, the voltage at the field plates is increased from typically around 0 V to 2.5 kV in 20 ns using two special high voltage push-pull MOSFETs[g]. The resulting electric field of up to 500 V cm^{-1} field ionizes the Rydberg atom by stripping the Rydberg electron off the Rb^+-ion. The electric field inside the chamber guides the produced ions towards the detector. After a time-of-flight of ca. 2 µs, the ions reach the ion-detector.

[g] Behlke HTS 61-03-GSM

To detect the Rb^+-ion, a micro-channel plate (MCP) in chevron configuration[h] with an anode is employed. Since a voltage of −2 kV is applied to the front side of the MCP, a grounded metal cage made of a wire mesh shields the MCP and minimizes stray fields. Each ion that reaches the front side of the MCP starts a cascade of electrons that grows exponentially as it propagates through the channel. Typically, one ion produces 10^5 electrons. When the electron cascade leaves the channel it is collected by the anode. From the charge deposited on the anode, the number of incident ions can be obtained. Therefore, the anode is discharged via a resistor and the resulting current is converted to a voltage via a homebuilt transimpedance amplifier circuit[93]. The roughly 500 ns wide voltage pulses are recorded on a PCI digitizer card with 20 MHz sampling rate[i]. Compared to the previously used digitizer card, much more data can now be taken in one atomic sample. This allows to increase the spectral resolution of the spectra and to improve the statistics of the measurements.

From the area of the voltage pulse, the number of ions and thus Rydberg atom can be calculated. This is done in a collection of MATLAB® scripts that compare the height of the detected pulse with a reference pulse that is obtained from averaging over 100 calibration-pulses. Details on the calibration of the MCP can be found in ref. 92.

[h] ElMul B012VA
[i] ADLINK Technology PCI-9812

Part III

State Tomography of Rydberg Atoms and Molecules

6 Introduction to Ramsey's Method

The coherent control over atoms and molecules in an unprecedented precision is the current apogee of a long lasting development in the manipulation of atoms[94]. In the early 1920ies, coherent atomic superpositions in atomic vapors only lasted for few nano seconds[95]. It was the development of atomic beams that allowed to prepare well defined initial states and, with the help of inhomogeneous magnetic fields for a finer selection[96], pushed this coherence time to milliseconds. Another milestone was the manipulation of the internal state of atoms using radio frequency which was first demonstrated by Rabi[12]. The break-through, however, was ushered 1949 by Ramsey, who was the first to recognize that it is advantageous to have separate pulses to prepare and probe the coherent superposition of an atomic state[13]. Both, scientific and technical applications of these fundamental ideas have been mutually beneficial and have led to achievements like nuclear magnetic resonance spectroscopy for chemical analysis and noninvasive investigation of biological systems[97], atom based frequency standards for highly accurate clocks[98] and have paved the road towards quantum information technology[99].

Regarding the fruitful success that has been made possible from coherent state preparation and interrogation, this thesis aims to develop techniques to provide coherent control of Rydberg atoms as well as ultralong-range Rydberg molecules. Although the coherent control of Rydberg atoms has been demonstrated recently for two atoms[54,55], the setup presented here is suited for a coherent control of a system consisting of several million atoms which allows for the observation of collective coherent phenomena. Moreover, coherently controlling Rydberg molecules is a major step towards time resolved investigation of the dynamics of the exotic molecule and may lead to a more sophisticated understanding of the underlying binding mechanisms. The key technique to realize the coherent control of Rydberg atoms and molecules is a Ramsey-like excitation scheme. Thus its basic concepts and properties will be discussed in the following.

The crucial feature of Ramsey type experiments is the application of two equal pulses being separated in space or time and couple the internal states of the

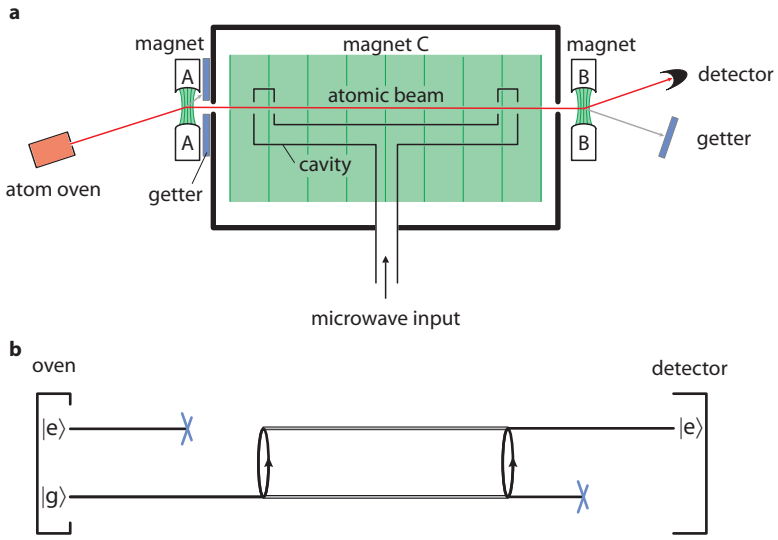

Figure 6.1 | Classical Ramsey setup scheme. a, An atomic beam is created in the oven and the Stern-Gerlach magnet A filters out atoms in the excited state. In the U-shaped Ramsey cavity, the atomic states are coupled via the oscillatory field at two separated places under the influence of magnetic field C. Finally, the beam is filtered by magnetic field B and detected. **b,** Schematic view of the evolution of the internal atomic states while an atom passes the setup.

atom. This split field technique offers several advantages over single pulse experiments:

- Resonance peaks are almost half as broad as resonance peaks from pulses with the same width in one single pulse
- The experiment is insensitive to inhomogeneities in the coupling field during the free propagation between the two pulses
- Energy levels of a system can be studied in a region where no coupling field can be applied or where it is inappropriate to apply the coupling field
- The relative phase shift between the two states can be measured and allows to precisely determine the energy difference of two levels

The schematic view of a classical Ramsey setup for an atomic beam is depicted in Figure 6.1. While magnets A and B are used to separate the path of

the atoms according to their internal state and thus prepare the initial state, the central element is the U-shaped microwave cavity. It couples the atomic beam spatially separated to the microwave field near the entrance and the exit of the experimental chamber. As becomes clear from the illustration below, a superposition between ground state $|g\rangle$ and excited state $|e\rangle$ is created in the first cavity region. In the second cavity region, the superposition is mapped back to ground and excited states. If the energy levels of ground and excited state between the coupling region are shifted with respect to the levels in the coupling region, the states will evolve differently in time and accumulate a relative phase. Then, the populations of the two states after the second interaction region will depend on the energy difference and the time the atoms spend in the intermediate region. Consequently it is possible to obtain the phase and therefore the energy difference from the population of the states after the second coupling.

When advancing the Ramsey scheme to ultra cold trapped atoms one must keep in mind that the splitting of the two coupling fields needs not to be in space, but can also be in time. Splitting the interaction regions in space is the method of choice for a continuous beam since the atoms naturally move from the first to the second region and two pulses split in time would not address the same atoms. For stationary ultra cold atoms in a trap, however, it is obvious that the Ramsey scheme is realized by two pulses of duration τ temporally separated by a delay time τ_d.

The scheme for an experimental realization is shown in Figure 6.2, along with the Ramsey fringe pattern obtained by scanning the detuning Δ of the coupling field. The relationship between duration of excitation pulse τ and delay time τ_d to the Ramsey fringe pattern is analogous to the fringe pattern from Young's double-slit experiment: The envelope is given by the width of the slit (pulse length τ), whereas the distance of the two slits (delay time τ_d) determines the oscillation frequency of the fringe pattern. For a two-level atom, the fringe pattern can be calculated as a function of the detuning Δ, e.g. based on the Bloch equations (3.9), employing the corresponding rotations for the Bloch vector given by Allen and Eberly[78]. The resulting excited state population P_e can be written in the form that has already been given by Ramsey as[100]

$$\begin{aligned} P_e(\Delta) &= 4\left(\frac{\Omega_0}{\Omega}\right)^2 \sin^2\frac{\Omega\tau}{2} \\ &\times \left(\cos\frac{\Delta\tau_d}{2}\cos\frac{\Omega\tau}{2} - \frac{\Delta}{\Omega}\sin\frac{\Delta\tau_d}{2}\sin\frac{\Omega\tau}{2}\right)^2 \end{aligned} \tag{6.1}$$

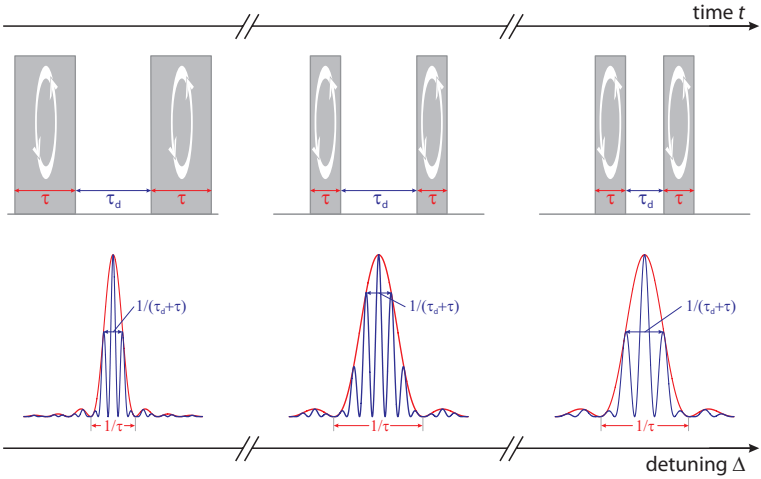

Figure 6.2 | Ramsey experiment with temporally separated pulses. The upper panel shows the realization of the Ramsey scheme in pulsed fields. When the detuning Δ of the coupling field is scanned, a fringe pattern is visible in population of the excited state (lower panel). While the envelope function (red) only depends on the length τ of the pulses, the fast modulation of the fringes is determined by the delay time τ_d between the pulses.

where Ω_o is the Rabi frequency for the coupling and $\Omega = \sqrt{\Omega_o^2 + \Delta^2}$ is the effective Rabi frequency. This corresponds to the blue curves in Figure 6.2. For the red pulse envelope function $\tilde{P}_e$, one finds

$$\tilde{P}_e(\Delta) = 4\left(\frac{\Omega_o}{\Omega}\right)^2 \sin^2 \frac{\Omega\tau}{2} \tag{6.2}$$

From (6.1) and (6.2), the analogy to Young's double slit experiment is apparent. The minima of the envelope function $\tilde{P}_e$ (6.2) are found at

$$\Delta_{\tilde{m}} = \frac{1}{\tau}\sqrt{(n\pi)^2 - (\Omega_o\tau)^2}, \tag{6.3}$$

which reduces to $\Delta_{\tilde{m}} = \pi/\tau$ for small pulse areas $\Omega_o\tau \ll \pi$. For the full Ramsey fringe pattern P_e in (6.1), finding minimal values is difficult since the

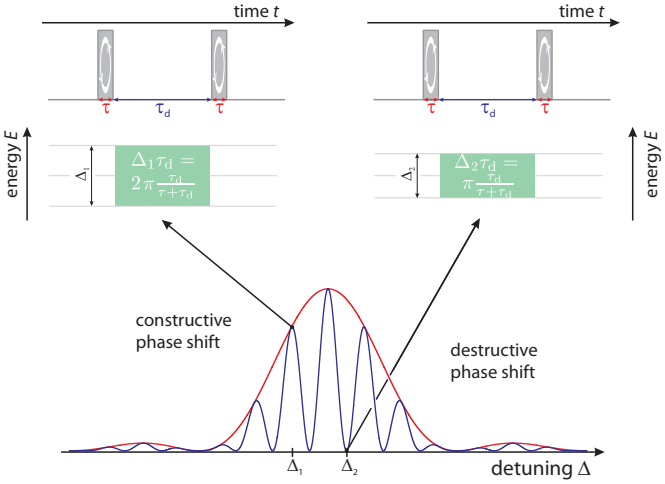

Figure 6.3 | Origin of Ramsey fringes. When the detuning Δ is scanned in a Ramsey experiment, the fringe pattern shown in the lower panel is observed. This pattern originates from the constructive or destructive interference of the relative phase between ground state $|g\rangle$ and excited state $|e\rangle$ during the delay time τ_d depending on the detuning. When the laser pulses are applied, the atomic levels are shifted due to the AC Stark shift by $\pm\Omega/2$. During the delay time τ_d, however, the levels are still shifted by $\pm\Delta/2$ and thus they accumulate the relative phase $\varphi_\Delta = \Delta\tau_d$. The accumulated phase is constructive at $\varphi_\Delta = 2n\pi\frac{\tau_d}{\tau+\tau_d}$ and the Ramsey fringe has a maximum. Accordingly, the fringe pattern has a minimum if the relative phase is destructive at $\varphi_\Delta = (2n+1)\pi\frac{\tau_d}{\tau+\tau_d}$.

transcendental equation

$$\tan\frac{\Delta_m\tau_d}{2}\tan\frac{\sqrt{\Omega_0^2+\Delta_m^2}\,\tau}{2} = \frac{\sqrt{\Omega_0^2+\Delta_m^2}}{\Delta_m} \tag{6.4}$$

must be solved. For small Rabi frequencies $\Omega_0^2/\Delta_m^2 \ll 1$, however, (6.4) can be solved analytically. Then, the minima are located at $\Delta_m = (2n+1)\pi/(\tau+\tau_d)$ and the maxima at $\Delta_m = (2n+1)\pi/(\tau+\tau_d)$.

Until now, the energy levels of ground state $|g\rangle$ and excited state $|e\rangle$ are not deliberately shifted during the delay time τ_d. Nevertheless, the occurrence of the fringe pattern in the population reveals that the two states accumulate a relative phase depending on the detuning Δ. The origin of this phase is the shift of the atomic levels due to the oscillating field. According to the

dressed atom picture, the atomic energy levels E_g and E_e are shifted apart by $\pm\Omega/2 = \pm\frac{1}{2}\sqrt{\Omega_0^2 + \Delta^2}$ due to the light shift when the coupling field is on and by $\pm\Delta/2$ when the coupling is off[101]. Thus even in the free evolution time τ_d, when the driving field Ω_0 is not present and no energy transfer occurs, the conservative shift Δ (c.f. section 3.1) of the atomic levels is relevant for the dynamics and the states $|g\rangle$ and $|e\rangle$ therefore accumulate the relative phase $\varphi_\Delta = \Delta\tau_d$. This is illustrated in Figure 6.3.

If there is another external shift of the levels $\delta E(t)$ during the delay time τ_d, an additional phase shift $\varphi_{\text{ext}} = -\int \delta E(t)/\hbar \, \mathrm{d}t$ is accumulated independent of detuning Δ. This additional phase shift has to be added to the phase φ_Δ, and consequently the zeros of the Ramsey fringe pattern are then located at $\Delta_{m,\text{ext}} = \Delta_m - \varphi_{\text{ext}}/\tau_d$, i.e. the energy shift due to the external perturbation leads to a shift of the fringe pattern that is proportional to the accumulated phase and the shift is to lower detunings if the two levels are brought closer together. This simple yet powerful relationship makes Ramsey spectroscopy an ideal candidate for the precise measurements of shifts of energy levels in ultra cold atomic samples. If the external perturbation is switched on during the delay time in an otherwise fixed Ramsey sequence, the shift of the energy levels due to the perturbation can be directly obtained from the shift of the fringe pattern in detuning Δ.

7 Coherent Creation of Ultralong-range Rydberg Molecules

Although it is a young field of research, the investigation of ultralong-range Rydberg molecules has attracted much interest due to the novelty of the exotic binding mechanism based on attractive electron-atom scattering[102,103]. Surprisingly, the photoassociation spectroscopy[4,6] of these unusual molecular states unveiled another so far undiscovered binding mechanism for ultralong-range Rydberg molecules that is based on quantum reflection. This demonstrates that the investigation of these molecules may have ready even more unexpectable findings. However, experimental methods going beyond classical spectroscopy are demanded for when the experimental interest moves on towards the investigation of the dynamical properties of ultralong-range Rydberg molecules. Therefore it is necessary to establish a coherent coupling between the unbound and the molecular state. Having at hand this crucial ingredient for the coherent preparation and probing of the molecular state, interferometric studies of the ultralong-range Rydberg molecules become possible.

As it has become clear in the previous section, Ramsey's method is a simple yet powerful approach to create and probe coherence in an atomic or molecular system. Although it is mostly described in the context of resonance of the Bloch vector of a classically moving atom, Ramsey's method can be seen as the first atom interferometer[94]. To prove the ability to coherently excite an atomic or molecular system, Ramsey's method turns out to be the method of choice because it can be easily set up experimentally and the occurrence of the fringe pattern is an unambiguous demonstration of the coherent control. Based on these ideas, this section will prove that the narrow band laser setup presented in section 5.1 can coherently drive pairs of Rubidium ground-state atoms between the unbound $5s$-$5s$ pair state and the bound ${}^3\Sigma(5s-35s)$ molecular ground state.

As depicted in Figure 7.1 **a**, the scheme for a Ramsey experiment for Rydberg molecules consist of two excitation pulses of equal length τ, separated by a delay time τ_d. The first pulse creates a superposition of the ground state and the ultralong-range molecule state whereas during the variable delay time τ_d

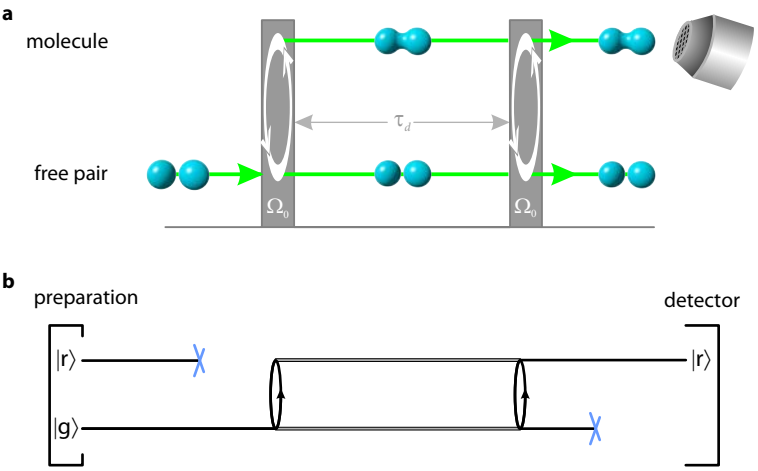

Figure 7.1 | Ramsey scheme for coherent photoassociation of molecules. **a,** The first excitation pulse creates a superposition state of bound molecules and free pairs. During the wait time τ_d, the relative phase between free pairs and molecules evolves. With the second laser pulse, the relative phase shift between the upper path and the lower path is mapped to the populations of free pairs and bound molecules and can be measured by detecting the number of Rydberg molecules. **b,** Evolution of the unbound pair state and the bound molecular state during the experiment.

the relative phase between free ground pair state and bound molecular state evolves. The second pulse of duration τ maps the relative phase back to populations of ground and molecular state. From Figure 7.1 **b**, the close relation to the classical Ramsey method with spatially separated coupling fields from Figure 6.1 **b** can be seen.

Ramsey experiments are demanding on the side of laser line width and coherence time of the observed system. On the one hand, since the two-photon Rabi frequency is limited, the duration of the excitation pulses must be long enough to create enough molecules to be detected. On the other hand, if the coherence time is too short, coherence can be lost already during the two laser pulses. Since the two-photon Rabi frequency Ω_0 in the setup is on the order of 100 kHz, a coherence time on the order of micro seconds is needed to allow for excitation pulses of adequate duration. The measurement of the laser line width as given in section 5.2 confirms that the laser setup provides the necessary frequency stability.

To implement the Ramsey method, the duration of the pulses is chosen to be $\tau = 0.75\,\mu s$. To photoassociate the ultralong-range Rydberg molecules, samples of approximately 2×10^6 ^{87}Rb atoms at a temperature of $3\,\mu K$ in the ground state $5s_{1/2}(F = 2, m_F = 2)$ are prepared. The $^3\Sigma(5s - 35s)(v = 0)$ vibrational ground state of the ultralong-range Rydberg molecules is addressed via a two-photon transition. The two lasers at 780 nm and 480 nm are detuned by $\Delta_{5p} = 380\,MHz$ from the intermediate $5p_{3/2}$-state. The red laser has a power of $96\,\mu W$ and is only slightly focused to a beam waist of $w_0 = 550\,\mu m$ at the position of the atoms. The blue laser is focused to a beam waist of $w_0 = 80\,\mu m$ and has a power of 50 mW. Taking into account the detuning of Δ_{5p}, the effective two photon Rabi frequency is $\Omega_0 = 184\,kHz$. Details on the laser setup are given in section 5.1. The number of Rydberg molecules is obtained from the MCP current after a field ionization pulse at field strength of $430\,V\,cm^{-1}$.

For each atomic sample, the delay time is kept fixed, the laser is scanned by 4 MHz across the molecular resonance and the population of the molecular state is recorded. This experiment is repeated in newly prepared samples for delay times τ_d between 0 µs and 3.2 µs. The Rydberg population as function of detuning Δ and delay time τ_d is shown in Figure 7.2 **a**. A Ramsey fringe pattern in the horizontal Δ-direction is clearly visible. The scan along the frequency axis in Figure 7.2 **c** and **d** clearly reveals the occurrence of Ramsey fringes and proves that a coherent excitation is achieved. Since each frequency scan involves 400 data points being taken in one atomic sample, the temperature slightly increases during the scan. For increasing detunings this means that the number of ground-state pairs with the right distance for photoassociation reduces, causing a reduced molecular signal. As this is an effect on the trapped ground-state atoms it does not affect the coherent evolution of the molecular state.

The Ramsey experiments can be modeled within a two-level system consisting of the unbound ground pair state $5s - 5s$ and the molecular state $^3\Sigma 35s - 5s$. The dynamics of the photoassociation are described by the optical Bloch equations (3.11)

$$\begin{aligned} \dot{u} &= -\Delta\, v - \frac{u}{T_2} \\ \dot{v} &= \Delta\, u + \Omega_0\, w - \frac{v}{T_2} \\ \dot{w} &= -\Omega_0\, v - \frac{w+1}{T_1}, \end{aligned} \tag{7.1}$$

where Δ is the detuning and Ω_0 the two-photon Rabi frequency. The time constants T_1 and T_2 are known as longitudinal and transverse relaxation times in NMR. In quantum optics, T_1 and T_2 are viewed from a different point of view. The relaxation time T_1 is here the excited state lifetime and describes the population decaying to the ground state via spontaneous emission. T_2 is the coherence lifetime and accounts for all losses of coherence, e.g. radiation loss and laser line width. Since w is the state inversion, the population of the molecular state is given by $S = \frac{w+1}{2}$.

To obtain the values for T_1 and T_2 from the measurements, the optical Bloch equations are solved numerically for the parameters Ω_0 and Δ given by the experimental Ramsey sequences. From comparing the calculated fringe patterns and the experimental data, the T_1- and T_2-times are found from an optimization procedure based on a least square algorithm that minimizes the quadratic error between experiment and model prediction. The depletion of pairs of ground-state atoms in the experiment is accounted for by an exponential decay. The optimal values obtained are $T_1 = 7.1(9)\,\mu s$ for the excited state lifetime and $T_2 = 1.3(3)\,\mu s$ for the coherence lifetime. The reproduced data from the model are depicted in Figure 7.2 **b**. The agreement to the experimental results is apparent. The scans along the Δ-axis for delay times $\tau_d = 0.7\,\mu s$ and $\tau_d = 1.7\,\mu s$ in Figure 7.2 **c** and **d** show the experimental results as blue points and the results from the calculation as red curve displayed in the conventionally used layout for Ramsey experiments. This allows for both, an easier comparison to other Ramsey type experiments and a better judgment of the excellent agreement between experiment and theory.

Aside from being a proof for the coherence of the photoassociation, the occurrence of Ramsey fringes allows to see the experiment as a realization of an atom-molecule interferometer. The relative phase shift between ground state and molecular state for given delay time τ_d and detuning Δ in Figure 7.2 **a** is given by $\delta\varphi \approx \Delta\tau_d$ in the case of no external perturbation. Maxima in the population S are expected from the theoretical analysis in chapter 6 for a phase shift of $\delta\varphi = 2\pi\frac{\tau_d}{\tau+\tau_d}$. The separation of adjacent maxima in detuning for a fixed pulse length τ and delay time τ_d then reads $(\tau+\tau_d)^{-1}$, which yields $\Delta_m = 0.69\,\text{MHz}$ and $\Delta_m = 0.40\,\text{MHz}$ for the Ramsey curves shown in Figure 7.2 **c, d**. This clear accordance to the measurements demonstrates that the relative phase shift is successfully mapped on the molecular population and an interferometer for ultralong-range Rydberg molecules has been set up.

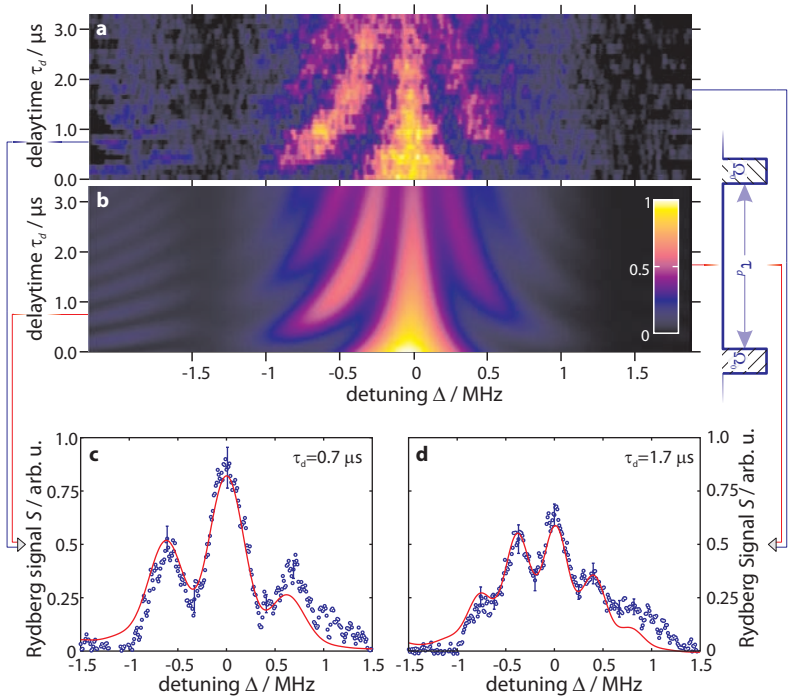

Figure 7.2 | Ramsey experiment for ultralong-range Rydberg molecules. The atomic sample is excited with two 0.75 µs long laser pulses separated by a wait time τ_d. For a wait time τ_d, the laser is scanned in one sample from $\Delta \approx -2.0$ MHz to $\Delta \approx 2.0$ MHz across the molecular resonance. This scan is repeated for wait times from $\tau_d = 0$ µs to $\tau_d = 3.3$ µs. **a,** Color-coded normalized experimental Rydberg signal. The decreasing signal from left to right is due to a slow depletion of ground-state atoms. This is accounted for in the calculation by an exponential decay. **b,** Results of the two-level model calculation with $T_1 = 7.1$ µs and $T_2 = 1.3$ µs. **c, d,** Cuts along the Δ-axis for fixed wait times of $\tau_d = 0.7$ µs and $\tau_d = 1.7$ µs with experimental (blue dots) and theoretical results (red curve). Points in **c** and **d** are averaged over eight atomic samples each and the representative error bars denote the standard deviation.

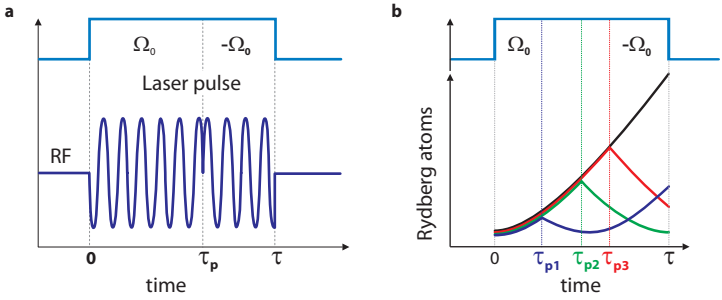

Figure 7.3 | Scheme for rotary echo experiments. a, In an excitation pulse of fixed duration τ, the phase of the driving laser light is inverted at variable time τ_p by inverting the phase of the radio frequency (RF) of an acousto optic modulator. **b,** For a perfectly coherent system, the inversion of phase at τ_p is equivalent to an inversion in the time evolution of the system. If the phase is inverted at the center of the pulse, there is no population left after the pulse.

Apart from using Ramsey's method to demonstrate the coherent photoassociation of ultralong-range Rydberg molecules, another technique known from nuclear magnetic resonance can be employed to give a second independent proof. It is well known in NMR that echo techniques make it is possible to invert the dynamics of coherent systems and to bring them back into their initial state. In the scope of the photoassociation of ultralong-range Rydberg molecules, this can be used as a test for the coherence in the excitation process. The most favorable echo scheme for this purpose is the rotary echo technique[104,105] that has previously been used to demonstrate the coherent excitation of Rydberg atoms in the 43*s*-state[106]. This echo scheme is based on the idea that shifting the phase of the exciting laser light by π is equivalent to multiplying the atom-light coupling by $e^{i\pi} = -1$, i.e. inverting the Rabi frequency Ω_o. From (3.10) it is clear that on resonance this formally corresponds to an inversion of time t for a coherent evolution.

The scheme of echo experiments for ultralong-range Rydberg molecules is depicted in Figure 7.3. In an excitation pulse of duration τ, the phase is inverted at a time τ_p during the pulse. If the phase is inverted at the center of the exciting laser pulse, $\tau_p = \tau/2$, the dynamics is unchanged for times $t < \tau/2$. After the inversion of the pulse, however, the dynamics is inverted and the excitation evolves backwards in time. If the system is fully coherent, no population is left after another time $\tau/2$ at the end of the pulse. For a phase shift at times $\tau_p \neq \tau/2$, the population is non-zero after the excitation pulse. If $\tau_p > \tau/2$, the time for the system to evolve under the inverted dynamics is too

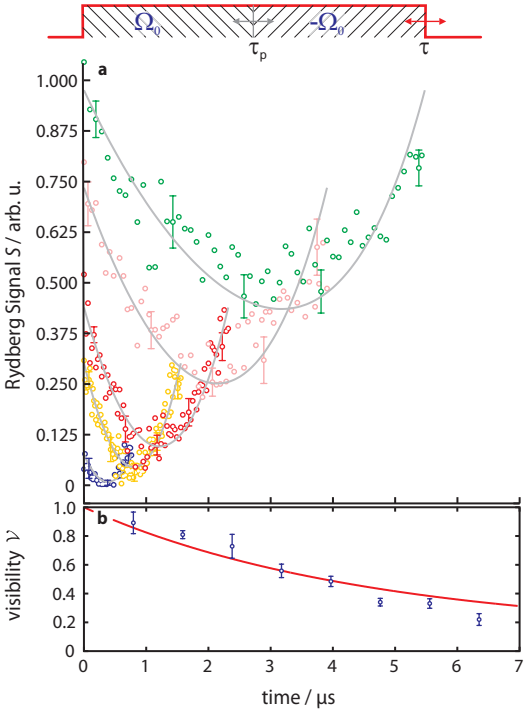

Figure 7.4 | Rotary echo experiments of ultralong-range Rydberg molecules. For a square pulse of fixed duration τ, the time of phase inversion is varied in one atomic sample from $\tau_p = 0$ to $\tau_p = \tau$. **a,** Echo curves for pulse-durations of 0.8 µs (blue), 1.6 µs (yellow), 2.4 µs (red), 4.0 µs (pink) and 5.6 µs (green). The points represent the Rydberg population S after the echo sequence where the time of phase inversion τ_p is varied from 0 to τ. The gray lines are the echo curves obtained from the calculations and an asymmetry becomes visible if the pulse duration gets comparable to the relaxation time T_1. **b,** Visibility $\mathcal{V}$ of the echo signal as a function of the duration of the excitation pulse. The red line is the result from the theoretical model. All points are averaged over five atomic samples each and the error bars represent the standard deviation.

short to return completely to the initial state. For $\tau_p < \tau/2$, the system is at its initial state already at $t = 2\tau_p$. During the remaining pulse duration $\tau - 2\tau_p$, molecules are photoassociated again.

The experimental realization is very similar to that used for Ramsey's method and only the power of the red laser was reduced to 6.5 µW, resulting in a two-

photon Rabi frequency of $\Omega_0 = 48\,\mathrm{kHz}$. To invert the Rabi frequency at time τ_p, the radio frequency of the acousto-optic modulator for switching the blue laser is inverted. For each atomic sample, the time of inversion is varied in 60 steps from $\tau_p = 0$ to $\tau_p = \tau$ and the number of Rydberg molecules created, S, is recorded. This sequence is averaged over five atomic samples. Finally, S is taken as a function of τ_p for eight different lengths of the excitation pulses τ between 0.8 µs and 6.4 µs to investigate the vanishing of the coherent character of the photoassociation.

The results of these measurements are shown in Figure 7.4 **a**. Error bars indicate the standard deviation from the five measurements per pulse duration. It is apparent that for short pulses of 0.8 µs and 1.6 µs the ultralong-range Rydberg molecules are almost completely transfered back into the unbound ground state if the phase is inverted at $\tau_p = \tau/2$, which is fully in concordance with the behavior expected for a coherent excitation. Even for long pulses of several microseconds, half of the molecules are detached again, clearly demonstrating that the coherent control of ultralong-range Rydberg molecules is feasible on the timescale of microseconds.

A measure to compare the results from different pulse lengths is the visibility $\mathcal{V}$ of the echo signal for each pulse duration that is defined by

$$\mathcal{V} = \frac{\max(S) - \min(S)}{\max(S) + \min(S)} \tag{7.2}$$

where the terms $\max(S)$ and $\min(S)$ refer to the maximal respectively minimal Rydberg signal of each measurement. Since the value of the maximal and minimal Rydberg signal is subject to experimental uncertainty, a parabola is fitted to the data first. From this parabola, the maximum and minimum values of S are obtained. Although the Rydberg signal S is not a paraboloid function of the time of phase inversion τ_p, a parabola is an appropriate approximation. The experimentally found visibility $\mathcal{V}$ for different pulse durations τ is shown in Figure 7.4 **b**. It is apparent that the visibility vanishes as the duration of the excitation pulse gets longer. This can be attributed to the limited lifetime of the coherence of the system.

To reveal this, the experimental sequence can be again modeled theoretically by the Bloch equations (7.1) and with the help of this theoretical description of the rotary echo sequence, it is possible to obtain relaxation time T_1 and coherence time T_2 from the experimental data. In section 3.2 the analytic solution of (7.1) for $\Delta = 0$ was calculated based on Torrey's method [81]. With the analytic solution at hand, a least-square algorithm can be set up to find the

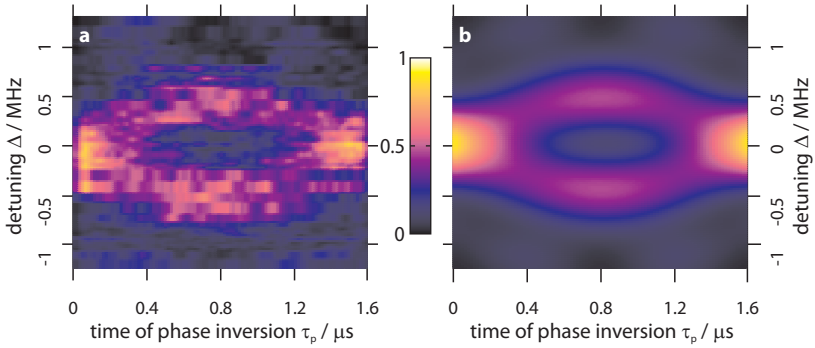

Figure 7.5 | Rotary echo experiments with variable detuning. For fixed detunings Δ from the molecular resonance, echo curves with $\tau = 1.6\,\mu s$ long excitation pulses and times of phase inversion varying from $\tau_p = 0\,\mu s$ to $\tau_p = \tau$ are taken. **a** Shows the Rydberg signal obtained in experiment and **b** the signal predicted from theory as color-coded plots normalized to the maximum Rydberg signal.

(T_1, T_2)-pair fitting best to the experimental data. The values for which the theoretically obtained curves fit best to the measurements in Figure 7.4 are a lifetime of the excited state of $T_1 = 6.4(9)\,\mu s$ and a coherence lifetime of $T_2 = 1.5(2)\,\mu s$, which agree with the values found using Ramsey's method. The theoretical curves corresponding to the best fit are shown in gray in Figure 7.4 **a** and red in Figure 7.4 **b**.

The echo experiments presented until now have been conducted with resonant excitation, while the duration of the laser pulses has been varied. This means that the coherence of the photoassociation has been observed in time domain. However, it is also possible to demonstrate the coherence of the excitation in frequency domain. Therefore, the echo experiments are carried out with a fixed pulses length of $\tau = 1.6\,\mu s$ and the time of inversion is varied in one sample from $\tau_p = 0$ to $\tau_p = \tau$. From sample to sample, the detuning to the molecular resonance is varied in steps of 50 kHz within $\Delta = \pm 1.4\,MHz$. As it has been pointed out in section 3.2, an analytic solution of the Bloch equation (7.1) is only feasible for vanishing detuning. To compare the experimental results with theoretical predictions, the Bloch equations are numerically integrated in the range of the experimental parameters. For the lifetimes T_1 and T_2, the values found from fitting the theory to the experimental data in Figure 7.4 **a** are used. The $\Delta - \tau_p$-map obtained in the experiment is shown in Figure 7.5 **a**, the corresponding result from theory in Figure 7.5 **b**. As in the previous experiment, the Rydberg population is minimal for a phase in-

version at the center of the pulse for resonant excitation and the maximal number of molecules is photoassociated when the phase is not inverted at all. For off-resonant excitation, however, the Rydberg population when exciting with a phase flip can be higher than without. This can be understood when taking into account that flipping the phase of the driving laser field can compensate the phase accumulated during the off-resonant excitation. Again, theory and experiment are in excellent agreement. It is remarkable that the experiment is well reproduced by the theory with input parameters T_1 and T_2 from the time-domain experiments. This clearly demonstrates that the model of a coherent photoassociation is valid and that the echo sequences constitute a second suitable tool to explore its properties that is independent from Ramsey's method.

With the observation of the Echo curves on the one hand and the Ramsey fringes on the other hand, the coherent creation of ultralong-range Rydberg molecules has been demonstrated. Having at hand the coherent control of the molecular system, the experimental exploration of the dynamics of these exotic molecule has become possible.

8 Lifetime of Rydberg Molecules

The lifetime of a molecule is an important property to characterize the stability of its bond and can contain information about the processes that lead to a decay of the molecule. At the first experimental observation of ultralong-range Rydberg molecules, the lifetimes of the vibrational ground states were determined [4]. Compared to the lifetime of the bare atomic Rydberg state, the values found for the molecules are considerably shorter, although the radiative decay rate is the same for atom and molecule. Also the interferometric investigation in the previous chapter confirms the short lifetime. It has been argued, that the presence of the ground-state atom inside the wave function of the Rydberg electron might make the molecule more sensitive to perturbations of the wave function [28].

The idea that the molecular potential can be deformed such that ground-state atom and Rydberg core collide is supported by the fact that an enhanced production rate of Rb_2^+ at the molecular resonances can be observed. The most probable cause for a distortion of the wave function of the Rydberg molecule is another ground-state atom passing through the orbit of the Rydberg electron. At typical densities of some $10^{13}\,\mathrm{cm}^{-3}$, trimer states with two ground-state atoms bound by the Rydberg atom can be formed and thus it is reasonable to assume that ground-state atoms are close enough to disturb the molecule. Whether the shortened lifetime is due to collisions of the molecules with ground-state atoms can be verified by measuring the lifetimes for different densities of ground-state atom. To estimate the plausibility of this idea, a theoretical consideration will be given first.

The rate at which ground-state atoms enter the orbit of the Rydberg electron can be estimated within a classical scattering theory. Therefore, one can assume that the ultralong-range Rydberg molecule dissociates when it collides with a ground-state atom. When the additional ground-state atom enters the classical volume $4/3\pi R^3$, it disturbs the Rydberg wave function and thus the molecular potential. The rate γ_{col} of such collisions in a gas is a well known problem [107]. In the case where the molecule can be treated at rest compared to the scattering ground-state atoms and the density of molecules is much

lower than the density of the ground-state atoms, the rate is given by[108]

$$\gamma_{\mathrm{col}} = \mathcal{N}\pi s^2 \overline{v}. \tag{8.1}$$

Here πs^2 is the geometric cross section, which in the case of ultralong-range Rydberg molecules is $\pi(r+R)^2 \approx \pi R^2$, since the bond length R of the molecule is much larger that the size r of the scattering ground-state atom. The mean relative velocity $\overline{v}$ of atoms with mass m in a thermal sample at temperature T is $\overline{v} = \sqrt{2 \cdot 8 k_{\mathrm{B}} T/\pi m}$[109]. Finally, $\mathcal{N}$ is the density of the scattering particles and it is reasonable to assume that the density of the scatterers is given by the density of ground-state atoms.

Applying these assumptions to (8.1), the additional decay rate of the molecular state yields

$$\gamma_{\mathrm{col}} = R^2 \sqrt{\frac{16\pi k_{\mathrm{B}} T}{m}} \mathcal{N} = \alpha_{\mathrm{col}} \mathcal{N}, \tag{8.2}$$

where the parameter α accounts for the mean velocity of the ground-state atoms and for the scattering cross section. Since the molecular states are as well subject to radiative decay as the Rydberg atom, the atomic decay rate γ_{atom} must be included as well. Then finally the decay rate of the molecular ground state reads

$$\gamma_g = \gamma_{\mathrm{atom}} + \alpha_{\mathrm{col}} \mathcal{N}. \tag{8.3}$$

To calculate the theoretical prediction of the density dependence of the molecular decay rate for the $35s$-molecular state, α_{col}, a bond length of $R = 1900 a_0$ is assumed. For ^{87}Rb and a temperature of $T = 3\mu$K, one calculates $\alpha_{\mathrm{col}} = 1.2 \times 10^{-9} \mathrm{cm}^3 \mathrm{s}^{-1}$. This means that for densities on the order of 10^{13} cm^{-3}, the collisional decay rate gets comparable to the radiative (c.f. section 1.4).

The scaling of (8.3) can be experimentally verified in a series of experiments where the lifetime of the molecular state is measured for different densities of ground-state atoms, $\mathcal{N}$. The density can be varied by pumping ground-state atoms from the $5s\ (F = 2, m_F = 2)$ state into the magnetically untrapped $5s\ (F = 1, m_F = 0)$-state via two microwave transitions at 6.834 GHz. To avoid a heating of the cloud, the frequency of the coupling microwave field must be varied across the resonance slow enough that the transition is adiabatic. According to the Landau-Zener formula[110], varying the microwave frequency within some ten ms does not leave the adiabatic regime. By changing the duration of the Landau-Zener sweep, the number of transferred atoms and

	peak density of ground-state atoms $\mathcal{N}/\mathrm{cm}^{-3}$					
	3.1×10^{12}	3.5×10^{12}	4.5×10^{12}	5.3×10^{12}	6.6×10^{12}	7.8×10^{12}
$\tau_g/\mu\mathrm{s}$	33(2)	29(2)	27.7(14)	24.1(11)	23(2)	22(2)
$\tau_e/\mu\mathrm{s}$	–	23(3)	21(3)	20(2)	19(2)	17(2)
τ_{atom}	$64(8)\,\mu$s, independent of $\mathcal{N}$					

Table 8.1 | Lifetimes of $^3\Sigma(5s-35s)$ molecules. Lifetimes of $^3\Sigma(5s-35s)$ ultralong-range Rydberg molecules in their vibrational ground state (τ_g) and an excited state (τ_e).

thus the density of ground-state atoms in the $5s$ $(F = 2, m_F = 2)$-state can be controlled[87].

To measure the depopulation rate of the Rydberg state, a delayed field ionization technique is employed. Therefore, the Rydberg molecules are first photoassociated by a laser pulse of 10 µs. Then, after a delay time τ_d, the electric field for field ionization is switched on and the Rydberg population is detected. Through varying the delay time τ_d, the population of the Rydberg state can be recorded as a function of τ_d and, from fitting an exponential curve to the depopulation, the time constant of the decay can be obtained.

Since this technique is based on the detection of the Rydberg population, it is necessary to make sure that for each delay time, the number of atoms without delay is also known. To determine this, each measurement consists of two frequency scans across the molecular resonance, where one spectrum is with delay time τ_d and the other is without delay time. Both spectra are taken simultaneously in the same atomic sample, i.e. the atoms are prepared and then for each laser frequency, two excitation-detection cycles are performed subsequently.

Measurements of the decay rate of the bare Rydberg state $35s$ at densities of ground-state atoms of $5 \times 10^{12}\mathrm{cm}^{-3}$ and $15 \times 10^{12}\mathrm{cm}^{-3}$ both yield a decay rate of the atomic state of $\gamma_{\mathrm{atom}} = 1.6(2) \times 10^4\mathrm{s}^{-1}$, depicting that the lifetime of the Rydberg state is not limited by collisions with ground-state atoms. Note that the corresponding lifetime of 64(8) µs is larger than expected from the calculated effective lifetimes including black-body induced decay given in section 1.4 and rather close to the radiative lifetime. This finding can be explained when considering that black-body induced decay from a ns state dominantly populates the $(n-1)p$ and np states. The energy of these states is close to that of the ns state and thus they can only be separated in a state-selective

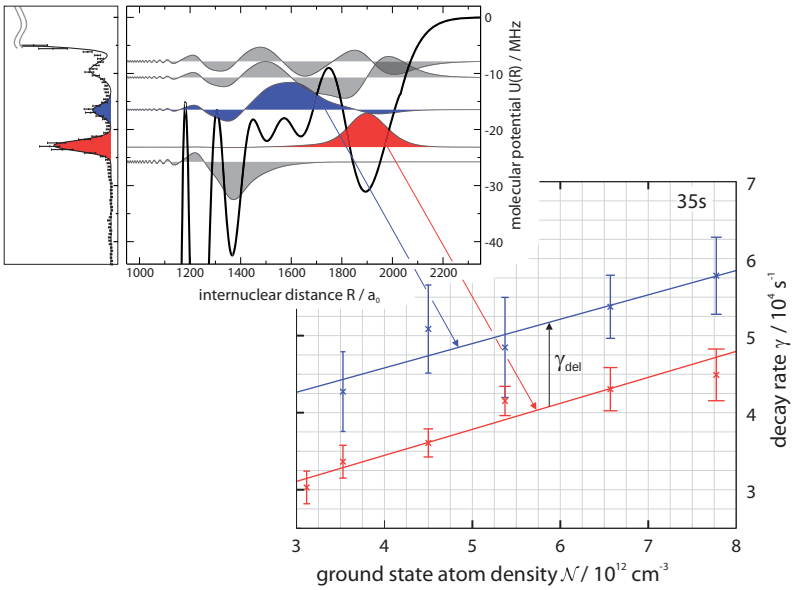

Figure 8.1 | Decay of $^3\Sigma(5s-35s)$ ultralong-range Rydberg molecules.
Decay rate of molecular ground state γ_g (red) and excited state γ_e (blue) vs. density of ground-state atoms $\mathcal{N}$. A linear fit of the type $\gamma = \gamma_o + \alpha\mathcal{N}$ yields $\gamma_{o,g} = 2.1(4) \times 10^4 s^{-1}$, $\alpha_g = 3(1) \times 10^{-9} cm^3 s^{-1}$ for the ground state and $\gamma_{o,e} = 3.3(12) \times 10^4 s^{-1}$, $\alpha_e = 3(2) \times 10^{-9} cm^3 s^{-1}$ for the excited state.
Inset: Molecular potential curve and wave functions for the 35s-state. The wave function of the vibrational ground state (red) is localized in the outermost potential well. The excited state (blue), is spread over several hundred a_o and stabilized by the quantum reflection at the potential drop near $R = 1200\, a_o$. Since the reflection is not perfect, there is a rate γ_{del} at which the excited state can reach the inner region.

field ionization procedure. Since the detection of Rydberg atoms in the experiment is not state-selective, also the population of the target states of the black-body induced decay is measured and thus the pure radiative lifetime is observed.

In Figure 8.1, the measured decay rate of the vibrational ground state, γ_g, is shown for densities of ground-state atoms between $\mathcal{N} = 3.1 \times 10^{12}$ cm^{-3} and $\mathcal{N} = 7.8 \times 10^{12}$ cm^{-3} as red crosses. It can be clearly seen that the decay rate

of the molecular states increases linearly as the density of ground-state atoms is increased. The scaling of the decay rate γ_g is well described by the red line given by $\gamma_g = \gamma_{o,g} + \alpha_g \mathcal{N}$. The scaling factor $\alpha_g = 3(1) \times 10^{-9}\mathrm{cm}^3\mathrm{s}^{-1}$ of the fit is close to the theoretical prediction α_{col} from (8.2). For the zero-density offset value, one finds $\gamma_{o,g} = 2.1(4) \times 10^4\mathrm{s}^{-1}$. Thus also the offset decay rate is close to the value expected from the model, the atomic decay rate γ_{atom}. Taking the simplicity of the model into account, the agreement between the theoretical predictions and the experimental findings is compelling.

But there is more to learn from the lifetimes shown in Figure 8.1. While the red data show the experimental findings for the vibrational ground state of the ultralong-range Rydberg molecules, the blue data show the decay rate of a vibrationally excited molecular state. The position of this state in the spectrum and its wave function in the molecular potential are depicted in the inset. It can be seen that the decay rate of this excited state is systematically higher than that of the molecular ground state, while the scaling with the density of ground-state atoms, $\mathcal{N}$, is almost identical. From fitting a linear curve of the type $\gamma_e = \gamma_{o,e} + \alpha_e \mathcal{N}$ for the excited molecular state, one finds $\alpha_e = 3(2) \times 10^{-9}\mathrm{cm}^3\mathrm{s}^{-1}$, which is in fact the same as for the molecular ground state. However, the zero-density offset value is $\gamma_{o,e} = 3.3(12) \times 10^4\mathrm{s}^{-1}$. To understand this shorter lifetime, a decay process for the excited state that does not occur for the vibrational ground state has to be considered.

As it has been pointed out in section 1.6, the excited molecular states are only bound by quantum reflection at the deep potential drop arising from the p-wave scattering resonance of the Rydberg-electron ground-state atom interaction[6]. The small probability that these states penetrate to small distances caused by the imperfect reflection ultimately leads to decay of the molecule. According to the calculation of the Wigner delay time from the derivative of the asymptotic phase shift in Table 1.5, the excited molecular state has a lifetime of only $\tau_{\mathrm{del}} = 40.5\,\mu\mathrm{s}$ until it gets into the inner region of the molecular potential.

When considering the total decay rate γ_e, the additional rate $\gamma_{\mathrm{del}} = 2.5 \times 10^4\ \mathrm{s}^{-1}$ due to this loss has to be taken into account. The overall zero-density decay rate for the excited molecular state, $\gamma_{e,o}$, expected from theory thus is $\gamma_{e,o}^{\mathrm{theo}} = \gamma_{\mathrm{atom}} + \gamma_{\mathrm{del}} = 4.1 \times 10^4\ \mathrm{s}^{-1}$, which agrees with the experimentally found value within the error bars. The agreement considering the simplicity of the theoretical model is remarkable and is another strong indication that the binding mechanism of the excited state actually is based on quantum reflection.

This experimental approach revealed that the lifetime of both, vibrational ground state and excited state of ultralong-range Rydberg molecules, depends on the density of atoms in the ground state $5s_{1/2}$. In spite of the agreement between experimental results and the approach based on classical scattering theory presented, the reduced lifetime can be explained as a distortion of the molecular state by the surrounding ground-state atoms. The dependence of this reduced lifetime on temperature T and density $\mathcal{N}$ of the ground-state atoms, $\tau_{\mathrm{col}} \propto T^{1/2}\mathcal{N}^{-1}$, clearly shows that it is only a narrow window of experimental parameters where ultralong-range Rydberg molecules can be observed: no pairs of ground-state atoms are close enough to form the molecules at densities too low, and the molecules decay too fast to be observed at all for densities being too high.

Moreover, the decay rate of the excited molecular state γ_e is systematically higher than that of the molecular ground state γ_g. By ascribing this to the inward penetration of the bound atomic pair due to imperfect quantum reflection that leads to the dissociation of the molecule, the theory of a second binding mechanism based on quantum reflection for the excited molecular states can be confirmed.

9 Rydberg Atoms in Crossed External Fields

The idea of a Ramsey setup for Rydberg molecules introduced in chapter 6 has been realized in chapter 7. There it has been given the experimental proof of the coherent photoassociation of Rydberg molecules. According to the definition given by Cronin et al.[94], the setup may even be seen as a interferometer for Rydberg molecules, although both arms of the interferometer are empty so far.

To extend the setup to a fully working interferometer, a control parameter to tune the relative phase shift between the ground-state arm and the Rydberg arm must be established. Shifting the relative energy separation of ground and Rydberg state during the delay time τ_d between the two laser pulses offers such a tunability. One advantage of working with Rydberg atoms is their exaggerated sensitivity to external electric fields that has been discussed in section 1.2 and leads e.g. to a Stark shift of the Rydberg level for the $43s$ state of 10 MHz already for electric fields $\mathcal{E}$ as low as $1\,\mathrm{V\,cm^{-1}}$. Thus a full 2π phase shift in the Rydberg-arm of the interferometer takes place even if the electric field is turned on for only 100 ns. Switching such small electric fields with nanosecond resolution is easily possible and thus applying the additional phase shift in the interferometer is straight forward.

The experimental setup for the Stark-interferometer is shown in Figure 9.1. It is very similar to the empty interferometer Figure 7.1 except for the additional electric field $\mathcal{E}$ that is turned on for the field-on time τ_{fo}. The external phase shift $\Delta\varphi_{\mathrm{Ryd}}$ due to the electric field is

$$\Delta\varphi_{\mathrm{Ryd}} = \frac{1}{\hbar}\Delta E_{\mathrm{Ryd}}\,\tau_{\mathrm{fo}} = \frac{\alpha_{43s}}{2\hbar}\tau_{\mathrm{fo}}\mathcal{E}^2, \tag{9.1}$$

taking into account the quadratic Stark shift of the $43s$-state. The polarizability of

$$\alpha_{43s} = -17.7(1)\frac{\mathrm{MHz}}{(\mathrm{V/cm})^2} \tag{9.2}$$

is extracted from calculations described in chapter 2 and is in agreement with

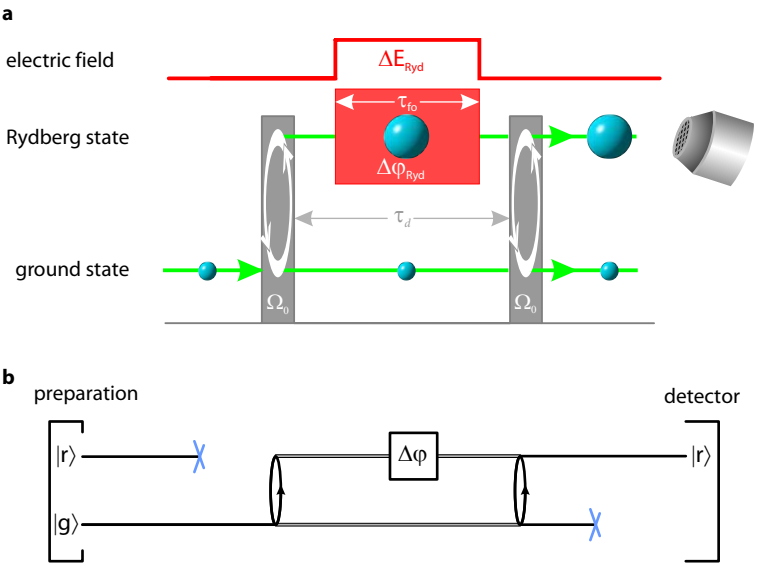

Figure 9.1 | Ramsey interferometer for Rydberg atoms with variable phase. **a,** In the first excitation pulse, a superposition ground state and Rydberg state is created. During the wait time τ_d, an external electric field $\mathcal{E}$ is applied for a field-on time τ_{fo}. This shifts the energy of the Rydberg s-state by $\Delta E_{\mathrm{Ryd}} = \frac{1}{2}\alpha\mathcal{E}^2$ and an additional relative phase $\Delta\varphi_{\mathrm{Ryd}} = \frac{1}{\hbar}\Delta E_{\mathrm{Ryd}}\tau_{\mathrm{fo}}$ between ground and Rydberg state is induced. When the relative phase shift between the ground-state arm and the Rydberg arm is mapped to the populations the two states, the level shift can be measured by detecting the number of Rydberg atoms. **b,** Schematic view of the evolution of ground state and Rydberg state during the experiment including the additional relative phase $\Delta\varphi_{\mathrm{Ryd}}$.

the empirical scaling given by O'Sullivan and Stoicheff[111]. The polarizability of the ground state is[112] $\alpha_{5s} = 0.0794(16)\,\mathrm{Hz/(V/cm)^2}$ and can thus be neglected.

To give the experimental verification of the tunable phase shift, samples of 3×10^6 ultracold rubidium atoms in the $5s_{1/2}$ ground state are prepared at a temperature of 3 µK. In each sample, Ramsey sequences of two pulses with duration $\tau = 1\,\mu\mathrm{s}$ and Rabi frequency $\Omega_0 = 120\,\mathrm{kHz}$ separated by a delay time $\tau_d = 1\,\mu\mathrm{s}$ are carried out with the detuning of both laser pulses Δ being scanned from $-2.2\,\mathrm{MHz}$ to $1.8\,\mathrm{MHz}$ in steps of 50 kHz. Additionally, a variable voltage is applied to the electric field plates in the chamber for the

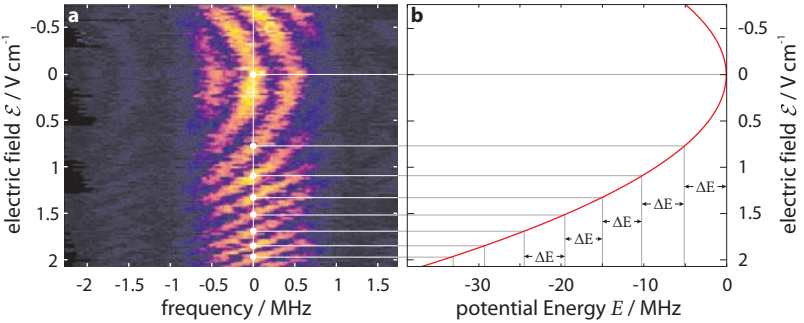

Figure 9.2 | Interferometer for $43s$ Rydberg atoms with tunable phase shift. **a,** Detected number of Rydberg atoms as function of electric field $\mathcal{E}$ and Detuning. As the electric field is tuned, the Ramsey fringe pattern is shifted to lower frequencies. From this direction of the shift, one can see that the Stark shift is negative, thus bringing the two levels closer together. The distance between the electric field values where the shift is 2π (white points) decreases linearly, since the Stark shift brings the levels closer together. **b,** Quadratic Stark shift of the $43s$ state with a polarizability of $\alpha = -17.7\,\mathrm{MHz/(V/cm)^2}$. The energies for which the phase in **a** is shifted by 2π (red points) are separated by a constant amount $\Delta E = 4.7(2)\,\mathrm{MHz}$.

field-on time $\tau_{\mathrm{fo}} = 200\,\mathrm{ns}$ during the delay time. The voltage is kept constant for each atomic sample and is varied linearly from sample to sample. Taking into account the calibration of the electric field plates[92], the electric field is varied from $-0.7\,\mathrm{V\,cm^{-1}}$ to $2.0\,\mathrm{V\,cm^{-1}}$ in 123 steps.

The results are shown in Figure 9.2. It can be seen that the Ramsey fringe pattern in Figure 9.2 **a** shifts to lower frequencies as the modulus of the applied electric field during the delay time is increased. Since the Rydberg level is shifted closer to the ground state through the Stark shift, lower detunings than without electric field generate the same phase shift and thus the fringe pattern is shifted towards lower detuning. The white points mark the electric field values $\mathcal{E}$ for which the phase differs by 2π. These points move closer together as $\mathcal{E}$ is increased. In Figure 9.2 **b** it can be seen, that the potential energies E of the Rydberg atom for these electric field values are separated by the same amount $\Delta E = 4.7(2)$ MHz each. This is exactly the expected behavior since the accumulated relative phase between ground state and Rydberg state $\Delta\varphi_{\mathrm{Ryd}} = \frac{1}{\hbar}\Delta E\tau_{\mathrm{fo}}$ is 2π for $\tau_{\mathrm{fo}} = 210\,\mathrm{ns}$, which is slightly longer than the field-on time of 200 ns measured with an oscilloscope. The small difference is mostly attributed to the impedance mismatch of the field plates in the ex-

perimental chamber and the voltage source[a] as well as the rise time of 10 ns of the voltage source[b].

In the case of a perfectly coherent system, the Ramsey fringes obtained as function of the detuning Δ are given by (6.1). Effects of finite linewidth of the exciting laser as well as limited lifetime of the population and the coherence of the atom lead to a deviation from this ideal behavior since the second Ramsey pulse is no longer perfectly coherent to all atoms.

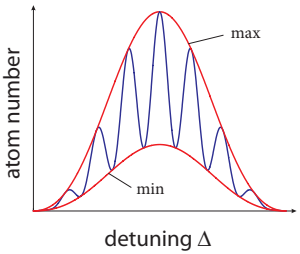

Figure 9.3 | Visibility. Definition of min and max for a visibility $\mathcal{V} = 0.5$

For the atoms that are not coupled coherently any more, the second Ramsey pulse acts independently from the first pulse and leads to an incoherent background signal that does not show Ramsey fringes. This can be accounted for by introducing the fringe contrast or visibility $\mathcal{V}$ as

$$\mathcal{V} = \frac{\max - \min}{\max + \min}, \tag{9.3}$$

where max and min represent the envelopes of the maxima and minima of the fringe pattern as depicted in Figure 9.3.

With the visibility $\mathcal{V}$ and for low Rabi frequencies $(\Omega_0/\Delta)^2 \ll 1$, the fringe pattern is given by

$$\begin{aligned} P_e(\Delta) &= 4\frac{\Omega_0^2}{\Delta^2}\sin^2\frac{\Delta\tau}{2} \\ &\times \frac{1}{1+\mathcal{V}}\left(2\mathcal{V}\cos^2\left[\frac{\tau+\tau_d}{2}\Delta + \frac{\varphi_{\text{ext}}}{2}\right] + 1 - \mathcal{V}\right). \end{aligned} \tag{9.4}$$

From fitting this function to the experimentally obtained curves, the external phase shift φ_{ext} and the visibility $\mathcal{V}$ can be extracted.

In Figure 9.4 **a**, the data from Figure 9.2 **a** is shown as function of the squared electric field, $\mathcal{E}^2$, leading to a linear behavior of the phase shift φ_{ext}. The values for visibility $\mathcal{V}$ and phase shift φ_{ext} extracted from the experimental data using (9.4) are shown in Figure 9.4 **b** and **c**. The linear scaling of the phase shift is apparent and a fit yields a slope of $2\pi \times 1.78(2)\,/(\text{V}^2/\text{cm}^2)$. Since the phase shift is given by $\varphi_{\text{ext}} = \frac{1}{2\hbar}\alpha\tau_{\text{fo}}\mathcal{E}^2$, the theoretically predicted value

[a] CGC NIM-AMX500-3
[b] EA-PS 7016-40

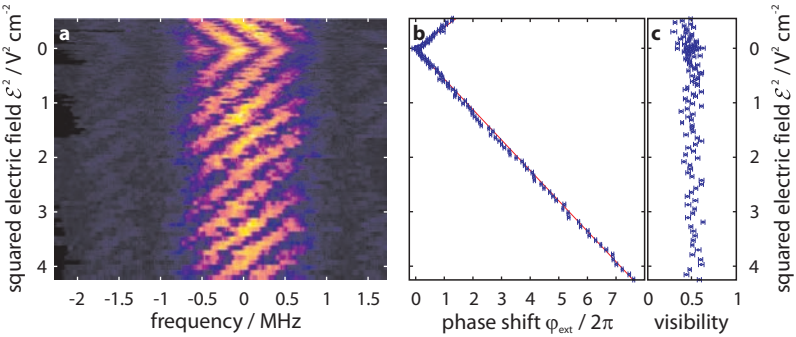

Figure 9.4 | Phase and visibility in the interferometer for $43s$ Rydberg atoms. **a,** Detected number of Rydberg atoms from figure 9.2 as function of squared electric field $\mathcal{E}^2$ and detuning Δ. The fringe pattern is linear in $\mathcal{E}^2$ since the energy shift is quadratic in the electric field. **b, c** Phase shift and visibility extracted from the experimental data from fitting the theoretical curve given by (9.4). From a linear fit of the phase shift φ_{ext} one obtains a slope of $2\pi \times 1.78(2)\,/(\text{V}^2/\text{cm}^2)$ which is in excellent agreement with the theoretical prediction of $\frac{1}{2\hbar}\alpha\tau_{\text{fo}} = 2\pi \times 1.77(1)\,/(\text{V}^2/\text{cm}^2)$. The visibility is nearly constant, showing that the electric field is stabilized enough to avoid dephasing effects. The error bars represent one standard deviation.

$\frac{1}{2\hbar}\alpha\tau_{\text{fo}} = 2\pi\times 1.77(1)\,/(\text{V}^2/\text{cm}^2)$ is in excellent agreement with the experimental value. Moreover, the visibility is almost constant for all electric fields $\mathcal{E}$. From these results it is clear that the Ramsey setup actually is an interferometer and that the relative phase between the Rydberg arm and the ground-state arm can be tuned via the exaggerated Stark shift of the Rydberg state. The quadratic scaling of the measured phase shift in the electric field, $\varphi_{\text{ext}} \propto \mathcal{E}^2$, and the almost constant visibility show that on the one hand the $43s$-state is a simple and well controllable system and that on the other hand the presented setup is well suited to explore its properties.

The measurements presented in Figure 9.2 and Figure 9.4 mark the successful application of the Ramsey interferometer and demonstrate that it can be used to explore the simple behavior of the Rydberg s-states in an external electric field. To tap the full potential of the Rydberg interferometer as a tool to explore the dynamics of quantum systems, however, more complex Rydberg states need to be considered. The next section will focus on the quest for such a system.

9.1 Rydberg states in crossed electric and weak magnetic fields

To demonstrate that the Rydberg interferometer can also be employed to investigate the dynamics of a Rydberg system, states with a non-trivial yet not too complicated energy structure are searched. The states looked at so far is the $43s\,(m_j = 1/2)$-state. Its energy structure in an external electric field $\mathcal{E}$ is depicted in Figure 9.5.

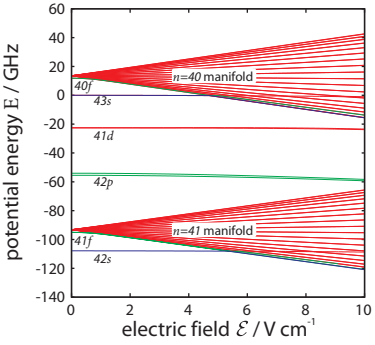

Figure 9.5 | Starkmap for Rb 43s. Starkmap in the vicinity of the $43s$ state

This state exhibits a quadratic Stark shift and it is not until a field strength of $\mathcal{E} \approx 5\,\mathrm{V\,cm^{-1}}$ that it crosses the $n = 40$ manifold, being the only level crossings until then. Exploring the dynamics at this crossing region is experimentally challenging since the required electric fields are relatively high. On the one hand, the field must be switched very fast during the delay time of the Ramsey sequence to ensure a diabatic transition of the state when the electric field is turned on and off. On the other hand, the electric field must be highly stable since the high-l states are extremely sensitive to electric fields and a noisy field can lead to a complete loss of visibility. In this context, Rydberg s-states are not a suitable model system to demonstrate the usefulness of the Rydberg interferometer in the exploration of the dynamics of Rydberg systems.

Another class of Rydberg states that can be accessed from the $5s_{1/2}$ ground state of rubidium via two-photon transitions are the d-states. Due to the orbital angular momentum of $l = 2$, these states can either have total angular momentum $j = 3/2$ or $j = 5/2$, separated by the fine structure splitting empirically found to be[113]

$$\Delta_{\mathrm{fs}} = 10\,800(15)\,\mathrm{GHz} \times \tilde{n}^{-3} - 84\,870(100)\,\mathrm{GHz} \times \tilde{n}^{-5}. \tag{9.5}$$

The structure of the $46d$-states in an electric field is depicted in Figure 9.6 **a**. In zero electric field, the $j = 3/2$-state is 4-fold, the $j = 5/2$-state 6-fold degenerate. In an external electric field, states with different absolute value of the

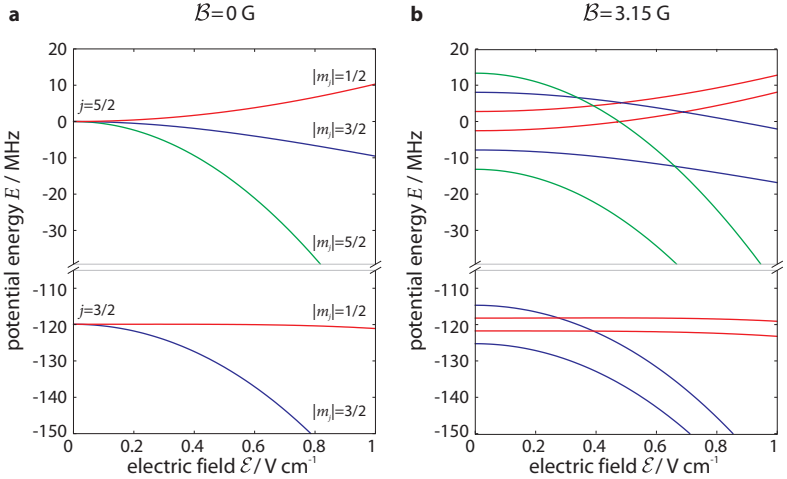

Figure 9.6 | Starkmap of the $46d$ Rydberg state for different magnetic fields pointing along the quantization axis.
a, $\mathcal{B}$ = 0 G. The fine structure splitting of the $46d$-state separates the $j = 3/2$ and $j = 5/2$ state by 120 MHz. Without magnetic field, states with the same absolute value of m_j are degenerate. States from different $|m_j|$-manifolds are not coupled. **b,** $\mathcal{B}$ = 3.15 G. The magnetic field lifts the degeneracy of the $+m_j$ and $-m_j$ levels, according to their energy shift in the magnetic field, $E_{\mathrm{mag}} = g_j m_j \mu_B \mathcal{B}$. The $m_j = 5/2$ state on the one hand has a more negative curvature in the electric field than the $m_j = 3/2$ and $m_j = 1/2$ states and on the other hand a more positive shift in the magnetic field. Thus these magnetic sublevels cross in weak electric fields but do not interact since neither the electric dipole operator $\mathfrak{d}_o$ nor the magnetic dipole operator μ couples the states.

projection of the total angular momentum j on the quantization axis, $|m_j|$, experience different Stark shifts and the states split according to $|m_j|$ into the $|m_j| = 1/2$, $|m_j| = 3/2$ and $|m_j| = 5/2$ manifolds. That the Stark shift does not depend on the sign of m_j means that parallel and anti-parallel projections are degenerate. Moreover, the electric dipole operator $\mathfrak{d}_o$ does not couple states of different m_j and thus the manifolds do not interact.

The situation changes when an addition weak magnetic field is applied parallel to the electric field. The Stark map for the case of a magnetic field with strength $\mathcal{B}$ = 3.15 G is shown in Figure 9.6 **b**. The magnetic field lifts the last remaining degeneracy of the $+m_j$ and $-m_j$ levels, since the magnetic dipole

operator also accounts for the parallel or anti-parallel orientation of the total angular momentum. Since the states with high $|m_j|$ clasp the states with lower $|m_j|$ in the Stark map, some of the magnetic sublevels cross in weak electric fields.

Although applying an electric and a magnetic field to Rydberg atoms leads to level crossings, transitions between the m_j substates cannot be driven since the states are not coupled. This is a consequence of the fact that the quantization axis can always be aligned parallel to the external fields. Therefore, the electric and magnetic dipole operators $\mathfrak{d}_0$ and μ do only couple states with the same m_j values. This situation changes dramatically when electric field $\mathcal{E}$ and magnetic field $\mathcal{B}$ are no longer parallel but draw an angle. Then, the quantization axis can only coincide with the direction of one of the fields, conveniently the magnetic field. As a consequence, the projection of the total angular momentum along the direction of the electric field and the magnetic field cannot be sharp simultaneously. Consequently, the eigenstates of the electric dipole operator need to be expressed as a sum of the different m_j states of the magnetic dipole operator. This obviously leads to a coupling of the magnetic substates.

To calculate the Starkmap in the case of crossed electric and magnetic fields, the formulas given in chapter 2 can be employed. It is convenient to place the quantization axis along the direction of the magnetic field such that the magnetic substates keep their natural meaning. If the angle between magnetic and electric field is denoted by θ, according to (2.46) the electric dipole operator can be written as

$$\mathfrak{d} = \mathfrak{d}_0 \cos\theta + \frac{1}{\sqrt{2}}(\mathfrak{d}_{-1} - \mathfrak{d}_1)\sin\theta. \tag{9.6}$$

The calculated Starkmap for the $46d_{5/2}$ levels at a magnetic field of $\mathcal{B} = 3.15\,\mathrm{G}$ and an angle $\theta = 15°$ is shown in Figure 9.7 **a**. For comparison, the Stark levels for parallel geometry $\theta = 0$ are also drawn in gray. In contrast to the previous case, the levels do not cross at the intersections but they experience avoided crossings where the m_j-character of the adiabatic energy eigenstate changes from its initial value m_j to its final value m_j' as the electric field is ramped through the intersection region.

The spectroscopic results for this case are shown in Figure 9.7 **b**. As it can bee seen, the Stark shift of the $m_j = 5/2$ state deviates from its quadratic behavior at electric fields of $\mathcal{E} \approx 0.3\,\mathrm{V\,cm^{-1}}$ and $\mathcal{E} \approx 0.4\,\mathrm{V\,cm^{-1}}$. These are the values where theory predicts the avoided crossings with the $m_j = 3/2$ and

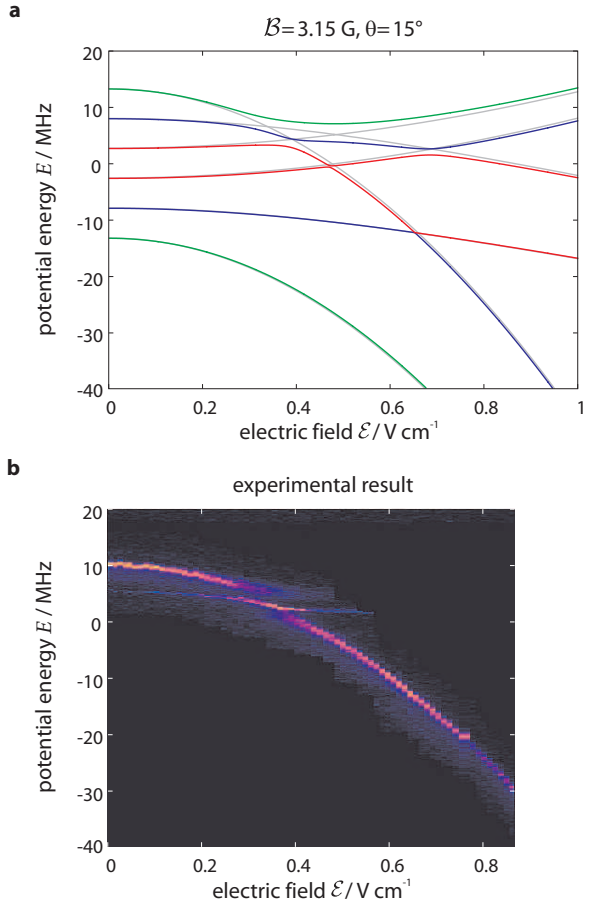

Figure 9.7 | Starkmap of the $46d$ Rydberg state in crossed electric and magnetic fields.
a, Adiabatic energy curves of the substates $m_j = \pm 5/2$ (green), $m_j = \pm 3/2$ (blue) and $m_j = \pm 1/2$ (red). States are labeled according to their zero-field behavior. In crossed external fields, the different magnetic substates are coupled and avoided crossings occur. The energy curves are calculated by diagonalizing the Zeeman-Stark Hamiltonian including all states with $l \leq 20$ in the range $40 \leq n \leq 50$ and $|m_j| \leq 9/2$. **b,** Measured Starkmap with σ^+-σ^+ polarized light, leading to a population of the $m_j = 5/2$ state. The avoided crossings are clearly visible, confirming the theoretical prediction. Around the intersection points, all involved eigenstates have $m_j = 5/2$ contribution and thus can be excited from the $5s_{1/2}$ ground state via the two-photon transition.

$m_j = 1/2$ levels to occur for an angle of $\theta = 15°$. The electric field is generated by applying a voltage to the field plates A and C while all other field plates are grounded (c.f. Figure 4.1 **b**). The resulting field is almost parallel to the magnetic field pointing along the z-axis, but due to the voltage on the grid to shield the MCP, the field direction slightly deviates from the z-axis. The deviation can also be reproduced by calculating the electric field with the SIMION® software package, although the exact value of the deviation depends on the absolute position of the trapped sample. The angle of 15° for which experimental data and theory are in excellent agreement is well within the range obtained from the calculation of the electric field.

Avoided crossings are promising properties of a system since they offer interesting dynamical effects: At the intersection point of an avoided crossing of two levels $|a\rangle$ and $|b\rangle$, the new eigenstates are given by $|+\rangle = |a\rangle + |b\rangle$ and $|-\rangle = |a\rangle - |b\rangle$, having equal contribution of the $|a\rangle$ and $|b\rangle$ eigenstates. If the system is prepared in the $|a\rangle$ eigenstate and then diabatically brought to the intersection point, it is no longer in an eigenstate but in an equal superposition of the $|+\rangle$ and $|-\rangle$ states. Due to the different eigenenergies, these two eigenstates evolve differently in time and the system will undergo Rabi oscillations between the $|a\rangle$ and the $|b\rangle$ state with the Rabi frequency given by the coupling strength. By diabatically ramping back, the coupling is removed and the Rabi oscillation is stopped. The populations of the $|a\rangle$ and $|b\rangle$ states then will depend on the interaction time and can be used to explore the dynamics of the system.

This interesting level structure in the interplay of Rydberg atoms in crossed electric and magnetic fields is easily accessible and well controllable. Its dynamics is governed by the Hamiltonian that already has been solved to obtain the Starkmap and thus can be calculated as well. The Rydberg interferometer has proven to be capable of detecting phase and energy shifts of the prepared Rydberg state. Having these ingredients at hand, the stage is prepared for the exploration of the dynamical behavior of a Rydberg system with the help of the Rydberg interferometer.

10 State Tomography of Rydberg Atoms

The previous chapter has shown that the Rydberg interferometer naturally yields two observables: phase shift φ_{ext} and visibility $\mathcal{V}$. In the experiments on the 43*s* state, the phase shift was entirely dominated by the Stark effect of the state and the visibility limited by the coherence of state preparation and readout. Since it is only these two quantities that can be obtained directly from the interferometer, it is reasonable to recall that this actually suffices to fully characterize the Rydberg state of interest.

The state of the atom can be generally expressed as

$$|z\rangle = |g\rangle + \chi\,|r\rangle + |c\rangle\,, \tag{10.1}$$

where $|g\rangle$ denotes the ground state, $|r\rangle$ the coherent part of the Rydberg state of interest and $|c\rangle$ all other Rydberg states that are not coupled coherently to $|g\rangle$. χ is the complex amplitude $\chi = a\mathrm{e}^{\mathrm{i}\varphi}$, consisting of the relative phase φ between ground state and Rydberg state and the real amplitude a, which is linked to the normalized population of the Rydberg state $|r\rangle$ via $S = a^2$.

As it has become clear in the previous chapter, the phase φ corresponds to the positions of the maxima and minima in the Ramsey fringe pattern. Thus the phase of the fringes between the perturbed interferometer and the empty interferometer is a direct measure of the relative phase shift φ_{ext} due to the perturbation. Note that the relative phase is not unique since the fringe function is 2π-periodic.

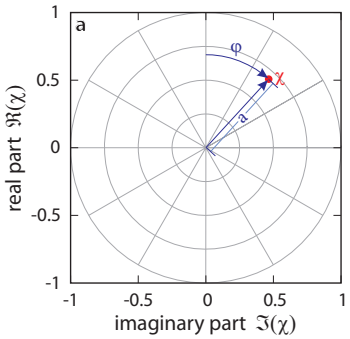

Figure 10.1 | Complex amplitude χ. Relation of χ to the phase φ and the real amplitude a

Moreover one finds that the amplitude a and the visibility $\mathcal{V}$ are connected by the relation $\mathcal{V} = a^2$. This is a consequence of the Ramsey pulses only coupling the states $|g\rangle$ and $|r\rangle$, but not $|c\rangle$. If population is transferred from $|r\rangle$ to

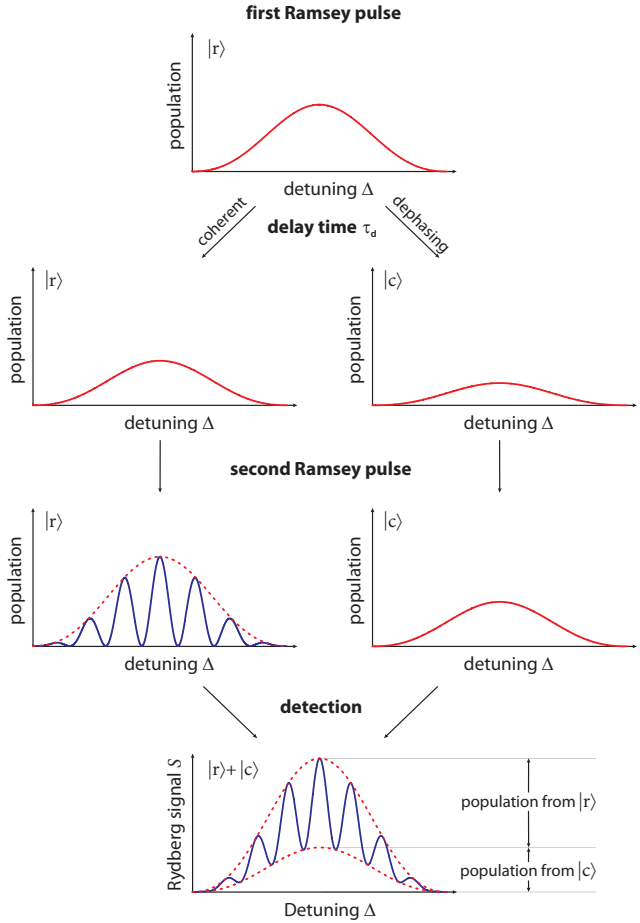

Figure 10.2 | Relation of visibility $\mathcal{V}$ to the population of states $|r\rangle$ and $|c\rangle$. The loss of visibility in the Ramsey fringes can be seen in the frame of an atomic level $|c\rangle$ that does not take part in the coherent evolution during the second Ramsey pulse. This produces an incoherent background leading to a reduced visibility of the Ramsey fringes. From the visibility $\mathcal{V}$, the population of the coherently coupled state $|r\rangle$ and all incoherent states $|c\rangle$ can be extracted.

$|c\rangle$ during the wait time τ_d due to a coupling between these states, this population will not take part in the coherent coupling during the second Ramsey pulse. If this incoherent population is detected by the MCP, it produces a background signal being the reason for the reduced visibility $\mathcal{V}$ (see Fig-

ure 10.2). For the case of the Stark shift of the $43s$-state in Figure 9.4, the loss of visibility is mostly due to dephasing of the Rydberg states $|r\rangle$, which effectively is described by transferring the incoherent population to the state $|c\rangle$ before the second Ramsey pulse. Since this loss of visibility is common to all Rydberg states, the background visibility of all shown experiments is below unity. However, this does not affect the linking between visibility $\mathcal{V}$ and amplitude a.

The avoided crossings observed in the Starkmap of the Rydberg d-states in crossed electric and magnetic fields in Figure 9.7 lead to a deviation from the quadratic scaling of the $m_j = 5/2$ state. Therefore it should also be assumed that the Ramsey fringe pattern as function of the electric field $\mathcal{E}$ during the waiting time τ_d shows a significantly different behavior than in the $43s$-case. Before the experimental results are presented, the scheme of the experiment will be illustrated and based on this, the expectations of the experiment are discussed.

The experimental sequence is depicted in Figure 10.3: Each sequence starts with all atoms in the ground state $|g\rangle$. The first Ramsey pulse transfers atoms to the $46d$ ($m_j = 5/2$) state, the Rydberg state of interest $|r\rangle$. Then, the electric field $\mathcal{E}$ is turned on fast enough that the atoms follow diabatically (gray potential curves in Figure 10.3). If the field is ramped into the region of the avoided crossings, the population is divided among the states following the adiabatic potential curves (red, green and blue). These states are coupled with the Rabi frequency Ω_c given by the splitting of the avoided crossing. During the field-on time τ_{fo}, the population thus oscillates between the different states with Rabi frequency Ω_c (c.f. upper panel of Figure 10.3). Switching off the electric field projects the states back into their diabatic components. Depending on the field-on time, the population can be completely removed from the Rydberg state $|r\rangle$. After the second Ramsey pulse, this results in a complete loss of visibility. Moreover, the phase shift φ_{ext} will no longer be given by the diabatic energy at electric field $\mathcal{E}$ alone since the Rabi oscillations between the adiabatic states introduce an additional phase shift.

To observe the fringe pattern as function of the electric field $\mathcal{E}$, samples of roughly 2×10^6 rubidium atoms in the $5s_{1/2}$ ground state are prepared at a temperature of 3 µK. In each sample, Ramsey sequences with pulse durations $\tau = 250$ ns and delay time $\tau_d = 500$ ns are conducted. The polarizations of the two-photon transition are chosen such that only the $46d_{5/2}(m_j = 5/2)$ state is addressed. The detuning Δ is scanned from −6 MHz to 6 MHz in 600 steps and the two-photon Rabi frequency is $\Omega_{\mathrm{o}} = 50$ kHz. During the delay time of the Ramsey sequence, a fixed square voltage pulse is applied for $\tau_{\mathrm{fo}} = 300$ ns

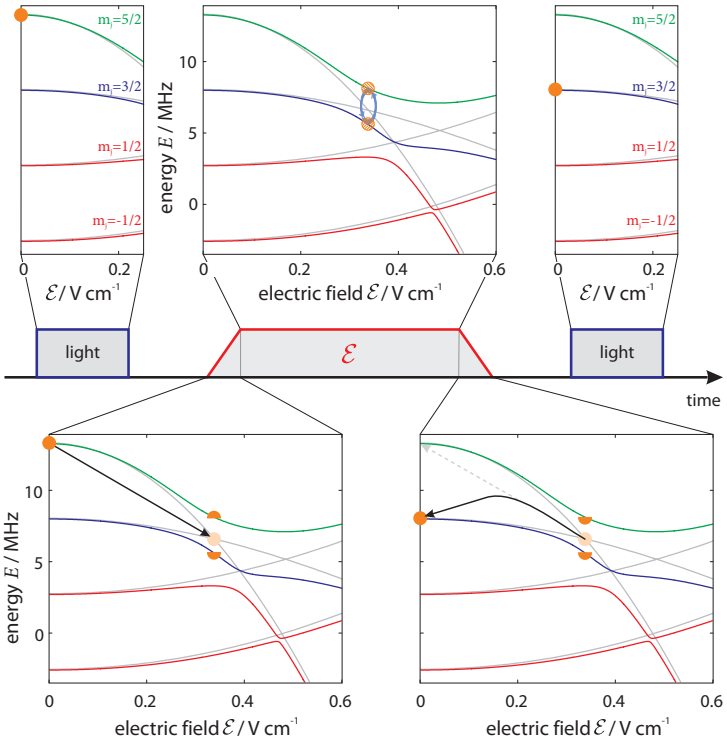

Figure 10.3 | Experimental sequence for the interferometric investigation of the $46d$ Rydberg state in crossed electric and magnetic fields.
During the first Ramsey pulse in zero electric field $\mathcal{E}$, only the $m_j = 5/2$-state is populated (orange dot). When the electric field is turned on diabatically, population is divided among the adiabatic eigenstates in the electric field (green, red, blue). Due to the avoided crossing the adiabatic eigenstates evolve differently in time. Depending on the time τ_{fo} during which the states are coupled, the population after diabatically switching off the electric field can be completely removed from the $m_j = 5/2$-state. After the second Ramsey pulse there will be no fringes, i.e. zero visibility $\mathcal{V}$.

to the field plates in the chamber by a function generator[a]. The rise time of the pulses is below 10 ns and thus the field is switched diabatically. The electric field is varied from sample to sample between 0.11 V cm^{-1} and 0.65 V cm^{-1} in 299 steps.

[a] Keithley 3390

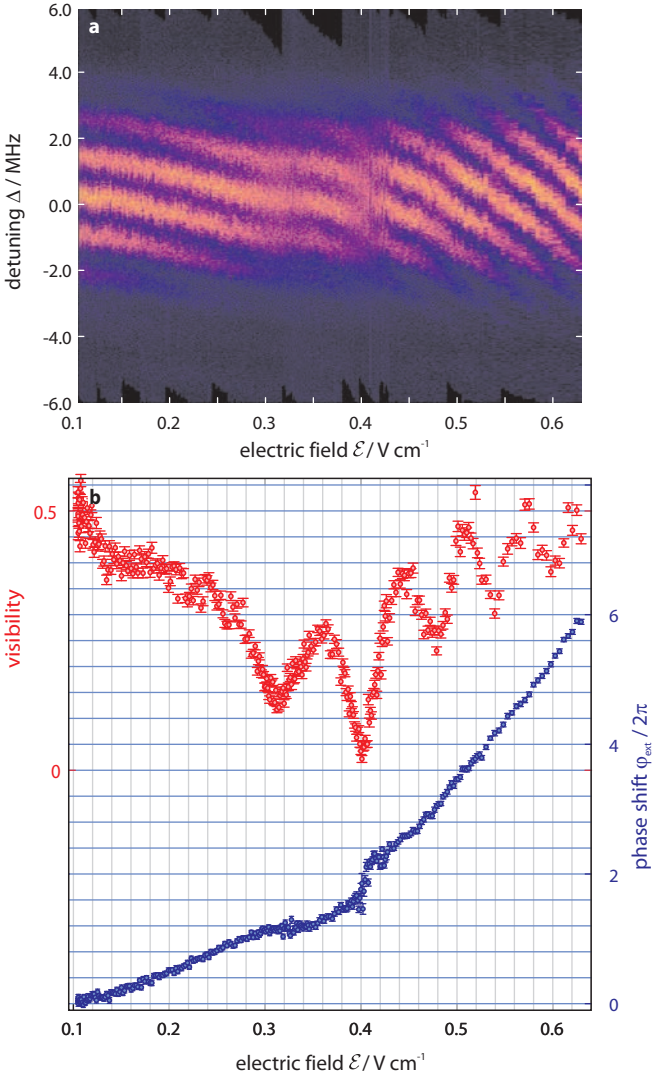

Figure 10.4 | Interferometer for the $46d$-state in variable electric field.
a, Detected number of Rydberg atoms as function of electric field $\mathcal{E}$ and detuning Δ. The fringe pattern in the region around $0.25\,\mathrm{V\,cm^{-1}} \leq \mathcal{E} \leq 0.45\,\mathrm{V\,cm^{-1}}$ is significantly distinct from the other regions and the fringes smear out. **b,** Visibility $\mathcal{V}$ and phase shift φ_{ext} as extracted from the experimental data. The visibility has several sharp minima. The phase shift has a flat plateau near $\mathcal{E} \approx 0.3\,\mathrm{V\,cm^{-1}}$ and a steep slope at $\mathcal{E} \approx 0.4\,\mathrm{V\,cm^{-1}}$

The normalized Rydberg population S at the end of the Ramsey sequence as function of the detuning Δ and the applied electric field $\mathcal{E}$ is depicted as color-coded plot in Figure 10.4 **a**. Compared to the fringe pattern of the $43s$-state in Figure 9.2 **a**, the $46d$ state shows a very different pattern. First one notes that the fringes barely shift at all for low electric fields while they show a large shift for electric fields $\mathcal{E} \geq 0.5\,\mathrm{V\,cm^{-1}}$, which is consistent with a quadratic Stark shift. However, in the region $0.25\,\mathrm{V\,cm^{-1}} \leq \mathcal{E} \leq 0.45\,\mathrm{V\,cm^{-1}}$, a very different behavior is apparent. On the one hand, the phase shift seems to slow down first and then to accelerate. Moreover the fringe pattern smears out, making it hard to define the phase of the fringe pattern at all.

To allow for a thorough analysis, the theoretical fringe pattern function from (9.4) with the fitting parameters visibility $\mathcal{V}$ and phase shift φ_{ext} is fitted to the experimental findings. The results are depicted in Figure 10.4 **b**. Again it is apparent that the visibility drops around $\mathcal{E} \approx 0.3\,\mathrm{V\,cm^{-1}}$ and $\mathcal{E} \approx 0.4\,\mathrm{V\,cm^{-1}}$, where at the same time the phase shift φ_{ext} noticeably shows a flat plateau and a steep slope.

To investigate the effects underlying this behavior, the adiabatic energy curves must be included in the considerations since they determine the dynamics of the Rydberg state at given electric fields. Therefore, Figure 10.5 again shows visibility $\mathcal{V}$ (red points) and phase shift φ_{ext} (blue points) as a function of electric field $\mathcal{E}$, now compared to the adiabatic energy levels. The axis of the adiabatic potential curve is scaled such that it coincides with the phase shift axis for a field-on time of $\tau_{\mathrm{fo}} = 300\,\mathrm{ns}$. While the blue points follow the lowest adiabatic curve with dominant $m_j = 5/2$ contribution for low electric fields $\mathcal{E} \leq 0.32\,\mathrm{V\,cm^{-1}}$, they do not coincide with any adiabatic energy level for higher electric field.

However, since the phase shift is unique only in the interval $0 \leq \varphi_{\mathrm{ext}} \leq 2\pi$, shifting the blue points by 2π is also consistent with the Ramsey fringe pattern observed in the experiment. Shifting the blue points by 2π yields the black points in Figure 10.5. It is apparent, that the black points follow the adiabatic energy curves in the region $\mathcal{E} \geq 0.32\,\mathrm{V\,cm^{-1}}$, i.e. in the region where the non-shifted data does no longer follow. This implies that the phase jumps by 2π in the region around $\mathcal{E} \approx 0.32\,\mathrm{V\,cm^{-1}}$, at the avoided crossing of the $m_j = 5/2$ and the $m_j = 3/2$ magnetic substates. Obviously, the phase jumps there from the adiabatic potential curve of the $m_j = 5/2$ state to the adiabatic curve of the $m_j = 3/2$ state. A similar effect is found near the avoided crossing of the $m_j = 5/2$ and the $m_j = 1/2$ magnetic substates around $\mathcal{E} \approx 0.4\,\mathrm{V\,cm^{-1}}$. At this electric field, the phase rises very fast by π - in contrast to the 2π jump at the first crossing.

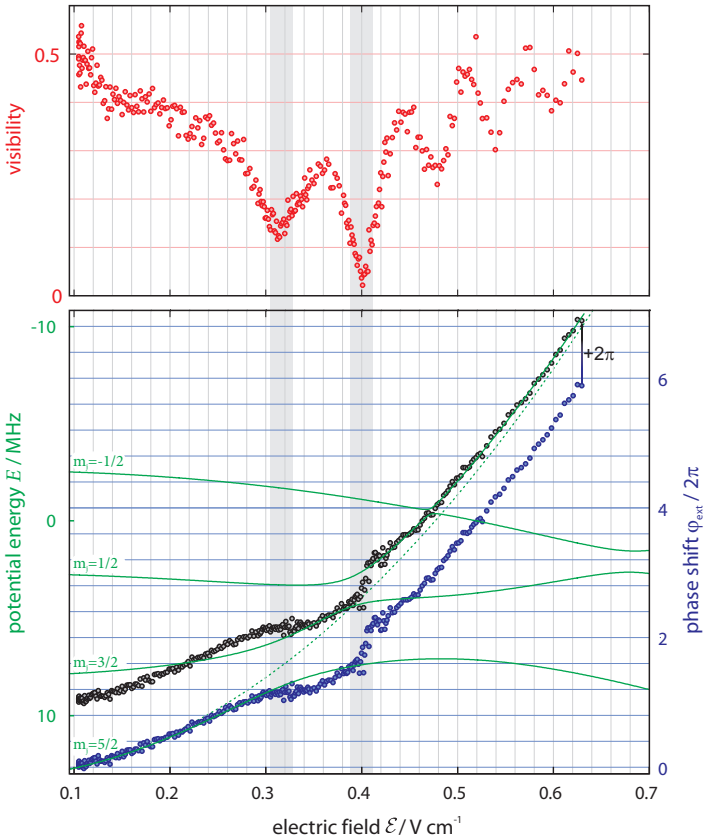

Figure 10.5 | Comparison of phase shift φ_{ext} to the adiabatic energy curves. Phase shifts as extracted from the experiment (blue points) and shifted by 2π (black points). The adiabatic potential curves (green) for the magnetic substates of the $46d_{5/2}$ Rydberg state are labeled according to their zero-field character. The dotted green curve is the diabatic potential curve for the $m_j = 5/2$ state. In the gray regions, the visibility $\mathcal{V}$ (red points) drops to nearly zero and the phase curve is abnormally flat or steep. Comparing the experimentally obtained data with theory supposes that the phase jumps by 2π near $\mathcal{E} \approx 0.3\,\mathrm{V\,cm^{-1}}$.

Note that the visibility at the 2π phase jump is higher than at the fast π phase rise. Thus the phase in the region of the lower state-crossing is continuously observed within the experimental resolution of the electric field, which is $10\,\mathrm{mV\,cm^{-1}}$, supporting the idea of a jump. However, the idea of the oc-

currence of a phase jump is by now only based on the assumption that the phase shift follows the adiabatic Stark level with dominant contribution of the $m_j = 5/2$ state in the electric field and has no experimental confirmation. Fortunately, there is a second independent way to determine the relative phase shift φ_{ext} at a given electric field $\mathcal{E}$ and field-on time τ_{fo}: increasing the field-on time from $\tau_{\text{fo}} = 0$ ns to $\tau_{\text{fo}} = 300$ ns and recording the fringe pattern.

For these measurements, the same experimental conditions as for the previous Ramsey sequences are prepared. In each atomic sample, Ramsey sequences with pulse duration $\tau = 250$ ns and delay time $\tau_d = 500$ ns are conducted and the detuning is scanned from $\Delta = -6$ MHz to $\Delta = 6$ MHz in each sample. While the amplitude of the electric field pulse is kept fixed during each experiment, the field-on time τ_{fo} is varied in steps of 10 ns from sample to sample.

Since these experiments aim to provide evidence for the existence of the 2π phase jump, the phase needs to be determined as function of the field-on time at several sgnificant electric field values $\mathcal{E}$. At first one notes that the phase shift φ_{ext} below $\mathcal{E} \approx 0.3\,\text{V cm}^{-1}$ is well described by the adiabatic potential curve and no further investigation is needed. Thus, the first scan of the field-on time is taken at a field of $\mathcal{E} = 0.31\,\text{V cm}^{-1}$ (Figure 10.6 **b**). The second scan in Figure 10.6 **c** is done at $\mathcal{E} = 0.37\,\text{V cm}^{-1}$, which is between the two regions of interesting behavior of the phase shift. At $\mathcal{E} = 0.41\,\text{V cm}^{-1}$, the third scan is taken and finally the fourth scan is far outside the region of the avoided crossings at $\mathcal{E} = 0.75\,\text{V cm}^{-1}$ (Figure 10.6 **d, e**).

In Figure 10.6 **a**, the previously obtained results for scanning the electric field for fixed field-on time is shown along with the red arrows illustrating the values of the electric field for which the phase shift has been measured as function of the field-on time. From the data in Figure 10.6 **b-e** one can obtain the value of the phase shift φ_{ext} at the field-on time $\tau_{\text{fo}} = 300$ ns at the respective values of the electric field $\mathcal{E}$. These values are depicted by the red crosses in Figure 10.6 **a**. Apparently, the measurements are in excellent agreement with the assumption of a 2π phase jump near $\mathcal{E} \approx 0.3\,\text{V cm}^{-1}$.

From the results depicted in Figure 10.6 **b-d** one can see that the visibility of the Ramsey fringe pattern shows pronounced minima for particular field-on times and an oscillatory structure in Figure 10.6 **e**. As it has been argued at the beginning of this chapter, this observation indicates a transfer of population from the $m_j = 5/2$ Rydberg state to the other magnetic substates due to the coupling in the crossed external fields and deserves a further investigation that will be given later. Moreover one finds that the phase shift φ_{ext} is rippled for the lower electric field values due to the coupling of the magnetic substates

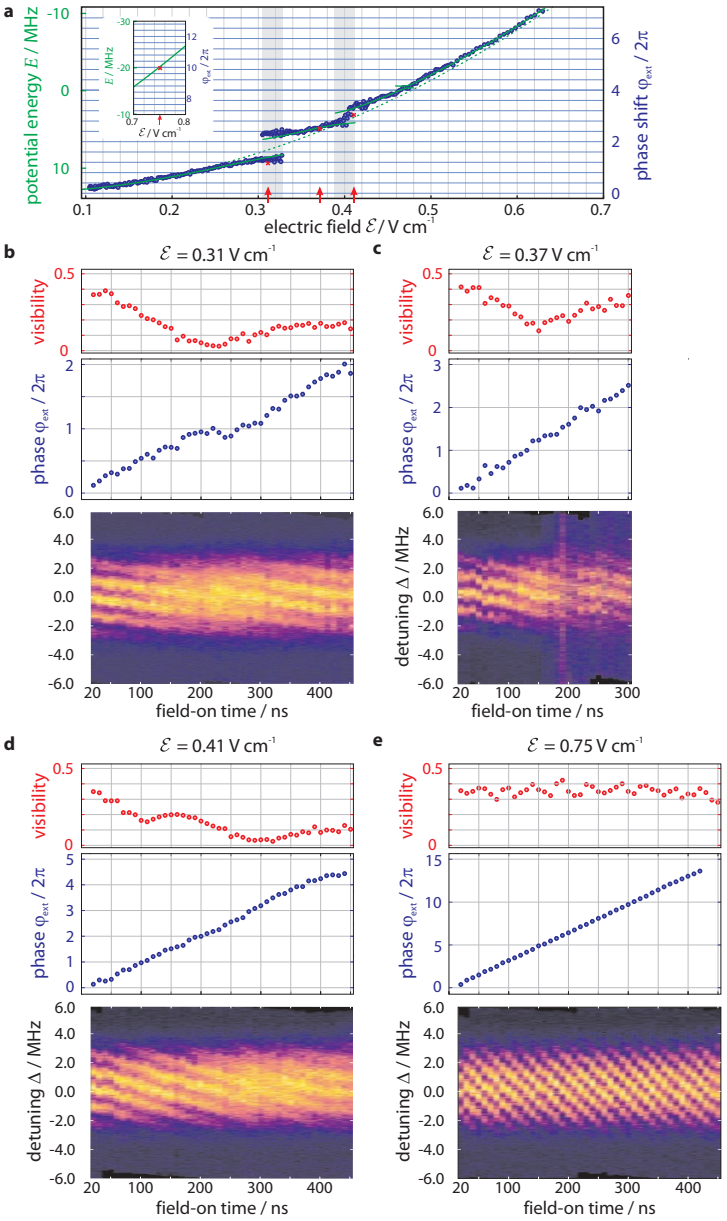

Figure 10.6 | Phase shift φ_{ext} as function of field-on time τ_{fo}.
For different fixed electric field values illustrated by the red arrows in **a**, the field-on time is varied (**b-e**). These measured phase shifts ϕ_{ext} for $\tau_{\mathrm{fo}} = 300\,\mathrm{ns}$ are depicted as red crosses in **a** and experimentally prove the 2π-phase jump around $\mathcal{E} \approx 0.3\,\mathrm{V\,cm^{-1}}$.

and shows a nearly perfect linear behavior at $\mathcal{E} = 0.75\,\mathrm{V\,cm^{-1}}$, yielding a phase shift around $14 \times 2\pi$ for a field-on time of $\tau_{\mathrm{fo}} = 420\,\mathrm{ns}$.

10.1 Theoretical modeling of the dynamics

So far, the 2π jump of the phase shift is explained by the idea that the phase shift follows the adiabatic energy curve with the largest contribution of the zero-field $m_j = 5/2$ state. The separation of the adiabatic energy curves at the avoided crossing, $2\Omega_c$, for a given field-on time τ_{fo} determines the gap of the phase shift between upper and lower adiabatic curve through the relation $\delta\varphi_{\mathrm{ext}} = 2\Omega_c\tau_{\mathrm{fo}}/\hbar$. If the field-on time is so large that the gap exceeds 2π, i.e. $\tau_{\mathrm{fo}} > \frac{\pi\hbar}{\Omega_c}$, this results in a phase jump that cannot be observed in the Rydberg interferometer. Since this phenomenon arises from the time evolution of the $m_j = 5/2$ population in the electric field $\mathcal{E}$, a theoretical investigation of the dynamics of the system may help to gain a deeper understanding of this effect and will be carried out in the following.

According to the Schrödinger equation[114], the time evolution of a state $|\psi\rangle$ of a system that is characterized by the Hamiltonian $\mathcal{H}$ is governed by

$$\mathrm{i}\hbar\frac{\mathrm{d}}{\mathrm{d}t}|\psi\rangle = \mathcal{H}|\psi\rangle\,. \tag{10.2}$$

To model the experiment, it is worth recalling the findings from the beginning of this chapter first. There it has been argued that the evolution of the complex amplitude χ of the $m_j = 5/2$ magnetic substates during the delay time τ_d determines the Ramsey fringe pattern. This greatly simplifies the theoretical treatment since only the evolution under the crossed electric and magnetic fields needs to be considered. In this case, the calculation of the dynamics employs the same states as the calculation of the Stark map: the 1870 states with $l \leq 20$ and $|m_j| \leq 9/2$ with principal quantum number n ranging from 40 to 50.

Since the $5s_{1/2}$ ground state of the atoms is insensitive to the weak electric field applied in the experiment, the ground-state part can be neglected for the calculation of the dynamics in the electric field. One then can set $\chi = 1$ after the first Ramsey pulse, meaning that the atom is in the state $|m_j = 5/2\rangle$, which is an eigenstate of the zero-electric field Hamiltonian $\mathcal{H} = \mathcal{H}_{\mathrm{o}} + \mathcal{H}_{\mathcal{B}}$. Thus χ is time-independent. In the next step, the electric field is switched on rapidly. This projects the state $|m_j = 5/2\rangle$ into a set of eigenstates $|\psi'\rangle$ of the new Hamiltonian $\mathcal{H}' = \mathcal{H}_{\mathrm{o}} + \mathcal{H}_{\mathcal{B}} + \mathcal{H}_{\mathcal{E}}(\mathcal{E})$. During the field-on time τ_{fo},

the state evolves according to its projections and their eigenenergies in the electric field $\mathcal{E}$. When the field is switched off again, the state is projected back into the zero-electric field basis. After the field pulse, the complex amplitude χ is stationary again. The second Ramsey pulse finally creates the Ramsey fringe pattern depending on χ after the electric field pulse.

From these considerations it is clear that the calculation involves three steps: First, the state is prepared in the zero-electric field value $|\psi(0)\rangle = |m_j = 5/2\rangle$ and transformed into the eigenbasis of $\mathcal{H}'$ via

$$|\psi(0)'\rangle = U^{-1}\,|\psi(0)\rangle\,, \tag{10.3}$$

where U is the matrix of eigenstates of $\mathcal{H}'$ such that $U^{-1}\mathcal{H}'U = \mathcal{D}$ is the diagonal matrix of eigenenergies. Note that the Stark map in Figure 9.7 is a graphical representation of $\mathcal{D}(\mathcal{E})$. In the second step the time evolution of the transformed state $|\psi'\rangle$ while the electric field $\mathcal{E}$ is kept at its field-on value is calculated according to (10.2) in the basis where $\mathcal{H}'$ is diagonal:

$$|\psi'(\tau_{\mathrm{fo}})\rangle = \int_0^{\tau_{\mathrm{fo}}} -\frac{\mathrm{i}}{\hbar}\mathcal{D}\,|\psi'(0)\rangle\,\mathrm{d}t. \tag{10.4}$$

Finally, the state is transformed back to the zero-electric field basis

$$|\psi(\tau_{\mathrm{fo}})\rangle = U\,|\psi'(\tau_{\mathrm{fo}})\rangle\,, \tag{10.5}$$

and the complex amplitude χ is determined as $\chi = \langle m_j = 5/2|\psi(\tau_{\mathrm{fo}})\rangle$. The time evolution can be formally integrated which then finally yields

$$|\psi(\tau_{\mathrm{fo}})\rangle = U\mathrm{e}^{-\frac{\mathrm{i}}{\hbar}\mathcal{D}\tau_{\mathrm{fo}}}U^{-1}\,|\psi(0)\rangle\,. \tag{10.6}$$

Since $\mathcal{D}$ is diagonal, the exponential $\mathrm{e}^{-\frac{\mathrm{i}}{\hbar}\mathcal{D}\tau_{\mathrm{fo}}}$ is also diagonal. Moreover, the matrix of eigenstates U needs only to be calculated once for a given electric field value which further reduces the computational effort to calculate the dynamics. Having at hand the theoretical modeling of the temporal evolution of the complex amplitude χ allows to find the effect underlying the 2π phase jump in Figure 10.4 as well as to prove that visibility $\mathcal{V}$ and phase shift φ_{ext} in the measurements in Figure 10.5 and Figure 10.6 map the complex amplitude χ of the state $|m_j = 5/2\rangle$.

The evolution of χ as function of the field-on time $\tau_{\mathrm{fo}} = 0\ldots300\,\mathrm{ns}$ for an electric field of $\mathcal{E} = 0.25\,\mathrm{V\,cm^{-1}}$ is shown as a polar plot in Figure 10.7 **a**. Thereby, the χ-vector is regarded as the tip of a vector in the complex plane and the trajectory of the tip is drawn as function of the field-on time. The red

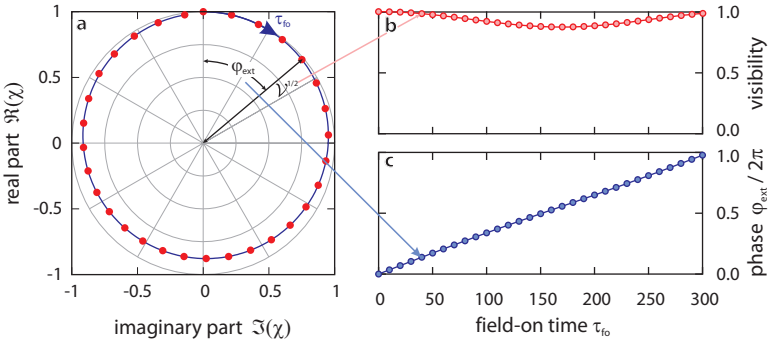

Figure 10.7 | Calculated dynamics of complex amplitude χ at $\mathcal{E}$ =0.25 V cm^{-1}. **a,** Polar plot of χ. The angle corresponds to the relative phase and the distance from the origin can be assigned to the visibility. As the field-on time τ_{fo} increases, χ describes a circle. The red points are 10 ns apart. **b,** The visibility obtained from the calculation is the modulus of χ: $\mathcal{V} = |\chi|^2$. **c,** The relative phase shift φ_{ext} is the phase of the complex number χ, i.e. $\varphi_{\mathrm{ext}} = \arg(\chi)$.

points are 10 ns apart. The chosen electric field is far off from the region of the avoided crossings so that the dynamics is simple. As the field-on time is increased, χ moves around the origin on a circle with almost constant length and angular speed, which can be seen from the equidistant spacing of the red points. Noting that the angle of χ is φ_{ext} and the length of χ is the visibility $\mathcal{V}$, these quantities can be easily extracted and are shown in Figure 10.7 **b, c**. One can see that the phase evolves linearly and the visibility is almost flat as it is expected at the given value of the electric field.

The situation changes in the regions of the avoided crossing. Figure 10.8 shows $\chi(\tau_{\mathrm{fo}})$ for the two regions of interest along with the experimental curve for phase shift φ_{ext} and visibility $\mathcal{V}$. The trajectories of χ where the phase rises fast by π around $\mathcal{E} \approx 0.4$ V cm^{-1} are depicted in Figure 10.8 **a**. At $\mathcal{E}$ = 0.402 V cm^{-1}, the slope of the phase is maximal and the visibility is minimal. It can be seen that for this electric field χ is nearly zero at τ_{fo} = 300 ns where the trajectory ends. As the electric field is only changed little from $\mathcal{E}$ = 0.398 V cm^{-1} to $\mathcal{E}$ = 0.405 V cm^{-1}, the endpoints of the trajectories only move a small distance in the complex plane. However, since the length of χ is close to zero, it moves very fast from the second to the fourth quadrant and thus also the phase changes very fast by π.

A more physical interpretation of the phase jump can also be seen from Figure 10.8 **a**. The endpoint of the trajectory of χ is at τ_{fo} = 300 ns and for

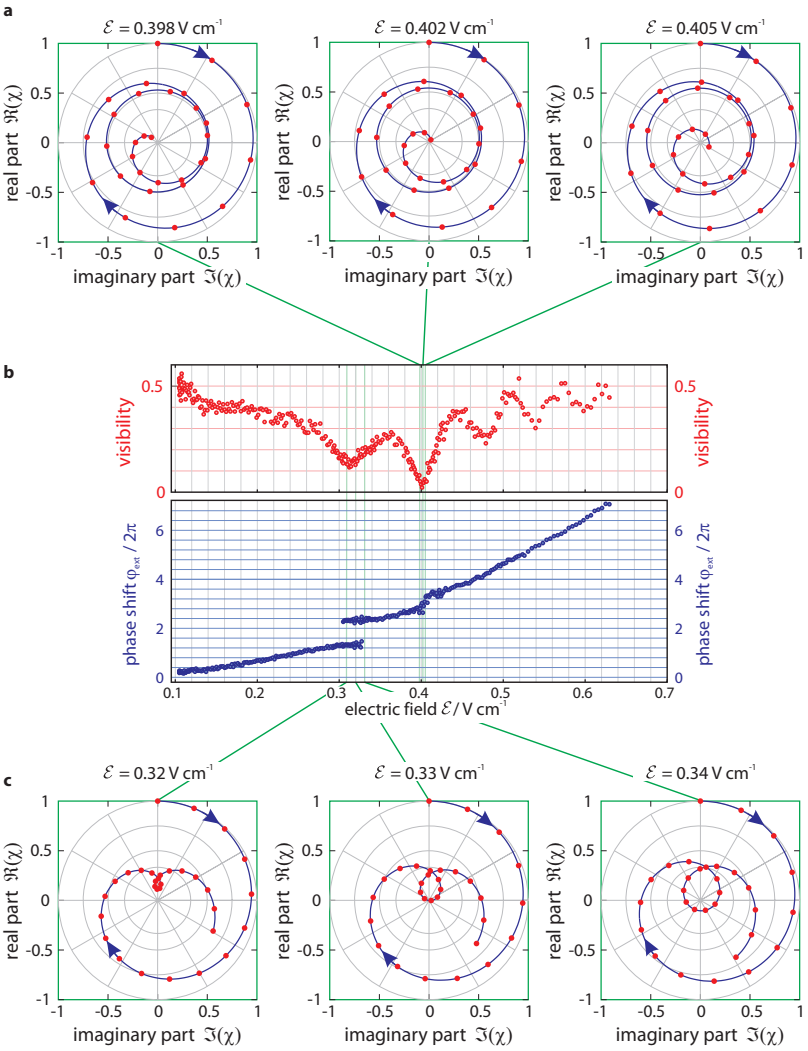

Figure 10.8 | Dynamics of χ near the avoided crossings.
the scan along the electric field for fixed field-on time τ_{fo} = 300 ns in **b,** illustrates the investigated electric fields. **a,** Polar plot of χ in the region around $\mathcal{E} \approx 0.4\,\mathrm{V\,cm^{-1}}$. When the population of the $|m_j = 5/2\rangle$ state is completely transfered to the other magnetic substates $|c\rangle$, alpha is zero and the phase changes by π. **c,** Near the electric field where the 2π phase jump occurs, the trajectory of χ in time forms an additional loop. If that loop encloses the origin, the trajectory winds another time and the phase suddenly increases by 2π. The red points are 10 ns apart.

$\mathcal{E}_c = 0.402\,\mathrm{V\,cm^{-1}}$, χ is zero at that field-on time. This means that at this electric field the coupling between the $|m_j = 5/2\rangle$-state and the other magnetic substates $|c\rangle$ is resonant, implying that the population can be completely transferred from $|m_j = 5/2\rangle$ to $|c\rangle$ for a field-on time corresponding to a $\pi/2$ pulse, which is 300 ns in this system. Consequently, one can consider the electric field region $\mathcal{E} < \mathcal{E}_c$ as red detuned and the region $\mathcal{E} > \mathcal{E}_c$ as blue detuned with respect to this coupling. That the phase accumulates a π shift when moving across a resonance is a well known phenomenon in physics and one of its most descriptive examples is the phase between a driven harmonic oscillator and the driving force that changes by π when the driving frequency is changed across the eigenfrequency of the oscillator.

A different situation is revealed around the electric field values where the phase φ_{ext} rapidly changes by 2π. Figure 10.8 **c** shows χ as function of τ_{fo} for the three values $\mathcal{E} = 0.32\,\mathrm{V\,cm^{-1}}$ just below the jump, $\mathcal{E}_c = 0.33\,\mathrm{V\,cm^{-1}}$ just at the jump and $\mathcal{E} = 0.34\,\mathrm{V\,cm^{-1}}$ right after the jump. As it can be seen in these curves, the trajectory of χ has a small additional loop for lower field values which increases as the field gets higher. Since this loop does not enclose the origin, it only causes a bump in the curve of the phase shift for lower electric fields. At $\mathcal{E} = 0.33\,\mathrm{V\,cm^{-1}}$ however, where the phase jump occurs, the aize of the loop has increased so much that it now encloses the origin, which implies that the trajectory orbits the origin once more and thus the phase shift increases by 2π. The emergence of the additional loop and its intriguing dynamics is a consequence of the complicated interaction between the magnetic substates which cannot be comprehended in a simple two-level model as it was possible for the π jump. Nevertheless these findings show that the presented calculations are an appropriate description of the Rydberg system under investigation.

Finally, the model can be used to calculate the evolution of φ_{ext} and $\mathcal{V}$ as function of the field-on time τ_{fo} for the experiments presented in Figure 10.6. The comparison of the experimental data and the theoretical calculations are shown in Figure 10.9 . The green curves are the calculated values for visibility $\mathcal{V} = |\chi|^2$ and phase shift $\varphi_{\mathrm{ext}} = \arg\chi$ whereas the red and blue points are the respective measured values. The calculated values for φ_{ext} are on the same scale as the experimental data. To account for imperfect state preparation/interrogation and dephasing processes that this theory does not account for, the calculated values of visibility $\mathcal{V}$ are scaled by 0.5, which is the background visibility of the empty interferometer. The calculated values for the visibility agree well with the experimental findings for field-on times before the state $|r\rangle$ has been totally depopulated, which is indicated by the visibility being zero. At field-on times after this depopulation, the experimental

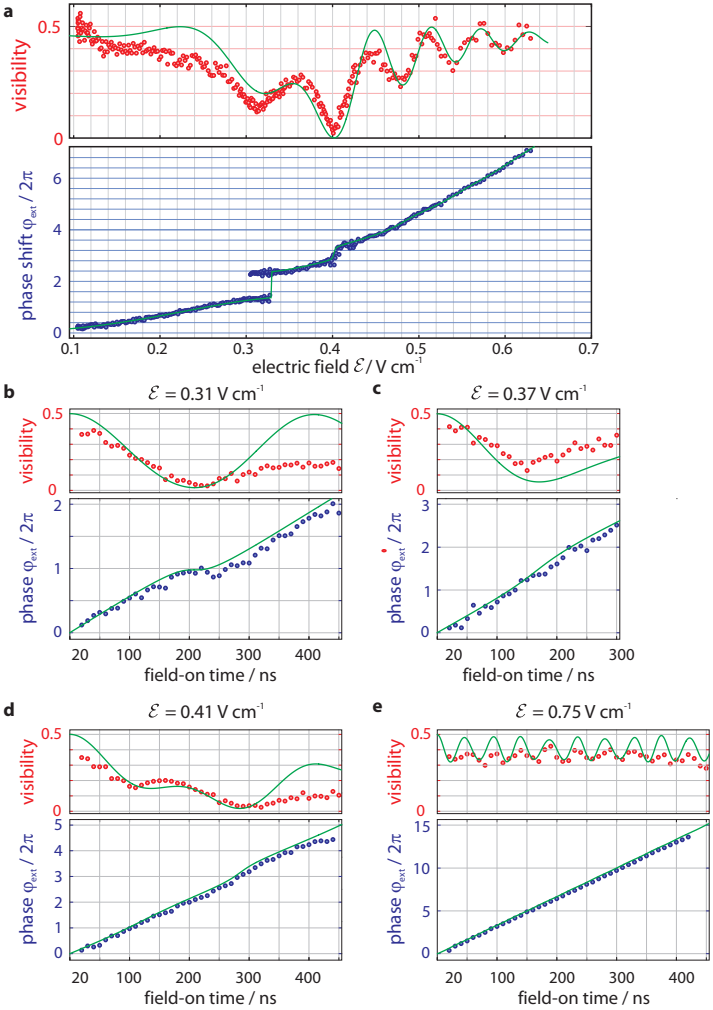

Figure 10.9 | Comparison of experimental results and theory.
a, The measured values for visibility $\mathcal{V}$ and phase shift φ_{ext} (red and blue dots) for the case of fixed field-on time τ_{fo} and scanned electric field $\mathcal{E}$ are excellently reproduced by theory (green curve). **b-e,** For the case of fixed electric field value $\mathcal{E}$ and scanned field-on time τ_{fo}, the experimentally obtained phase shifts φ_{ext} (blue points) are in good agreement with theoretical calculations. For the visibility $\mathcal{V}$, the oscillatory structure is apparent in both, theory and experiment. The theoretical curves for the visibility have been scaled by 0.5 to account for background loss of visibility due to dephasing and imperfect state preparation.

findings are lower than the expected visibility. This may be attributed to an additional dephasing of the Rydberg states $|c\rangle$ which perturbs the repopulation of $|r\rangle$.

The accordance between theory and experiment for the phase shift is apparent for all scans of field-on time τ_{fo} with fixed electric field as well as for the scan of the electric field $\mathcal{E}$ with fixed field-on time. Also for the visibility, the experimentally found behavior is largely reproduced by theory. Especially the oscillatory character of the visibility, corresponding to the oscillation of the population of the $m_j = 5/2$ state, greatly coincides between theory and experiment. The successful mapping of visibility $\mathcal{V}$ and phase shift φ_{ext} to the complex amplitude χ confirms that the Rydberg interferometer has been employed to track the dynamics of the $m_j = 5/2$ state allowing to consider it as a state tomograph for Rydberg atoms.

Conclusion and Outlook

... Aber das ist eine andere Geschichte und soll ein andermal erzählt werden.

(Michael Ende, Die unendliche Geschichte)

In the course of this thesis the techniques of coherent state preparation and interrogation introduced by Stern, Rabi, Ramsey and others have been extended to large samples of ultracold Rydberg atoms and molecules. The key technique to realize the coherent control is a Ramsey-like excitation scheme. To achieve this, a Rydberg interferometer has been set up and successfully applied in the investigation of the recently discovered ultralong-range Rydberg molecules [4] as well as for the exploration of the dynamics of atomic Rydberg states. While the coherent control of two Rydberg atoms has been demonstrated recently [54,55], the experiments presented in this thesis demonstrate the coherent control of a system consisting of several million atoms. Coherent control over large samples of Rydberg atoms is a key ingredient for collective coherent phenomena that are expected to occur for Rydberg atoms [115,116,117]. Moreover, the coherent control of Rydberg molecules has been proven. This is a major step towards time resolved investigation of the dynamics of the exotic molecule and opens new opportunities for a more sophisticated understanding of the underlying binding mechanisms.

The young field of investigation of ultralong-range Rydberg molecules has attracted much interest due to the novelty of the exotic binding mechanism based on attractive electron-atom scattering and unveiled another so far undiscovered binding mechanism for ultralong-range Rydberg molecules that is based on quantum reflection. However, experimental methods going beyond classical spectroscopy are needed for the investigation of the dynamical properties of ultralong-range Rydberg molecules. In this thesis, experimental techniques to meet these requirements have been developed. The key ingredient is the successful establishment of a coherent coupling between the unbound and the molecular state. This crucial ingredient for the coherent preparation and probing of the molecular state makes interferometric studies of the ultralong-range Rydberg molecules possible.

The first experimental application of the interferometer for ultralong-range Rydberg atoms has been presented in chapter 7. Following the work of Ramsey, an experimental sequence with two excitation pulses split in time was set up. Because the Rydberg molecules are coherently photoassociated in the experiment, the split excitation pulses create an interference pattern, known as Ramsey fringes - similar to the interference in Young's double split experiment [118]. The loss of visibility of the Ramsey fringe pattern could be de-

scribed in a simple two-level model and from these calculations, the lifetime of the molecules was determined interferometrically. Consequently, this experiment and the lifetime extracted thereby is the first interferometric study of ultralong-range Rydberg molecules. Thus aside from being an elegant and unambiguous proof for the coherence of the photoassociation, the occurrence of Ramsey fringes also allows one to see the experiment as an atom-molecule interferometer.

Apart from Ramsey's method, the rotary echo technique known from nuclear magnetic resonance[104,105] has be employed to give a second independent proof for the the coherent photoassociation of ultralong-range Rydberg molecules. It has been shown that this technique makes it possible to invert the dynamics of the photoassociation of ultralong-range Rydberg molecules. For short excitation pulses, almost all Rydberg molecules could be transferred back into the unbound state when the dynamics is inverted in the center of the pulse. Also in this experiment, the vanishing of coherence was explained by the two-level model, yielding the same results as the interferometric approach. The accordance of the results obtained from the two different experiments also shows that the coherent character is maintained in the variable experimental setups presented. With the coherent control of the molecular system at hand now, these experiments have paved the way towards experimental exploration of the dynamics of these exotic molecule.

An approach to explore these dynamics may be based on the coupling of the vibrational levels. While the rovibrational transitions in most molecules are in the range of near infrared radiation, the vibrational levels of the ultralong-range Rydberg molecules are only separated by some MHz and thus transitions can be driven via radio frequency pulses. To drive these transitions with electromagnetic radiation however, the molecules also need to have a dipole moment. While huge dipole moments are expected for the high-l trilobite molecules[3], it has been found recently, that also the s-state molecules have a permanent dipole moment on the order of 1 Debye[119].

With the prerequisites for coupling the vibrational levels fulfilled, one can now think about possible schemes to explore more of the properties of ultralong-range Rydberg molecules. One possible experimental route is depicted in Figure C.1. In an atomic sample of appropriate density and temperature prepared, the first Ramsey pulse is applied on resonance to one of the molecular states v. At the beginning of the delay time, a RF-pulse is applied to couple the populated state v to another vibrational state v'. The resulting state is a superposition of the two vibrational states and the relative contributions

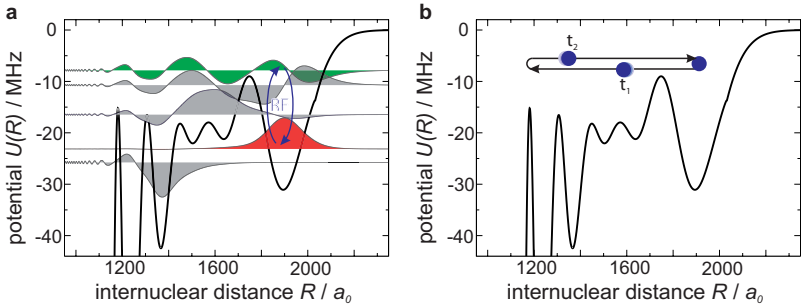

Figure C.1 | Moving wave packet in the molecular potential.
a After preparing the atom pair in a superposition between the free pair state and the molecule in its vibrational ground state with the first Ramsey pulse, a radio frequency pulse (RF) is applied. This creates a superposition between the vibrational ground state and the excited state. **b** The molecular state can be seen as a wave packet that is moving in the molecular potential. Depending on the timing of the second Ramsey pulse, the position of the wave packet can be reconstructed after different propagation times t_1, t_2 from the phase in the Ramsey fringe pattern.

can be controlled with the coupling strength of the RF-pulse. Since the resulting state is not an eigenstate any more, it is no longer stationary and a moving wave packet has been created. Moreover, the properties of the wave packet can be tuned by selecting appropriate vibrational states and RF coupling strength.

With the wave packet created, it may become possible to track its motion in the molecular potential while the radio frequency is turned off. Especially the quantum refection at the deep abyss due to the p-wave shape resonance may be observed. At this point, the Rydberg interferometer comes into play. The classical detection scheme based on field ionization only yields the number of Rydberg atoms and thus no conclusions about the wave packet can be drawn from an absorptive measurement. With the Rydberg interferometer, however, it is possible to measure the projection of the wave packet onto all the different vibrational states. Particularly interesting hereby is that also the phase information can be obtained since the wave packet can only be reconstructed with information about both phase and relative populations.

Tracking the motion of the wave packet in the molecular potential then may be realized as follows. In the first Ramsey pulse, a superposition between free pair state and molecular ground state is created. Then, a short RF pulse is

applied to form the wave packet. After a tunable evolution time, the second Ramsey pulse interrogates phase and population of the addressed state. Note that it is possible to address the different vibrational states with the second Ramsey pulse when the detuning is chosen accordingly. Observing the motion of wave packets in the molecular potential would yield another proof for the quantum reflection and may reveal even more unexpected properties of ultralong-range Rydberg molecules.

For another open question in the field of ultralong-range Rydberg molecules - their lifetime - the findings in this thesis brought clarity. Although previous experimental observation of ultralong-range Rydberg molecules[4] as well as the interferometric investigations in this thesis both yield that the lifetime of the molecules is shorter than the lifetime of the atomic Rydberg state, the reason for these findings was unclear. The experimental observations in chapter 8 revealed that the lifetime of the vibrational ground state of the Rydberg molecules depends on the density of atoms in the ground state $5s_{1/2}$. An approach based on classical scattering theory can explain the reduced lifetime under the assumption that the molecular state is distorted by the surrounding ground-state atoms. The limited lifetime thus could be attributed to collisions of the molecules with the surrounding ground-state atoms[7].

Moreover, the measurements of the lifetime of ultralong-range Rydberg molecules have brought more insight into the emergence of another binding mechanisms for the molecules. From the density-dependent investigations it could be found that the lifetime of the vibrationally excited molecular state is systematically shorter than that of the molecular ground state. These findings confirm the theory that the excited molecular states are bound by a different binding mechanism based on quantum reflection: The shortened lifetime can be ascribed to the inward penetration of the bound atomic pair due to imperfect quantum reflection that leads to the dissociation of the molecule. The theoretically expected Wigner delay time until the transmission occurs that is calculated from the molecular potential curve has been validated by the reduction of the lifetime found in the experiment.

In total, the dependence of the lifetime of the ultralong-range Rydberg molecules on temperature T and density $\mathcal{N}$ of the ground-state atoms is found to be $\tau_{\mathrm{col}} \propto T^{1/2}\mathcal{N}^{-1}$. This shows that it is only a narrow window of experimental parameters where ultralong-range Rydberg molecules can be observed at all since for too low densities no pairs of ground-state atoms are close enough to be photoassociated, and the molecules decay too fast to be observed if the density is too high. The presented experimental setup with its high densities

and its ability for coherent excitation can operate in this window of possibilities and may be the basis for more sophisticated experiments revealing more unexpected properties of these peculiar molecular states.

In the further course of this thesis, the idea of a Ramsey setup for Rydberg molecules has been extend to Rydberg atoms. With the introduction of a control parameter to tune the relative phase shift between the ground-state arm and the Rydberg arm, the so far empty interferometer has been extended to a full working interferometer. To shift the relative phase of the two arms during the delay time between the two laser pulses, the exaggerated sensitivity of Rydberg atoms to external electric fields is utilized.

These measurements have verified that the energy shift due to the external perturbation leads to a shift of the fringe pattern that is proportional to the accumulated phase and they show that the Stark shift of the $43s$ Rydberg state can be successfully mapped on the Ramsey fringe pattern obtained from the interferometer. Although -or maybe just because - this relationship is so simple, it makes Ramsey spectroscopy an ideal candidate for the precise measurements of shifts of energy levels in ultra cold atomic samples since the energy shift during the delay time can be directly obtained from the shift of the fringe pattern as the detuning Δ is scanned.

While the measurements on the $43s$-state with its quadratic scaling of the phase shift in the electric field demonstrated the usability of the interferometer in a simple and well controllable system and can be seen as a proof-of-principle experiment, the interferometric studies on the $46d$-state in crossed external fields can be regarded as the first investigative application of the interferometer. The interesting level structure in the interplay of Rydberg atoms in crossed electric and magnetic fields is easily accessible and experimentally well controllable. Its dynamics, however, is not as simple as in the $43s$-case. Applying a magnetic as well as an electric field leads to a complete lifting of the degeneracy of the magnetic structure of the atom. More importantly, couplings within the magnetic substructure emerge if the fields draw an angle and at the electric fields where the magnetic sublevels cross in the parallel field configuration, avoided crossings occur for the adiabatic energy levels in the crossed geometry. With the help of the Rydberg interferometer, the behavior of Rydberg atoms under these condition could be explored in this thesis.

The key point of the investigation is the link between the two observables of the Rydberg interferometer, phase shift φ_{ext} and visibility $\mathcal{V}$, and the complex value χ describing the Rydberg state of interest. It was found that the phase shift of the Rydberg state mostly follows the adiabatic energy curves

in the electric field calculated for these experimental parameters. However, in the region where the avoided crossings occur, the phase shift behaves substantially different. While the phase rises fast by π near the avoided crossing of the $m_j = 5/2$ and the $m_j = 1/2$ states, a 2π jump occurs at the avoided crossing of the $m_j = 5/2$ and the $m_j = 3/2$ states. Since the phase can only be determined in the interval between 0 and 2π experimentally, the jump cannot be observed as function of the electric field. This limitation has been overcome by taking the phase shift as function of time for different electric fields, which allows to reconstruct the phase at the given field-on time independently. From these measurements, the occurrence of the 2π jump could be validated.

To explore the reasons underlying the behavior of the phase in the electric field, the dynamics of the system has been modeled theoretically. The experimental findings for the phase shift as well as for the visibility are thoroughly reproduced by theory. Especially the characteristic behavior of phase shift and visibility near the avoided crossings is also seen in the calculations. With the help of this modeling one can see the fast π rise in analogy to the phase of a driven harmonic oscillator that changes from in-phase when the driving frequency is below the resonance of the oscillator and out-of-phase above. The 2π jump, however, emerges from the complex dynamics of the several levels involved and can not be easily broken down to a two-level picture. Altogether, these findings confirm that the Rydberg interferometer can track the dynamics of the selected Rydberg state and enabled the tomography of the Rydberg state. Moreover, these measurements show the potential of the Rydberg interferometer as tool to explore the dynamic of quantum systems.

Among the most interesting candidates for further investigations are two-atom or many-atom Rydberg systems which have sparked considerable interest recently due to their strong interaction[120]. But even as important as the strength of the interaction is its tunability via Förster resonances[121], since this may allow to switch the interaction by an external control parameter, the electric field. The electric field value for these resonances as well as their strength are determined from calculations similar to those presented in this thesis, i.e. based on matrix elements calculated from model potentials. To employ Förster resonances as tool to control the interaction between Rydberg atoms, the validity of the calculations should be tested first.

When it comes to the search for a setup to explore structure and strength of a Förster resonance, the Rydberg interferometer lends itself as an ideal candidate. The results of this thesis show that the interferometer is capable to exploit the level structure of single Rydberg atoms. As the interaction between

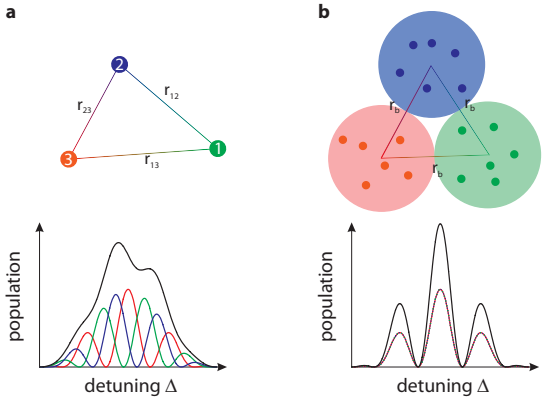

Figure C.2 | Visibility of Ramsey fringes at Förster resonance.
In a strongly interacting sample of atoms, the energy shift of an atom depends on the distances to its neighbors. **a** Due to the distribution of distances, all atomic levels are shifted differently and thus different phase shifts in the fringe pattern occur. This causes to wash out the Ramsey signal averaged over all atoms. **b** If the interaction is strong enough that collective phenomena occur, blockade effects emerge and the energy shift saturates for low distances. Thus also the phase shift does not depend on the distance and a clear fringe pattern is visible again.

two Rydberg atoms can be obtained from the single atom energy levels, the Rydberg interferometer is a readily available tool to measure interaction.

However, the experimental conditions have to be chosen carefully. As it has become clear in the course of this thesis, applying electric and magnetic fields simultaneously leads to a lifting of all degeneracies of the Rydberg atoms and, if the fields are not parallel, they even lead to coupling of the single-atom levels already. Consequently, one of the two fields must be circumvented. Since the Förster resonances are tunable via electric fields, it is a natural choice to avoid the application of magnetic fields. This is even more preferable since experiments by Afrousheh et al.[122] have revealed that already weak magnetic fields on the order of 500 mG can dramatically reduce the strength of Förster resonances. The reason for this reduction again is the lifting of the degeneracies of the magnetic substates. However, the presented setup is based on the magnetic trapping of the ground-state atoms and the atoms are released when the magnetic field is turned off. Thus it is necessary to trap the ground-state atoms in an optical dipole trap[123] during the experiment.

The densities reachable in optical dipole traps are as high as in magnetic traps and the preparations of such dense samples from the existing setup is feasible. The experimental approach to investigate the Förster resonances is very similar to the one presented in chapter 10 for the single atom case. A sample of ultracold rubidium atoms is prepared and with the first Ramsey pulse in zero electric field, a superposition between ground state and Rydberg state, e.g. $46d_{5/2}$, is created. Since the interaction is only weak when the Ramsey pulse occurs, blockade effect may be neglected. Then, the electric field is ramped up and the energies of the two-atom pair states, $46d_{5/2}46d_{5/2} - 44f48p_{3/2}$ are tuned towards resonance and hence the interaction strength is increased.

If the interaction is strong enough to shift the energy levels of the Rydberg atoms, they will accumulate a relative phase shift while the electric field is on. This phase shift can be observed as shift in the fringe pattern after the second Ramsey pulse. Since the interaction is of resonant dipole-dipole type, its strength scales as $1/r^3$, where r is the distance of the interacting Rydberg atoms. Accordingly, the phase shift of each Rydberg atom depends on the distribution of Rydberg atoms nearby and the averaged Ramsey pattern will be washed out, as depicted in Figure C.2 **a**.

However, if the interaction strength is increased further, a different regime of interaction is reached. Because the interaction between two Rydberg atoms shifts the its energy levels, it can become strong enough to shift the states out of resonance again: the Rydberg blockade occurs[53,115,124]. This blockade leads to a deviation from the $1/r^3$ behavior of the interaction potential for small distances and the interaction energy is constant for distances smaller than the blockade radius r_b[125]. When the interaction is strong enough to reach this regime, the phase shift will be equal for all atoms again, since the energy shift is insensitive to the atomic spacings. The averaged Ramsey fringe pattern then will retain its full visibility again.

When the electric field is scanned in high density samples, a characteristic behavior will herald the a Förster resonance. While the visibility of the fringe pattern is high at electric fields far from the resonance, it will vanish as the field strength approaches the resonance. On resonance, however, the visibility revives and a clear fringe pattern is visible. When the electric field is increased further, the coupling strength decreases again and the visibility first vanishes in the region of mediate coupling strength before the fringe pattern reappears for sufficiently large electric fields where the interaction is weak again. For this investigation, the Rydberg interferometer turns out to be an ideal tool.

A Appendix

A.1 Measurement of the lifetime of Rydberg molecules

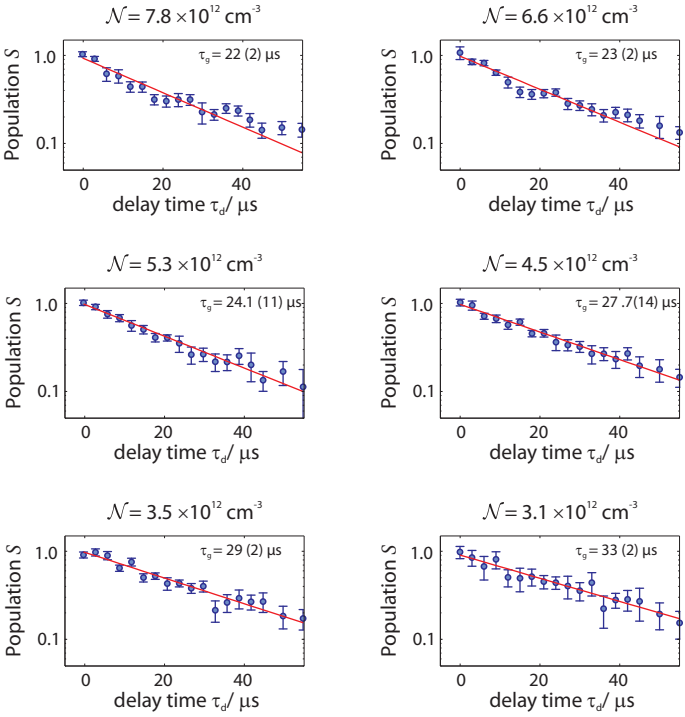

Figure A.1 | Lifetime τ_g of the ground state of $35s$-Rydberg molecules. Rydberg population after variable delay time τ_d between excitation and field ionization for the ground state of ultralong-range Rydberg molecules for different densities of ground-state atoms, $\mathcal{N}$. The Rydberg populations with delayed field ionization are normalized to the population that is measured in the same sample without delay time. Error bars indicate one standard deviation.

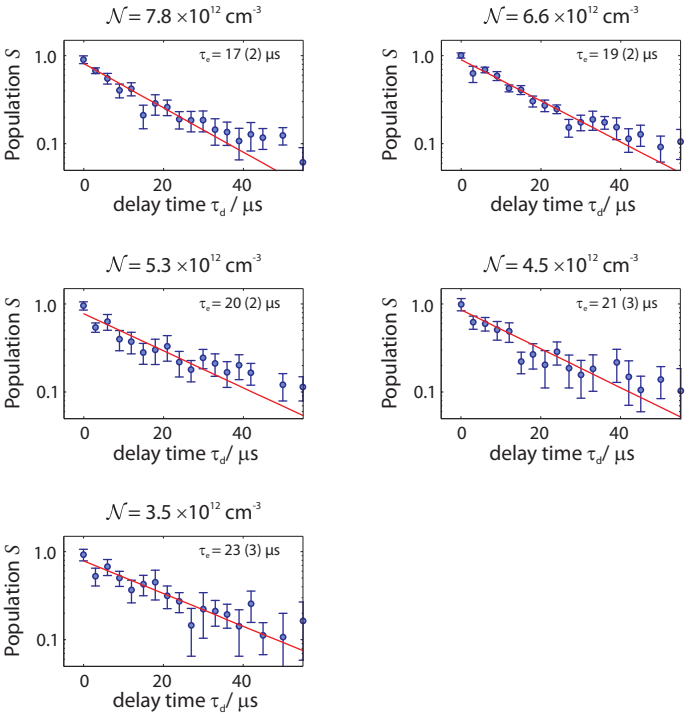

Figure A.2 | Lifetime τ_e of the excited state of Rydberg molecules.
Rydberg population after variable delay time τ_d between excitation and field ionization for an excited state of ultralong-range Rydberg molecules for different densities of ground-state atoms, $\mathcal{N}$. The Rydberg populations with delayed field ionization are normalized to the population that is measured in the same sample without delay time. Error bars indicate one standard deviation.

A.2 Eigenstate in the electric field

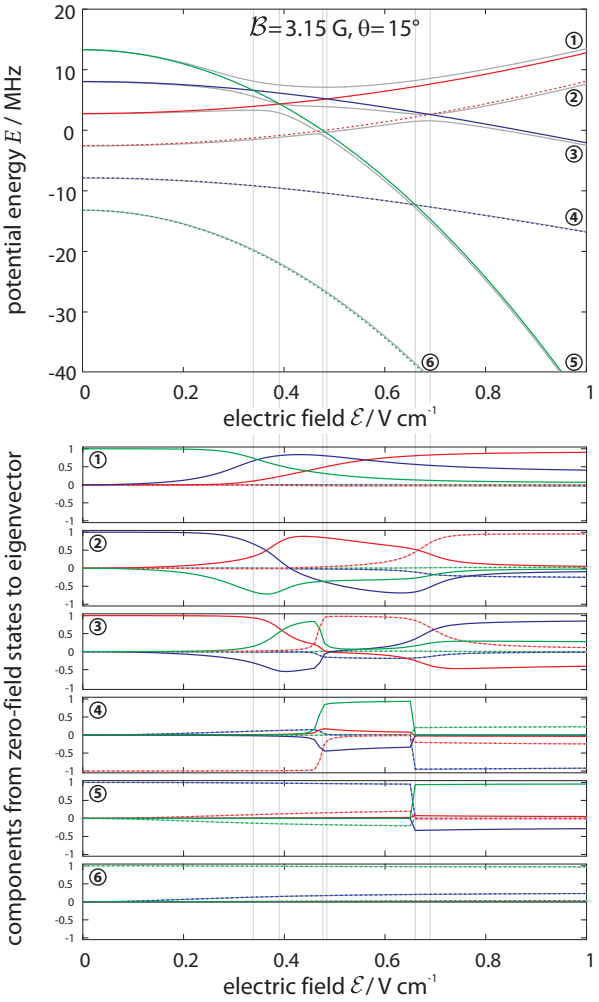

Figure A.3 | Eigenstates of the adiabatic energies in crossed $\mathcal{E}$ and $\mathcal{B}$ fields. The eigenvectors of the adiabatic energy curves (gray curves) can be expressed in the basis of the uncoupled states $m_j = -5/2 \ldots m_j = 5/2$ (colored). The contributions to each adiabatic state from the uncoupled basis are depicted in the subfigures and the line styles correspond to the uncoupled basis states.

Bibliography

[1] M. Müller, I. Lesanovsky, H. Weimer, H. P. Büchler, and P. Zoller. Mesoscopic Rydberg Gate Based on Electromagnetically Induced Transparency. *Physical Review Letters*, 102(17):170502, May 2009. doi: 10.1103/PhysRevLett.102.170502. arXiv: 0811.1155.

[2] H. Weimer, M. Müller, I. Lesanovsky, P. Zoller, and H. P. Büchler. A Rydberg quantum simulator. *Nature Physics*, 6:382–388, May 2010. doi: 10.1038/nphys1614.

[3] C. H. Greene, A. S. Dickinson, and H. R. Sadeghpour. Creation of Polar and Nonpolar Ultra-Long-Range Rydberg Molecules. *Physical Review Letters*, 85:2458–2461, September 2000. doi: 10.1103/PhysRevLett.85.2458.

[4] V. Bendkowsky, B. Butscher, J. Nipper, J. P. Shaffer, R. Löw, and T. Pfau. Observation of ultralong-range Rydberg molecules. *Nature*, 458:1005–1008, April 2009. doi: 10.1038/nature07945.

[5] S. Ospelkaus, K.-K. Ni, D. Wang, M. H. G. de Miranda, B. Neyenhuis, G. Quéméner, P. S. Julienne, J. L. Bohn, D. S. Jin, and J. Ye. Quantum-State Controlled Chemical Reactions of Ultracold Potassium-Rubidium Molecules. *Science*, 327:853–, February 2010. doi: 10.1126/science.1184121. arXiv: 0912.3854.

[6] V. Bendkowsky, B. Butscher, J. Nipper, J. B. Balewski, J. P. Shaffer, R. Löw, T. Pfau, W. Li, J. Stanojevic, T. Pohl, and J. M. Rost. Rydberg Trimers and Excited Dimers Bound by Internal Quantum Reflection. *Physical Review Letters*, 105(16):163201, October 2010. doi: 10.1103/PhysRevLett.105.163201. arXiv: 0912.4058.

[7] B. Butscher, V. Bendkowsky, J. Nipper, J. B. Balewski, L. Kukota, R. Löw, T. Pfau, W. Li, T. Pohl, and J. M. Rost. Lifetimes of ultralong-range Rydberg molecules in vibrational ground and excited state. *accepted for publication in J. Phys. B*, February 2011. arXiv: 1102.4069.

[8] A.-M. Lagrange, M. Bonnefoy, G. Chauvin, D. Apai, D. Ehrenreich, A. Boccaletti, D. Gratadour, D. Rouan, D. Mouillet, S. Lacour, and M. Kasper. A Giant Planet Imaged in the Disk of the Young Star β Pictoris. *Science*, 329:57–, July 2010. doi: 10.1126/science.1187187. arXiv: 1006.3314.

[9] J. Fraunhofer. Bestimmung des Brechungs- und des Farbenzerstreungs-Vermögens verschiedener Glasarten, in Bezug auf die Vervollkommnung achromatischer Fernröhre. *Annalen der Physik*, 56:264–313, 1817. doi: 10.1002/andp.18170560706.

[10] N. Bohr. On the Constitution of Atoms and Molecules. *Phil. Mag.*, 26:1, 476, 857, 1913.

[11] N. Kolachevsky, A. Matveev, J. Alnis, C. G. Parthey, S. G. Karshenboim, and T. W. Hänsch. Measurement of the 2S Hyperfine Interval in Atomic Hydrogen. *Physical Review Letters*, 102(21):213002, May 2009. doi: 10.1103/PhysRevLett.102.213002. arXiv: 0812.3509.

[12] I. I. Rabi, J. R. Zacharias, S. Millman, and P. Kusch. A New Method of Measuring Nuclear Magnetic Moment. *Physical Review*, 53:318–318, February 1938. doi: 10.1103/PhysRev.53.318.

[13] N. F. Ramsey. A New Molecular Beam Resonance Method. *Physical Review*, 76:996–996, October 1949. doi: 10.1103/PhysRev.76.996.

[14] P. Rochat, F. Droz, P. Mosset, G. Barmaverain, Q. Wang, D. Boving, L. Mattioni, M. Belloni, M. Gioia, U. Schmidt, T. Pike, and F. Emma. The onboard galileo rubidium and passive maser, status amp; performance. In *Frequency Control Symposium and Exposition, 2005. Proceedings of the 2005 IEEE International*, pages 26 –32, August 2005.

[15] A. L. Schawlow and C. H. Townes. Infrared and Optical Masers. *Physical Review*, 112:1940–1949, December 1958. doi: 10.1103/PhysRev.112.1940.

[16] C. W. Chou, D. B. Hume, J. C. J. Koelemeij, D. J. Wineland, and T. Rosenband. Frequency Comparison of Two High-Accuracy Al^+ Optical Clocks. *Physical Review Letters*, 104(7):070802, February 2010. doi: 10.1103/PhysRevLett.104.070802. arXiv: 0911.4527.

[17] S. Haroche, M. Gross, and M. P. Silverman. Observation of Fine-Structure Quantum Beats Following Stepwise Excitation in Sodium D States. *Physical Review Letters*, 33:1063–1066, October 1974. doi: 10.1103/PhysRevLett.33.1063.

[18] M. Marinescu, H. R. Sadeghpour, and A. Dalgarno. Dispersion coefficients for alkali-metal dimers. *Physical Review A*, 49:982–988, February 1994. doi: 10.1103/PhysRevA.49.982.

[19] H. M. J. M. Boesten, C. C. Tsai, J. R. Gardner, D. J. Heinzen, and B. J. Verhaar. Observation of a shape resonance in the collision of two cold ^{87}Rb atoms. *Physical Review A*, 55:636–640, January 1997. doi: 10.1103/PhysRevA.55.636.

[20] J. Mitroy and M. W. Bromley. Semiempirical calculation of van der Waals coefficients for alkali-metal and alkaline-earth-metal atoms. *Physical Review A*, 68(5):052714, November 2003. doi: 10.1103/PhysRevA.68.052714.

[21] K. Singer. http://quantendynamik.physik.uni-freiburg.de/potcalc/.

[22] D. Jaksch, J. I. Cirac, P. Zoller, S. L. Rolston, R. Côté, and M. D. Lukin. Fast Quantum Gates for Neutral Atoms. *Physical Review Letters*, 85:2208–2211, September 2000. doi: 10.1103/PhysRevLett.85.2208. arXiv: quant-ph/0004038.

[23] M. D. Lukin, M. Fleischhauer, R. Cote, L. M. Duan, D. Jaksch, J. I. Cirac, and P. Zoller. Dipole Blockade and Quantum Information Processing in Mesoscopic Atomic Ensembles. *Physical Review Letters*, 87(3):037901, July 2001. doi: 10.1103/PhysRevLett.87.037901. arXiv: quant-ph/0011028.

[24] E. A. Cornell and C. E. Wieman. Nobel Lecture: Bose-Einstein condensation in a dilute gas, the first 70 years and some recent experiments. *Reviews of Modern Physics*, 74:875–893, August 2002. doi: 10.1103/RevModPhys.74.875.

[25] W. Ketterle. Nobel lecture: When atoms behave as waves: Bose-Einstein condensation and the atom laser. *Reviews of Modern Physics*, 74:1131–1151, November 2002. doi: 10.1103/RevModPhys.74.1131.

[26] Rolf Heidemann. *Rydberg Excitation of Bose-Einstein Condensates: Coherent Collective Dynamics*. PhD thesis, Universität Stuttgart, March 2008.

[27] Ulrich Raitzsch. *Universal scaling and coherence properties of an ultracold Rydberg gas*. PhD thesis, Universität Stuttgart, November 2008.

[28] Vera Bendkowsky. *Ultralong-range Rydberg molecules: Investigation of a novel binding*. PhD thesis, Universität Stuttgart, March 2010.

[29] Anders J. Ångström. *Recherches sur le Spectre Solaire*. W. Schultz, Upsala, 1868.

[30] William Huggins. On the photographic spectra of stars. [abstract]. *Proceedings of the Royal Society of London*, 30:pp. 20–22, 1879.

[31] J. J. Balmer. Notiz über die Spektrallinien des Wasserstoffs. *Ann. Phys. Chem.*, 25:80, 1885.

[32] J. R. Rydberg. On the Structure of the Line Spectra of the Chemical Elements. *Phil Mag 5th series*, 29:331–337, 1890.

[33] W. Li, I. Mourachko, M. W. Noel, and T. F. Gallagher. Millimeter-wave spectroscopy of cold Rb Rydberg atoms in a magneto-optical trap: Quantum defects of the ns, np, and nd series. *Physical Review A*, 67(5):052502, May 2003. doi: 10.1103/PhysRevA.67.052502.

[34] C-J. Lorenzen and K. Niemax. Quantum Defects of the n2P1/2,3/2 Levels in 39K I and 85Rb I. *Phys. Scr.*, 27:300–305, 1983. doi: 10.1088/0031-8949/27/4/012.

[35] M. J. Seaton. REVIEW ARTICLE: Quantum defect theory. *Reports of Progress in Physics*, 46:167–257, February 1983.

[36] T. F. Gallagher. *Rydberg Atoms*. Cambrige University Press, October 1994.

[37] Aaron W. Reinhard. *Cold Rydberg-Atom Interactions*. PhD thesis, University of Michigan, 2008.

[38] F. Gounand. Radiative lifetimes of highly excited states in rubidium. *Journal de Physique*, 40:457–460, May 1979.

[39] I. I. Beterov, I. I. Ryabtsev, D. B. Tretyakov, and V. M. Entin. Quasiclassical calculations of blackbody-radiation-induced depopulation rates and effective lifetimes of Rydberg nS , nP , and nD alkali-metal atoms with $n \leq 80$. *Physical Review A*, 79(5):052504, May 2009. doi: 10.1103/PhysRevA.79.052504. arXiv: 0810.0339.

[40] A. L. Oliveira, M. W. Mancini, V. S. Bagnato, and L. G. Marcassa. Measurement of Rydberg-state lifetimes using cold trapped atoms. *Physical Review A*, 65(3):031401, March 2002. doi: 10.1103/PhysRevA.65.031401.

[41] D. B. Branden, T. Juhasz, T. Mahlokozera, C. Vesa, R. O. Wilson, M. Zheng, A. Kortyna, and D. A. Tate. Radiative lifetime measurements of rubidium Rydberg states. *Journal of Physics B Atomic Molecular Physics*, 43(1):015002, January 2010. doi: 10.1088/0953-4075/43/1/015002. arXiv: 0910.1073.

[42] Gounand, F., Hugon, M., and Fournier, P.R. Radiative lifetimes of highly excited states in rubidium. *J. Phys. France*, 41(2):119–121, 1980. doi: 10.1051/jphys:01980004102011900.

[43] F. Gounand, P. R. Fournier, J. Cuvellier, and J. Berlande. Determination of natural radiative lifetimes for highly excited P states in rubidium. *Physics Letters A*, 59:23–24, November 1976. doi: 10.1016/0375-9601(76)90340-6.

[44] M. Hugon, F. Gounand, and P. R. Fournier. Radiative lifetimes of highly excited F states in rubidium. *Journal of Physics B Atomic Molecular Physics*, 11:L605–L609, October 1978. doi: 10.1088/0022-3700/11/20/002.

[45] V. A. Nascimento, L. L. Caliri, A. L. de Oliveira, V. S. Bagnato, and L. G. Marcassa. Measurement of the lifetimes of S and D states below n=31 using cold Rydberg gas. *Physical Review A*, 74(5):054501, November 2006. doi: 10.1103/PhysRevA.74.054501.

[46] L. L. Caliri and L. G. Marcassa. Reply to "Comment on 'Measurement of the lifetimes of S and D states below n=31 using cold Rydberg gas'". *Physical Review A*, 75(6):066503, June 2007. doi: 10.1103/PhysRevA.75.066503.

[47] T. F. Gallagher and W. E. Cooke. Interactions of Blackbody Radiation with Atoms. *Physical Review Letters*, 42:835–839, March 1979. doi: 10.1103/PhysRevLett.42.835.

[48] J. D. Jackson. *Classical Electrodynamics*. John Wiley & Sons, New York, 1975.

[49] K. Singer, J. Stanojevic, M. Weidemüller, and R. Côté. Long-range interactions between alkali Rydberg atom pairs correlated to the ns ns, np np and nd nd asymptotes. *Journal of Physics B Atomic Molecular Physics*, 38:295, January 2005. doi: 10.1088/0953-4075/38/2/021.

[50] T. Förster. Transfer mechanisms of electronic excitation. *Discuss. Faraday Soc.*, (27):7–27, 1959. doi: 10.1039/DF9592700007.

[51] A. Reinhard, T. C. Liebisch, B. Knuffman, and G. Raithel. Level shifts of rubidium Rydberg states due to binary interactions. *Physical Review A*, 75(3):032712, March 2007. doi: 10.1103/PhysRevA.75.032712.

[52] H. Feshbach. Unified theory of nuclear reactions. *Annals of Physics*, 5:357–390, December 1958. doi: 10.1016/0003-4916(58)90007-1.

[53] R. Heidemann, U. Raitzsch, V. Bendkowsky, B. Butscher, R. Löw, L. Santos, and T. Pfau. Evidence for Coherent Collective Rydberg Excitation in the Strong Blockade Regime. *Physical Review Letters*, 99(16):163601, October 2007. doi: 10.1103/PhysRevLett.99.163601. arXiv: arXiv:quant-ph/0701120.

[54] E. Urban, T. A. Johnson, T. Henage, L. Isenhower, D. D. Yavuz, T. G. Walker, and M. Saffman. Observation of Rydberg blockade between two atoms. *Nature Physics*, 5:110–114, February 2009. doi: 10.1038/nphys1178. arXiv: 0805.0758.

[55] A. Gaëtan, Y. Miroshnychenko, T. Wilk, A. Chotia, M. Viteau, D. Comparat, P. Pillet, A. Browaeys, and P. Grangier. Observation of collective excitation of two individual atoms in the Rydberg blockade regime. *Nature Physics*, 5:115–118, February 2009. doi: 10.1038/nphys1183. arXiv: 0810.2960.

[56] R. Heidemann, U. Raitzsch, V. Bendkowsky, B. Butscher, R. Löw, and T. Pfau. Rydberg Excitation of Bose-Einstein Condensates. *Physical Review Letters*, 100(3):033601, January 2008. doi: 10.1103/PhysRevLett.100.033601. arXiv: 0710.5622.

[57] Enrico Fermi. Sopra lo spostamento per pressione delle righe elevate delle serie spettrali. *Nuovo Cimento*, 11:157–166, 1934. doi: 10.1007/BF02959829.

[58] J. M. Blatt and J. D. Jackson. On the Interpretation of Neutron-Proton Scattering Data by the Schwinger Variational Method. *Physical Review*, 76:18–37, July 1949. doi: 10.1103/PhysRev.76.18.

[59] T. F. O'Malley, L. Spruch, and L. Rosenberg. Modification of Effective-Range Theory in the Presence of a Long-Range (r^{-4}) Potential. *Journal of Mathematical Physics*, 2:491–498, July 1961. doi: 10.1063/1.1703735.

[60] I. I. Fabrikant. Interaction of Rydberg atoms and thermal electrons with K, Rb and Cs atoms. *Journal of Physics B Atomic Molecular Physics*, 19:1527–1540, May 1986. doi: 10.1088/0022-3700/19/10/021.

[61] C. Bahrim and U. Thumm. Low-lying $^3P^o$ and $^3S^e$ states of Rb^-, Cs^-, and Fr^-. *Physical Review A*, 61(2):022722, February 2000. doi: 10.1103/PhysRevA.61.022722.

[62] E. L. Hamilton, C. H. Greene, and H. R. Sadeghpour. LETTER TO THE EDITOR: Shape-resonance-induced long-range molecular Rydberg states. *Journal of Physics B Atomic Molecular Physics*, 35:L199–L206, May 2002. doi: 10.1088/0953-4075/35/10/102.

[63] M. L. Zimmerman, M. G. Littman, M. M. Kash, and D. Kleppner. Stark structure of the Rydberg states of alkali-metal atoms. *Physical Review A*, 20:2251–2275, December 1979. doi: 10.1103/PhysRevA.20.2251.

[64] V. A. Kostelecký and M. M. Nieto. Analytical wave functions for atomic quantum-defect theory. *Physical Review A*, 32:3243–3246, December 1985. doi: 10.1103/PhysRevA.32.3243.

[65] C. E. Theodosiou. Lifetimes of alkali-metal-atom Rydberg states. *Physical Review A*, 30:2881–2909, December 1984. doi: 10.1103/PhysRevA.30.2881.

[66] S. A. Bhatti, C. L. Cromer, and W. E. Cooke. Analysis of the Rydberg character of the $5d7d\,^1D_2$ state of barium. *Physical Review A*, 24:161–165, July 1981. doi: 10.1103/PhysRevA.24.161.

[67] Mark Galassi, Jim Davies, James Theiler, Brian Gough, Gerard Jungman, Michael Booth, and Fabrice Rossi. *Gnu Scientific Library: Reference Manual*. Network Theory Ltd., January 2009.

[68] I. I. Sobelman. *Atomic Spectra and Radiative Transitions*. Springer Series on Atoms+Plasmas. Springer Verlag, Berlin, 2. edition, 1996.

[69] W. Li, P. J. Tanner, Y. Jamil, and T. F. Gallagher. Ionization and plasma formation in high n cold Rydberg samples. *European Physical Journal D*, 40:27–35, October 2006. doi: 10.1140/epjd/e2006-00189-8.

[70] W. Li, P. J. Tanner, and T. F. Gallagher. Dipole-Dipole Excitation and Ionization in an Ultracold Gas of Rydberg Atoms. *Physical Review Letters*, 94(17):173001, May 2005. doi: 10.1103/PhysRevLett.94.173001.

[71] J. A. Gaunt. The triplets of helium. *Philosophical Transactions of the Royal Society of London. Series A, Containing Papers of a Mathematical or Physical Character*, 228:pp. 151–196, 1929.

[72] C. Eckart. The Application of Group theory to the Quantum Dynamics of Monatomic Systems. *Reviews of Modern Physics*, 2:305–380, July 1930. doi: 10.1103/RevModPhys.2.305.

[73] E. Wigner. Einige Folgerungen aus der Schrödingerschen Theorie für die Termstrukturen. *Zeitschrift fur Physik*, 43:624–652, September 1927. doi: 10.1007/BF01397327.

[74] Pierre Meystre. *Atom Optics*. Springer Verlag, New York, 2001.

[75] Pierre Meystre and Murray Sargent, III. *Elements of Quantum Optics*. Springer Verlag, Heidelberg, 4 edition, 2007.

[76] F. Bloch. Nuclear Induction. *Physical Review*, 70:460–474, October 1946. doi: 10.1103/PhysRev.70.460.

[77] R. P. Feynman, F. L. Vernon, Jr., and R. W. Hellwarth. Geometrical Representation of the Schrödinger Equation for Solving Maser Problems. *Journal of Applied Physics*, 28:49–52, January 1957. doi: 10.1063/1.1722572.

[78] L. Allen and J. H. Eberly. *Optical resonance and two-level atoms*. Dover publications, 1987.

[79] F. Bloch. Nuclear induction. *Phys. Rev.*, 70(7-8):460–474, Oct 1946. doi: 10.1103/PhysRev.70.460.

[80] H. J. Metcalf and P. van der Straten. *Laser Cooling and Trapping*. Springer Verlag, New York, 1999.

[81] H. C. Torrey. Transient Nutations in Nuclear Magnetic Resonance. *Physical Review*, 76:1059–1068, October 1949. doi: 10.1103/PhysRev.76.1059.

[82] Ulrich Raitzsch: *Aufbau einer UHV-Kammer zur DurchfÃ¼hrung von Experimenten mit Bose-Einstein-Kondensaten in optischen Gittern*. Diplomarbeit, Universität Stuttgart, December 2004.

[83] Robert Löw. *A versatile setup for experiments with Rubidium Bose Einstein condensates: From optical lattices to Rydberg matter*. PhD thesis, Universität Stuttgart, December 2006.

[84] E. W. Streed, A. P. Chikkatur, T. L. Gustavson, M. Boyd, Y. Torii, D. Schneble, G. K. Campbell, D. E. Pritchard, and W. Ketterle. Large

atom number Bose-Einstein condensate machines. *Review of Scientific Instruments*, 77(2):023106, February 2006. doi: 10.1063/1.2163977. arXiv: arXiv:cond-mat/0507348.

[85] W. D. Phillips, H. Metcalf, and H. Metcalf. Laser Deceleration of an Atomic Beam. *Physical Review Letters*, 48:596–599, March 1982. doi: 10.1103/PhysRevLett.48.596.

[86] Ettore Majorana. Atomi orientati in campo magnetico variabile. *Il Nuovo Cimento (1924-1942)*, 9:43–50, 1932.

[87] H. Bender: *Mikrowellen-Anregung von ultrakalten Atomen*. Diplomarbeit, Universität Stuttgart, December 2006.

[88] Björn Butscher: *Kollektive kohärente Anregung von ultrakalten Rydberg-Atomen*. Diplomarbeit, Universität Stuttgart, December 2007.

[89] W. Demtröder. *Laserspektroskopie : Grundlagen und Techniken*. Springer Verlag, Berlin, 4 edition, 2000.

[90] Stephan A. Schulz. *Scalable Microchip Ion Traps for Quantum Computation*. PhD thesis, Universität Ulm, 2009.

[91] R. W. P. Drever, J. L. Hall, F. V. Kowalski, J. Hough, G. M. Ford, A. J. Munley, and H. Ward. Laser phase and frequency stabilization using an optical resonator. *Applied Physics B: Lasers and Optics*, 31:97–105, June 1983. doi: 10.1007/BF00702605.

[92] Jonathan Balewski: *Hochauflösende Photoassoziationsspektroskopie von Rydberg-Dimeren und Trimeren*. Diplomarbeit, Universität Stuttgart, December 2009.

[93] A. Grabowski. *Aufbau einer Messaparatur zur Laserkühlung und hochauflösende Rydberg-Spektroskopie an ^{87}Rb-Atomen*. PhD thesis, Universität Stuttgart, 16 March 2006.

[94] A. D. Cronin, J. Schmiedmayer, and D. E. Pritchard. Optics and interferometry with atoms and molecules. *Reviews of Modern Physics*, 81:1051–1129, July 2009. doi: 10.1103/RevModPhys.81.1051. arXiv: 0712.3703.

[95] W. Hanle. Über magnetische Beeinflussung der Polarisation der Resonanzfluoreszenz. *Zeitschrift fur Physik*, 30:93–105, December 1924. doi: 10.1007/BF01331827.

[96] W. Gerlach and O. Stern. Der experimentelle Nachweis der Richtungsquantelung im Magnetfeld. *Zeitschrift fur Physik*, 9:349–352, December 1922. doi: 10.1007/BF01326983.

[97] G. K. Radda. The Use of NMR Spectroscopy for the Understanding of Disease. *Science*, 233:640–645, August 1986. doi: 10.1126/science.3726553.

[98] L. Essen and J. V. L. Parry. An Atomic Standard of Frequency and Time Interval: A Cæsium Resonator. *Nature*, 176:280–282, August 1955. doi: 10.1038/176280a0.

[99] C. H. Bennett and D. P. DiVincenzo. Quantum information and computation. *Nature*, 404:247–255, March 2000. doi: 10.1038/35005001.

[100] N. F. Ramsey. A Molecular Beam Resonance Method with Separated Oscillating Fields. *Physical Review*, 78:695–699, June 1950. doi: 10.1103/PhysRev.78.695.

[101] C. N. Cohen-Tannoudji. Nobel Lecture: Manipulating atoms with photons. *Reviews of Modern Physics*, 70:707–719, July 1998. doi: 10.1103/RevModPhys.70.707.

[102] C. H. Greene. Quantum chemistry: The little molecule that could. *Nature*, 458:975–976, April 2009. doi: 10.1038/458975a.

[103] S. D. Hogan and F. Merkt. A new perspective on the binding power of an electron. *ChemPhysChem*, 10(17):2931–2934, 2009.

[104] I. Solomon. Rotary Spin Echoes. *Physical Review Letters*, 2:301–302, April 1959. doi: 10.1103/PhysRevLett.2.301.

[105] N. C. Wong, S. S. Kano, and R. G. Brewer. Optical rotary echoes. *Physical Review A*, 21:260–267, January 1980. doi: 10.1103/PhysRevA.21.260.

[106] Ulrich Raitzsch, Vera Bendkowsky, Rolf Heidemann, Björn Butscher, Robert Löw, and Tilman Pfau. Echo experiments in a strongly interacting rydberg gas. *Phys. Rev. Lett.*, 100(1):013002, Jan 2008. doi: 10.1103/PhysRevLett.100.013002.

[107] J. Clerk Maxwell. On the dynamical theory of gases. *Philosophical Transactions of the Royal Society of London*, 157:49–88, 1867.

[108] A. Sommerfeld. *Vorlesungen über theoretische Physik: Thermodynamik & Statistik*. Akademische Verlagsgesellschaft Geest & Portig, Leipzig, 3. edition, 1962.

[109] Heinz Niedrig. *Physik*. Springer Verlag, Berlin, 1. edition, 1992.

[110] C. Zener. Non-Adiabatic Crossing of Energy Levels. *Royal Society of London Proceedings Series A*, 137:696–702, September 1932.

[111] M. S. O'Sullivan and B. P. Stoicheff. Scalar polarizabilities and avoided crossings of high Rydberg states in Rb. *Physical Review A*, 31:2718–2720, April 1985. doi: 10.1103/PhysRevA.31.2718.

[112] Daniel A. Steck. Rubidium 87 d line data. available online at http://steck.us/alkalidata (revision 2.1.4), 12 2010. 23 December 2010.

[113] K. C. Harvey and B. P. Stoicheff. Fine Structure of the n^2D Series in Rubidium near the Ionization Limit. *Physical Review Letters*, 38:537–540, March 1977. doi: 10.1103/PhysRevLett.38.537.

[114] E. Schrödinger. Quantisierung als Eigenwertproblem. *Annalen der Physik*, 384:361–376, 1926. doi: 10.1002/andp.19263840404.

[115] D. Tong, S. M. Farooqi, J. Stanojevic, S. Krishnan, Y. P. Zhang, R. Côté, E. E. Eyler, and P. L. Gould. Local Blockade of Rydberg Excitation in an Ultracold Gas. *Physical Review Letters*, 93(6):063001, August 2004. doi: 10.1103/PhysRevLett.93.063001. arXiv: physics/0402113.

[116] K. Singer, M. Reetz-Lamour, T. Amthor, L. G. Marcassa, and M. Weidemüller. Suppression of Excitation and Spectral Broadening Induced by Interactions in a Cold Gas of Rydberg Atoms. *Physical Review Letters*, 93(16):163001, October 2004. doi: 10.1103/PhysRevLett.93.163001. arXiv: physics/0404075.

[117] T. Vogt, M. Viteau, J. Zhao, A. Chotia, D. Comparat, and P. Pillet. Dipole Blockade at Förster Resonances in High Resolution Laser Excitation of Rydberg States of Cesium Atoms. *Physical Review Letters*, 97(8):083003, August 2006. doi: 10.1103/PhysRevLett.97.083003.

[118] T. Young. The Bakerian Lecture: Experiments and Calculations Relative to Physical Optics. *Royal Society of London Philosophical Transactions Series I*, 94:1–16, 1804.

[119] Johannes Nipper. Linear stark effect in a polar homonuclear molecule. Unpublished data, 2011.

[120] Hendrik Weimer and Hans Peter Büchler. Two-stage melting in systems of strongly interacting rydberg atoms. *Phys. Rev. Lett.*, 105(23):230403, Nov 2010. doi: 10.1103/PhysRevLett.105.230403.

[121] M. Saffman, T. G. Walker, and K. Mølmer. Quantum information with Rydberg atoms. *Reviews of Modern Physics*, 82:2313–2363, July 2010. doi: 10.1103/RevModPhys.82.2313. arXiv: 0909.4777.

[122] K. Afrousheh, P. Bohlouli-Zanjani, J. D. Carter, A. Mugford, and J. D. D. Martin. Resonant electric dipole-dipole interactions between cold Rydberg atoms in a magnetic field. *Physical Review A*, 73(6):063403, June 2006. doi: 10.1103/PhysRevA.73.063403. arXiv: physics/0604169.

[123] R. Grimm, M. Weidemüller, and Y. B. Ovchinnikov. Optical dipole traps for neutral atoms. *ArXiv Physics e-prints*, February 1999. arXiv: arXiv:physics/9902072.

[124] T. Vogt, M. Viteau, A. Chotia, J. Zhao, D. Comparat, and P. Pillet. Electric-Field Induced Dipole Blockade with Rydberg Atoms. *Physical Review Letters*, 99(7):073002, August 2007. doi: 10.1103/PhysRevLett.99.073002. arXiv: arXiv:physics/0703102.

[125] J. E. Johnson and S. L. Rolston. Interactions between Rydberg-dressed atoms. *Physical Review A*, 82(3):033412, September 2010. doi: 10.1103/PhysRevA.82.033412. arXiv: 1006.3212.

Zum Schluß dieser Arbeit nutze ich die Gelegenheit um allen zu danken, die durch ihre vielfältige Unterstützung zum Gelingen meiner Doktorarbeit beigetragen haben.

Zunächst möchte ich Tilman Pfau dafür danken, daß er mich schon zu Beginn meines Studiums an sein Institut aufgenommen und mir die Chance gegeben hat, das Rydberg-Experiment frühzeitig und umfassend kennenzulernen und meine Dissertation an diesem Experiment durchzuführen. Insbesondere danke ich ihm für die vielen guten Ideen und Diskussionen.

Ein großer Dank geht an alle, die vor mir das Rydberg-Thema beackert haben und wertvolle Vorarbeiten geleistet haben. Dies sind zum einen Axel, der als Pionier die ersten Schritte auf diesem unbekannten Terrain gemacht hat und Robert, der durch seine Weitsicht schon bei der Planung und beim Aufbau der BEC-Kammer den Grundstein für die zukünfigen Erfolge gelegt hat.

Danke auch an Rolf für die Geduld, die er mit mir hatte und für die fortwährende Unterstützung und Anleitung zum selbständigen Arbeiten. Außerdem danke ich Ulrich, der mich mit den Besonderheiten der BEC-Kammer vertraut gemacht und sein Wissen gerne weitergegeben hat.

Vera danke ich für die Erkenntnis, daß man mit ‚einfacher' Spektroskopie gepaart mit physikalischem Gespür bahnbrechende Ergebnisse erzielen kann und für die umfangreiche Erfahrung, die sie gerne mit mir geteilt hat.

Ein ganz besonderer Dank geht an Johannes und Jonathan, die mich stets mit vollem Einsatz unterstützt haben und auf die ich immer zählen konnte. Johannes danke ich insbesondere für seine Offenheit und seine Denkanstöße und dafür, daß sein Überblick oft neue Einsichten gebracht hat. Es war mir auch eine besondere Freude mit Jonathan arbeiten zu dürfen, der immer für das Experiment da war, durch seine zuverlässige und präzise Arbeitsweise viele Probleme gar nicht erst aufkommen ließ und immer Verständnis für die beiden wichtigsten Dinge hatte.

Außerdem danke ich Bea, Karin, Nadine und Oli für das Übernehmen der vielfältigen Verwaltungsaufgaben, die oft über ihren Aufgabenbereich hinaus gingen, und für die Unterhaltungen, die sich nicht um Physik drehten. Obwohl die kleinen oder Alltagsarbeiten manchmal unwichtig scheinen, ist die entlastende Wirkung ein wichtiger Teil des Erfolgs.

Danke auch an alle Kollegen im dritten und vierten Stock für die außergewöhnlich angenehme Arbeitsatmosphäre und ihre Hilfsbereitschaft bei Problemen aller Art. Viele Projekte wären ohne die fachkundige Unterstützung der Werkstätten des Physikalischen Instituts undenkbar gewesen. Deshalb

gebührt auch allen Mitarbeitern dort mein Dank für die kleinen Meisterwerke, die sie geschaffen haben.

Prof. Gießen danke ich für die Übernahme des Mitberichts und für das kurzfristige Erstellen des Gutachtens und Prof. Büchler dafür, daß er den Vorsitz meiner Doktorprüfung übernommen hat. Bei der Carl-Zeiss-Stiftung bedanke ich mich für das Stipendium zur Förderung meiner Arbeit.

Ganz besonders bedanken möchte ich mich bei meinen Freunden und meiner Familie, die mich durch die letzten vier Jahre begleitet haben und mich immer unterstützt haben. Hendrik danke ich insbesondere für die vielen auflockernden und entspannenden Unterhaltungen über eine große Bandbreite von Themen. Von ganzem Herzen möchte ich Vera danken, die mich stets unterstützt und mich nach Rückschlägen wieder aufgerichtet hat, auch nach einem anstrengenden Tag ein offenes Ohr für meine Probleme und Verbesserungsvorschläge hatte und mich während der Auswerte- und Schreibphase ertragen hat. Deine Begeisterung für meine Arbeit hat sie zu etwas Besonderem werden lassen.

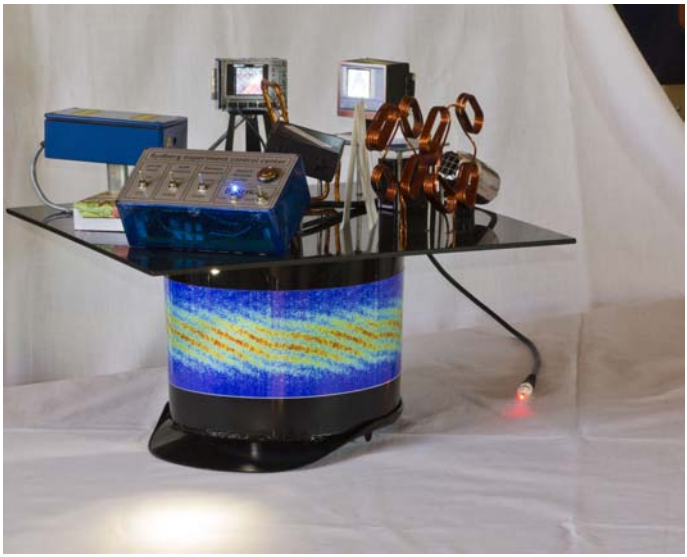

"In photo-association, two atoms cooled to submillikelvin temperatures are placed in an intense light field tuned to a frequency at which the pair can absorb one or several photons. The atom pair is then transferred to a state in which it forms a long-range molecule in a well-defined bound state, with one of the two atoms in an electronically excited state [...].

In this reaction, all internal and external degrees of freedom of the molecule are controlled. Therefore, in principle, the molecule can be converted back to free atoms. However, the lifetime of these molecules is usually very short, of the order of a few tens of nanoseconds, and in photo-association experiments so far the molecules decayed before the bond could be undone in controlled manner.[...]

The coherent excitation of Rydberg molecules can be understood by considering two states: a pair of free atoms and a molecule. Driving the system with a resonant laser prepares a superposition of these states; the system is neither a pair of atoms nor a molecule, but both at the same time. This superposition, however, is fragile and highly sensitive to the environment in which the atoms reside, which eventually leads to the collapse of the superposition.

To drive the system coherently using lasers, their phase must be kept constant during the entire process. Exploring the coherence at the ultimate limit set by the lifetime of the molecules requires a laser linewidth of less than 100 kHz. Equipped with such a laser source, Butscher et al. spectroscopically characterized the molecules and measured the coherence time of the atom-pair/Rydberg-molecule system and the lifetime of the Rydberg molecules. The study of Butscher et al. is an impressive example of coherent control over a reversible reaction."

Antoine Browaeys and Pierre Pillet,
nature physics 6, pp. 941 (2010)